INFORMATION TO USERS

This manuscript has been reproduced from the microfilm master. UMI films the text directly from the original or copy submitted. Thus, some thesis and dissertation copies are in typewriter face, while others may be from any type of computer printer.

The quality of this reproduction is dependent upon the quality of the copy submitted. Broken or indistinct print, colored or poor quality illustrations and photographs, print bleedthrough, substandard margins, and improper alignment can adversely affect reproduction.

In the unlikely event that the author did not send UMI a complete manuscript and there are missing pages, these will be noted. Also, if unauthorized copyright material had to be removed, a note will indicate the deletion.

Oversize materials (e.g., maps, drawings, charts) are reproduced by sectioning the original, beginning at the upper left-hand corner and continuing from left to right in equal sections with small overlaps. Each original is also photographed in one exposure and is included in reduced form at the back of the book.

Photographs included in the original manuscript have been reproduced xerographically in this copy. Higher quality 6" x 9" black and white photographic prints are available for any photographs or illustrations appearing in this copy for an additional charge. Contact UMI directly to order.

UMI

University Microfilms International
A Bell & Howell Information Company
300 North Zeeb Road, Ann Arbor, MI 48106-1346 USA
313/761-4700 800/521-0600

Reproduced with permission of the copyright owner. Further reproduction prohibited without permission.

Reproduced with permission of the copyright owner. Further reproduction prohibited without permission.

Order Number 9209701

Studies of inertio-gravity waves induced by geostrophic adjustment of the atmospheric jet stream

Luo, Zhangai, Ph.D.

University of Alaska Fairbanks, 1991

Copyright ©1992 by Luo, Zhangai. All rights reserved.

U·M·I
300 N. Zeeb Rd.
Ann Arbor, MI 48106

Reproduced with permission of the copyright owner. Further reproduction prohibited without permission.

Reproduced with permission of the copyright owner. Further reproduction prohibited without permission.

STUDIES OF INERTIO-GRAVITY WAVES INDUCED BY GEOSTROPHIC ADJUSTMENT OF THE ATMOSPHERIC JET STREAM

A

THESIS

Presented to the Faculty

of the University of Alaska Fairbanks

in Partial Fulfillment of the Requirements

for the Degree of

DOCTOR OF PHILOSOPHY

By

Zhangai Luo, B.S., M.S.

Fairbanks, Alaska

September 1991

Reproduced with permission of the copyright owner. Further reproduction prohibited without permission.

STUDIES OF INERTIO-GRAVITY WAVES INDUCED BY GEOSTROPHIC ADJUSTMENT OF THE ATMOSPHERIC JET STREAM

By

Zhangai Luo

RECOMMENDED:

Dr. David L. Musgrave

Dr. Thomas C. Royer

Dr. Hiroshi L. Tanaka

Dr. Walter R. Tape

Dr. David C. Fritts, Advisory Committee Chair

Dr. John L. Morack, Department Head

APPROVED:

Dr. Paul Reichardt, Dean, College of Natural Sciences

Dr. Luis Proenza, Dean of the Graduate School

8/1/91

Date

Reproduced with permission of the copyright owner. Further reproduction prohibited without permission.

Abstract

Motivated by observations revealing very low frequency gravity waves throughout the lower and middle atmosphere, this thesis investigates inertio–gravity waves (IGWs) radiating from an ageostrophic jet stream assuming geostrophic adjustment to be the source mechanism. Fourier integral and Green's function techniques are employed to solve this problem. The ageostrophic components of the motion field are described by an initially unbalanced Gaussian velocity field which has been chosen to have infinite and localized zonal extents corresponding to two–dimensional (2–D) and three–dimensional (3–D) cases. The adjustment process permits the radiation of IGWs and the attainment of an induced geostrophically balanced mean circulation.

The results of this thesis reveal IGW radiation from the initially unbalanced momentum source with frequencies near f (inertial frequency) and most of the disturbance energy associated with the IGW field. This research thus confirms geostrophic adjustment may be a major source of the low frequency gravity waves in the atmosphere. IGW structure includes primarily meridional wave propagation, with vertical and horizonal scales that depend on the initial unbalance configuration. The 3–D solutions at large distances from the jet core along the jet axis exhibit a change in IGW character from primarily meridional propagation at early times to largely zonal propagation at later times due to delayed arrival of IGW activity from more distant source regions. The induced mean flows in the 2–D and 3–D cases represent small fractions of the initial energy, insure conservation of potential vorticity, and reflect to a large degree the character of the momentum source.

Reproduced with permission of the copyright owner. Further reproduction prohibited without permission.

Contents

Reproduced with permission of the copyright owner. Further reproduction prohibited without permission.

Reproduced with permission of the copyright owner. Further reproduction prohibited without permission.

List of Figures

Reproduced with permission of the copyright owner. Further reproduction prohibited without permission.

Reproduced with permission of the copyright owner. Further reproduction prohibited without permission.

Reproduced with permission of the copyright owner. Further reproduction prohibited without permission.

Acknowledgements

I would like to express my great thanks to my advisor, Dr. Dave Fritts, for his constant support, encouragement and excellent academic guidance through my entire graduate studies. I have been motivated by his sharp physics insights and his numerous approaches to physical problems. I can feel his standing by me when I need help but I never feel pressure from him. I would say, without his guidance, this thesis would not be completed.

I would like to thank Dr. Hiroshi Tanaka for many discussions from which I learned a lot in the past few years. Thanks also for his numerous suggestions and criticisms on the early versions of this thesis which have made this dissertation more integrated.

Thanks also to my other committee members, Drs. David Musgrave, Tom Royer and Walter Tape, for their suggestions and reviews on different stages of this research, and for their endurance in the completion of my studies.

I also found many friends and colleagues who gave me much help. Among them, I would like to mention a few, Rich Honrath, Joe Isler and Wentong Lu, for their friendly support.

Finally, I would like to thank deeply my wife, Hongfei Lin, for her love always and the sacrifice of her academic education to accompany me in Alaska, supporting me in the completion of these studies.

Reproduced with permission of the copyright owner. Further reproduction prohibited without permission.

Chapter 1

Introduction

Gravity waves have received increasing attention during the last two or three decades owing to their significant dynamical roles in the atmosphere. These include transporting energy and momentum vertically and horizontally from one region to another (Fritts, 1984*a*), initiation or modulation of the development of severe weather (Ley and Peltier, 1978; Stobie *et al.*, 1983) and cascading energy from macroscale motions to turbulence by means of saturation and dissipation processes (Lindzen, 1981; Fritts, 1984*a*; Fritts and Dunkerton, 1985; Weinstock, 1987).

Hines (1960) first proposed that motions in the upper atmosphere ($\sim$ 80 km to lower F region) are hydrodynamic and result from activities of internal gravity waves propagating upward from below as well as sources and generation processes at greater heights (Gossard, 1962; Chimonas and Hines, 1970; Chimonas, 1970; Davis and Da Rosa, 1970; Hines *et al.*, 1974; Richmond, 1978; Yeh and Liu, 1985; and Dong and Yeh, 1988). Much remains to be understood quantitatively about tropospheric gravity wave sources and generating mechanisms as well as their influences at greater heights, however.

Gravity waves are known to be a major component of the middle atmosphere motion field due to their amplitude growth with height. The thermal structure

Reproduced with permission of the copyright owner. Further reproduction prohibited without permission.

and circulation of the atmosphere at these heights are controlled to a large degree by the transports of energy and momentum by gravity waves and the processes acting to limit their amplitudes (Lindzen, 1981; Holton, 1982). Modeling studies of gravity wave effects at these heights have assumed either zonal components (Holton, 1982) or isotropic phase velocity distributions (Holton and Zhu, 1984), with wavelengths and wave amplitudes specified such that the waves break in the mesosphere. This assumes that the major wave generating processes occur in the troposphere and lower stratosphere enabling geostrophic adjustment to have an important role (Zhu, 1987). Rind *et al.* (1988) applied a wave breaking scheme to a global general circulation model (GCM) with gravity waves generated in the lower troposphere and found that gravity waves can propagate to the stratosphere and mesosphere before breaking. Reviews of middle atmosphere gravity waves and their effects include those by Hines *et al.* (1974), Fritts (1984*a*, 1989) and Dunkerton (1989).

Attention has turned recently to gravity wave sources in the troposphere due to improved observations and theoretical studies showing their importance at higher levels. It is the troposphere that is believed to contain a majority of the main sources and generation processes among the different atmospheric regions. The processes thought to be important include topography, convective activity, wind shear, frontal motions and geostrophic adjustment. Numerous studies have treated topographic generation (Lilly and Kennedy, 1973; Smith, 1985; Nastrom *et al.*, 1987; McFarlane, 1987; Hines, 1988; Jasperson *et al.*, 1990; and Nastrom and Fritts, 1991), convective and frontal activity (Stobie *et al.*, 1983; Lu, *et al.*, 1984; Pfister *et al.*, 1986; Clark *et al.*, 1986; Gall *et al.*, 1988; Hauf and Clark, 1989;

Reproduced with permission of the copyright owner. Further reproduction prohibited without permission.

Vincent and Eckermann, 1990; and Fritts and Nastrom, 1991) and wind shear excitation (Lalas and Einaudi, 1976; Mastrantonio *et al.*, 1976; Fritts, 1982, 1984*b*; Chimonas and Grant, 1984; and Danielsen *et al.*, 1991) due to their clear association with wave activity. It also happens that these sources tend to produce the higher intrinsic frequency ($\omega \gg f$, where ω and f are the intrinsic and inertial frequencies) gravity waves. The likelihood of generating low frequency gravity waves from these sources is less certain. Yet observations reveal clearly that a large fraction of gravity wave energy is contributed by motions near the inertial frequency (Balsley and Carter, 1982; Meek *et al.*, 1985; Hirota and Niki, 1986; and Kwon *et al.*, 1990). Thus, it is plausible to expect generation processes of gravity waves at low frequencies, with geostrophic adjustment a possibly major contributor.

Geostrophic adjustment as a mechanism to explain the geostrophic balance of large scale motions in the atmosphere and ocean has been suggested since 1938 (Rossby, 1938). Previous works on geostrophic adjustment processes concerned primarily the adjustment time scales and the mean fields and energy repartition after the adjustment (Blumen, 1972; Middleton, 1986). Applications also included initialization and assimilation of observed data during the numerical prediction by using geostrophic adjustment to isolate the inertio–gravity waves (denoted IGWs) (Charney, 1955; and Phillips, 1963). The emphasis in this thesis, in contrast, is on geostrophic adjustment as an excitation mechanism of IGWs in the atmosphere. Thus, the results presented here will discuss IGW characteristics under different initially unbalanced conditions and their relevance to the atmospheric gravity wave spectrum.

Reproduced with permission of the copyright owner. Further reproduction prohibited without permission.

Low frequence gravity waves are observed ubiquitously as the dominant motions over the mesoscale range owing to their large contributions of the energy. Fig. 1.1 exhibits one of the observations for such nature in the lower atmosphere by MST (Mesosphere–Stratosphere–Troposphere) radar at Poker Flat, Alaska. The intrinsic frequence of gravity wave ω is bounded by $\mid f \mid < \mid \omega \mid < N$ according to the linear theory shown in chapter 2. As we can see from Fig. 1.1, lower frequency motions contribute most energy. IGWs associated with jet streams have been observed by many authors as well (see Hirota and Niki, 1986; and Uccellini and Koch, 1987). Using the MU (Middle and Upper Atmosphere) radar, Hirota and Niki (1986) found IGWs propagating upward to the stratosphere and downward to the troposphere, during a strong tropopause jet. Observations also show gravity waves propagating largely on meridional direction (Fritts, 1984*a*). Theoretical efforts addressing the generating processes of those low frequency gravity waves, however, are much less comprehensive.

To measure the ageostrophic modes embedded in the atmospheric jet streams is not an easy task. However, some previous case studies do help us to describe such an unbalanced flow. A magnitude of ageostrophic motions larger than $10m/s$ associated with the tropospheric jet stream has been documented by Uccellini *et al.* (1984), Uccellini and Kocin (1987), and Cammas and Raymond (1989). In particular, by analyzing data that were assimilated by the European Centre for Medium–Range Weather Forecast (ECMWF) schemes, Cammas and Raymond (1989) noted a particular ageostrophic pattern scaled $\sim 2-3km$ vertically and $\sim$ 10 to 20 times larger than the vertical one on the cross–jet direction in the upper–tropospheric jet. With these knowledge, a particular initially unbalanced

Reproduced with permission of the copyright owner. Further reproduction prohibited without permission.

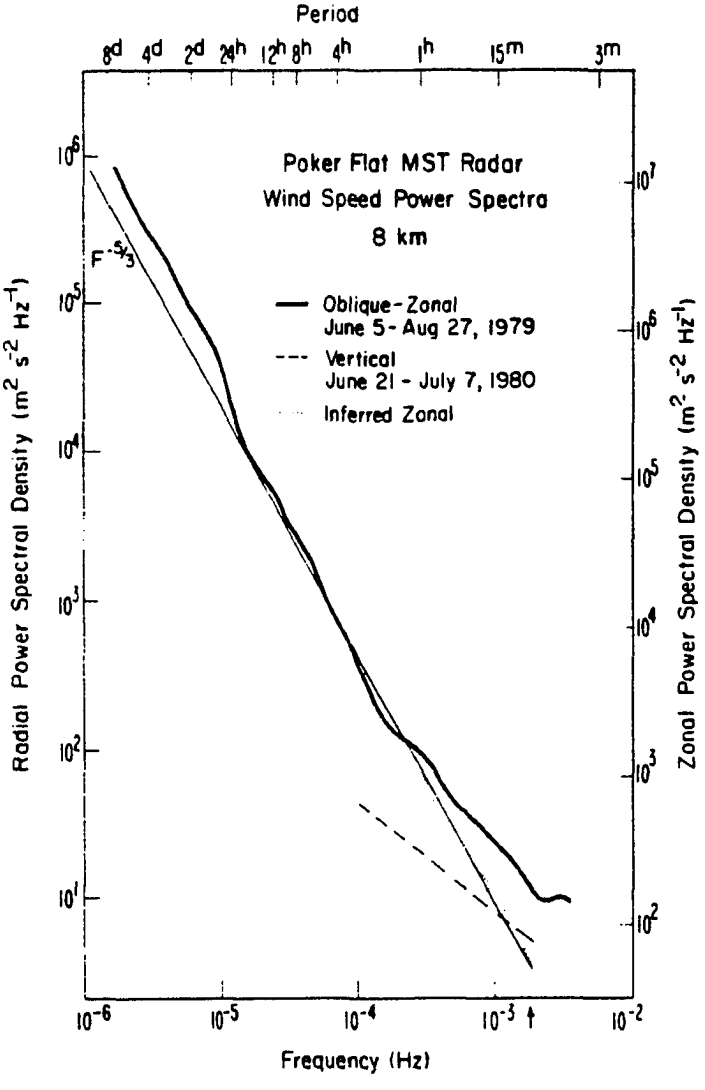

Figure 1.1 Power spectrum of the wind fluctuations at 8.1 km obtained using the Poker Flat MST radar in Alaska (oblique spectrum=solid lines; vertical spectrum represented by the dashed line). The arrow marks the nominal value of N. The dashed line represents a power law slope of $f^{-5/3}$. The left-hand ordinate is scaled in "radial" power density (i.e., along the antenna beam), while the right-hand ordinate is scaled in inferred zonal wind power density (*after Balsley and Carter. 1982).*

Reproduced with permission of the copyright owner. Further reproduction prohibited without permission.

momentum source in association with the jet stream can be constructed. The objective of this thesis is to determine whether the IGWs radiated by an idealized geostrophic adjustment process can reasonably account for such atmospheric observations.

In this thesis, the ageostrophic component of the jet stream is specified to have Gaussian structure. IGWs radiating from this initially unbalanced momentum are investigated assuming geostrophic adjustment to be the source mechanism. Fourier integral and Green's function techniques are employed to solve this problem. Numerical computations are also involved to value the multiple integrals. The organization of this thesis is as follows. A brief review of geostrophic adjustment concepts and gravity wave dynamics is given in chapter 2. Chapter 3 will address the radiating IGWs during the process of geostrophic adjustment of an infinite two–dimensional Gaussian jet by considering the ageostrophic component separately as an initial unbalance field. The analysis is extended to a three–dimensional adjustment problem corresponding to a localized Gaussian ageostrophic jet in chapter 4. The conclusions are presented in chapter 5. IGW generators appropriate to the geostrophic adjustment and Green's function problems in three dimensions are presented in the appendices.

Reproduced with permission of the copyright owner. Further reproduction prohibited without permission.

Chapter 2

Major Observed Atmospheric Motions and Basic Gravity Wave Dynamics

The fundamental atmospheric motions can be distinguished in terms of their different propagation mechanisms. There are acoustic waves, which result from the compressibility of the fluid, gravity waves, which are possible when the atmosphere is stably stratified so that a fluid parcel displaced vertically will experience a restoring force towards its equilibrium position, and Rossby waves or planetary waves, which require absolute vorticity conservation and are maintained by a variable Coriolis force or β effects ($\beta \equiv \partial f/\partial y$, y directed northward). Each of these motions exhibits structure, propagation, and effects in the atmosphere that depend on a dispersion relation and the physical state and character of the atmosphere through which it propagates.

2.1 Geostrophic Balance and Geostrophic Adjustment

In spite of the broad spectrum of motions in the atmosphere, the principal observed atmospheric flows at large scales are geostrophic, in which Coriolis and

Reproduced with permission of the copyright owner. Further reproduction prohibited without permission.

pressure gradient forces are balanced. Why this phenomenon stands is one of the most important fundamental dynamics problems, with three individual theories proposed to account for this state.

The first is the geostrophic adjustment mechanism. It states that extra (not geostrophically balanced) energy, momentum, or mass somehow will be redistributed, with extra energy and momentum radiated away by IGWs, leaving a mean state in geostrophic balance. Such geostrophic balance has been frequently observed. The concepts of geostrophic adjustment were originally posed by Rossby (1938) and Cahn (1945) in considering the geostrophically balanced flow in the ocean and atmosphere. Rossby introduced a parameter (called radius of deformation) defined as the ratio of long wave phase speed to Coriolis parameter to judge the conditions under which geostrophic adjustment might occur. However, instead of estimating the radiating waves from the unbalanced region explicitly, Rossby argued that the inertial oscillation of a balanced current implied the occurrence of adjustment.

A second theory involves a baroclinic instability explanation. It declares that geostrophic balance is merely a reflection of large–scale baroclinic instabilities which are basically quasi–geostrophic (Tanaka and Sun, 1990). This includes conventional baroclinic instability supported by the available potential energy of an unperturbed zonal flow due to the sloping mean density surface (Eady, 1949) and symmetric instability (no longitudinal variations) supported by the kinetic energy of an unperturbed zonal flow (Eady, 1949; and Stone, 1966, 1978).

A third theory is the geostrophic momentum approximation which is based on the rate of change of momentum being much smaller than the Coriolis force,

Reproduced with permission of the copyright owner. Further reproduction prohibited without permission.

permitting advected momentum to be well approximated by its geostrophic value (Hoskins,1975). Nevertheless, since geostrophically balanced motions are not a complete set of atmospheric motions, it is important to point out that the last two theories exclude *a priori* mesoscale motions by assuming a Rossby number $R_0 = \mid d\vec{V}/dt \mid / \mid f\vec{V} \mid \ll 1$.

One thing which is clear and important is that the geostrophic adjustment mechanism helps us to understand how the momentum and mass field adjust to each other in the atmosphere and the ocean. Thus, it is possible for us to view the large scale atmospheric motions as consisting of two components: a quasi–geostrophic or balanced state which describes the evolution of large scale features and an unbalanced component which incorporates both adjustment processes of the large–scale motion field and inertio–gravity wave structures with small–scale and large–scale energy sources.

Geostrophic adjustment processes are usually catalogued more informatively as barotropic and baroclinic geostrophic adjustments in a barotropic or baroclinic atmosphere. The adjustment processes will not occur unless IGWs act as a vehicle to carry the ageostrophic energy away. This is the original physics view which also can be proved mathematically (Zeng, 1978). Consequently, it is plausible to expect that geostrophic adjustment processes act as a source mechanism of low–frequency gravity waves.

Most previous studies of geostrophic adjustment have dealt with barotropic geostrophic processes and attempted to identify the resulting geostrophically balanced state, the adjustment timescale and energy partition between balanced and unbalanced motions (Rossby, 1938; Veronis, 1956; Phillips *et al.*, 1960; Blumen,

Reproduced with permission of the copyright owner. Further reproduction prohibited without permission.

1972; Middleton, 1986). Barotropic geostrophic adjustment processes, according to Obukhov's classical conception (Obukhov, 1949), allows for radiation of external gravity waves only because it assumes "shallow water" type dynamical equations. It thus excludes internal gravity waves *a priori*. In fact, barotropic studies have dominated geostrophic adjustment research. More recently, however, some studies in the atmosphere and ocean have considered 2-layer or fully baroclinic geostrophic adjustment to address the energy redistribution between wave field and mean states in a barotropic and a baroclinically unstable fluid (Blumen, 1972; Schubert *et al.*, 1980; Van Tuyl and Young, 1982; Duffy, 1990).

Of particular interest to baroclinic geostrophic adjustment, Van Tuyl and Young (1982) applied a two-layer hydrostatic and adiabatic model to examine the ageostrophic modes arising from nonlinearity and examined the possible effects of the background on the initial unbalance in a propagating jet maximum. They noted that the amplitudes of the unbalanced motions increase with the square of the Rossby number, particularly around and just downstream of the jet core. Walterscheid and Boucher (1984) investigated the responses to momentum and heating sources in a stratified isothermal thermosphere utilizing a two-dimensional model which included compressibility and rotation and noted that more initial energy went to IGWs in the cases of shallow momentum and deep thermal forcings. Schubert *et al.* (1980) simulated a geostrophic adjustment process in an axisymmetric vortex and found the majority of energy to be partitioned to IGWs. Zhu and Holton (1987) examined the role of geostrophic adjustment in the middle atmosphere by means of checking the response of a localized gravity wave packet forcing as a local momentum source. Only those studies by Walterscheid and

Reproduced with permission of the copyright owner. Further reproduction prohibited without permission.

Boucher (1984) and Zhu and Holton (1987) attempted to look closely at the transient state (emerging wave field). Yet it appears important to investigate other possible processes serving as source process of low–frequency gravity waves. The goal of this thesis is to provide a more explicit description of the transient fields radiated from ageostrophic atmospheric jet streams.

2.2 Gravity Wave Generation

Basic understanding of atmospheric gravity wave dynamics requires an understanding of two issues: how has the wave been generated and in what manner does the wave propagate? When the atmosphere is stably stratified, which is the case under most times and circumstances, a fluid parcel displaced vertically will experience a buoyancy force due to gravity, and will oscillate around its original position and influence neighbouring parcels to oscillate in a manner described by the equations of motions. There are two categories of gravity waves: i) external gravity waves which occur at fluid boundaries or interfaces, such as the free surface of the ocean or the interior of a fluid with a severe density discontinuity and, ii) internal gravity waves which may occur in the absence of boundaries.

To further quantify the effects of a displaced fluid parcel, imagine a parcel initially with the same pressure, temperature, and density as its surroundings to experience a small vertical displacement. If the parcel is displaced such that the pressure is different from the equilibrium value at its new location, the motion will be primarily acoustic in character. On the other hand, if the pressure field is balanced, then density and temperature fluctuations will occur if the motion is adiabatic and the motion will couple best with gravity wave motions. As illustrated

Reproduced with permission of the copyright owner. Further reproduction prohibited without permission.

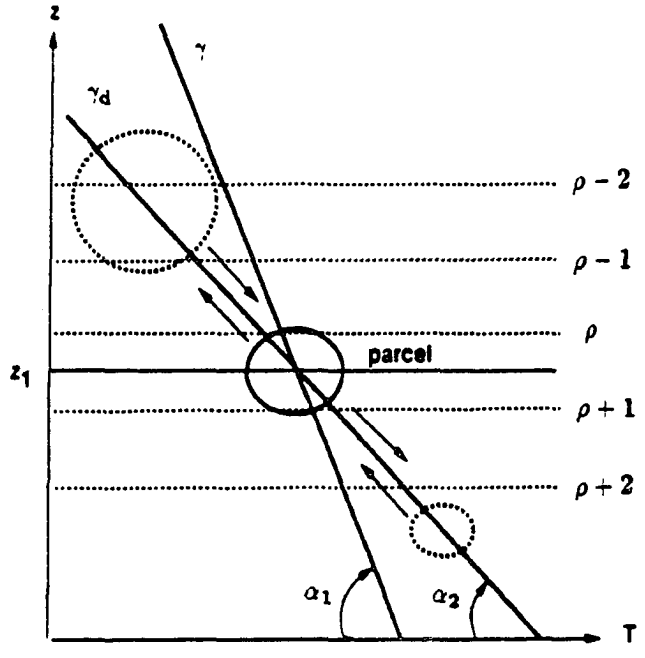

Figure 2.1 Parcel motion of gravity wave. A fluid parcel feels a buoyancy force and results in oscillation after the disturbance. Assuming this is an adiabatic process, arrows indicate the parcel's motions, where γ is a typical lapse rate, γ_d $(= g/c_p)$ is the adiabatic lapse rate, and T is temperature. Profiles of γ, γ_d and ρ (density) represent the stably stratified atmosphere. $\alpha_1 = \tan^{-1}[dz/(-dT)] = \tan^{-1}(1/\gamma), \alpha_2 = \tan^{-1}(1/\gamma_d)$.

in Fig. 2.1, a parcel initially at $z = z_1$ having the same thermal and dynamical character as its environment now moves vertically to $z = z_1 + \delta z$. The background stably stratified structure is represented by profiles of γ ($\sim 6.5\,°C/km$), a typical lapse rate, and γ_d ($\sim 9.8\,°C/km$), the adiabatic lapse rate of dry air and those constant density lines. The parcel's thermal character is determined by the γ_d profile during the motion because of being considered an adiabatic process. The parcel becomes cooler (warmer) when it moves upwards (downwards) and thus it is heavier (lighter) than its surroundings and results in an acceleration towards its original position at level z_1 through the buoyancy force. The overshooting as

Reproduced with permission of the copyright owner. Further reproduction prohibited without permission.

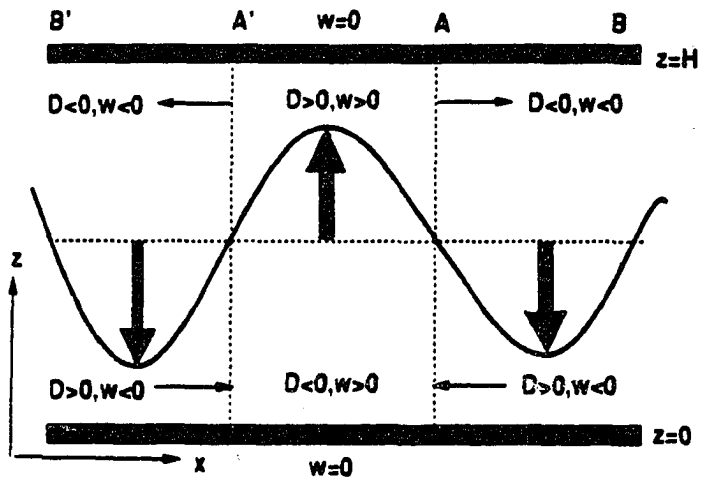

Figure 2.2 Generation and propagation of gravity wave. Gravity wave generated after an initial upward disturbance in column A'A. z=0 and z=H are solid lids. D = $\partial u/\partial x$ is horizontal divergence. Thin dot lines show geometry centers and column boundaries. Thin arrows present converging motions of the fluid. Blunt arrows show the perturbations of vertical velocity. The solid line indicates a typical wave disturbance.

it returns results in an oscillation about its initial level. Since the buoyancy force provides the restoring force, the name buoyancy wave has been suggested.

An illustration of gravity wave propagation is provided in Fig. 2.2. To simplify the description, incompressible motion is assumed. Let's restrict ourselves to a horizontal-vertical (x, z) plane with fixed boundaries at $z = 0$ and $z = H$. This situation will be the same as in the real atmosphere if we think that $z = 0$ is the ground, and $z = H$ is an upper limit at large distance. An incompressible fluid has a continuity equation

$$\frac{\partial u}{\partial x} + \frac{\partial w}{\partial z} = 0, \tag{2.1}$$

Reproduced with permission of the copyright owner. Further reproduction prohibited without permission.

where u, w are perturbation velocity components in the x and z directions. Define horizontal divergence D to be

$$D \equiv \frac{\partial u}{\partial x}. \tag{2.2}$$

In column A'A (Fig. 2.2), an initial motion towards to $z = H$ ($z = 0$) where $w = 0$ results in $\partial w/\partial z < 0$ (> 0) in the upper level (lower level). And thus $D > 0$, ($D < 0$, convergence). The divergence–convergence distributions of A'A determine the divergence patterns in the undisturbed neighbourhood columns B'A' and AB, and thus cause vertical motions in those areas as indicated in Fig. 2.2, causing gravity wave propagation horizontally and parcel oscillation in horizontal and vertical directions.

Fig. 2.3 (Kundu, 1990) shows the internal gravity waves' propagation from a periodic source in the absence of rotation in a laboratory facility. The source is at the center of the figure and wave energy is propagating away (the beams). Since the frequency of source has been fixed at $0.71\, rad/s$, only those positions along the beams are affected by the waves. The phase and group velocities can be explained by eqs. (2.17)–(2.19).

Dynamically, gravity waves are generated in one of several ways: instability or forcing. The most discussed instability in the wave excitation issue is that of a horizontally uniform flow with vertical gradients of wind and/or buoyancy. Among these are the buoyant or convective instability, the inertial–buoyancy or symmetric instability, and the shearing type including the Kelvin–Helmholtz instability. The last has received the most attention as a gravity wave generation mechanism in the literature (Gossard and Hooke, 1975; Stobie *et al.*, 1983; and Fritts, 1984*a*). The first two instabilities are less understood. In the case of waves generated by shear

Reproduced with permission of the copyright owner. Further reproduction prohibited without permission.

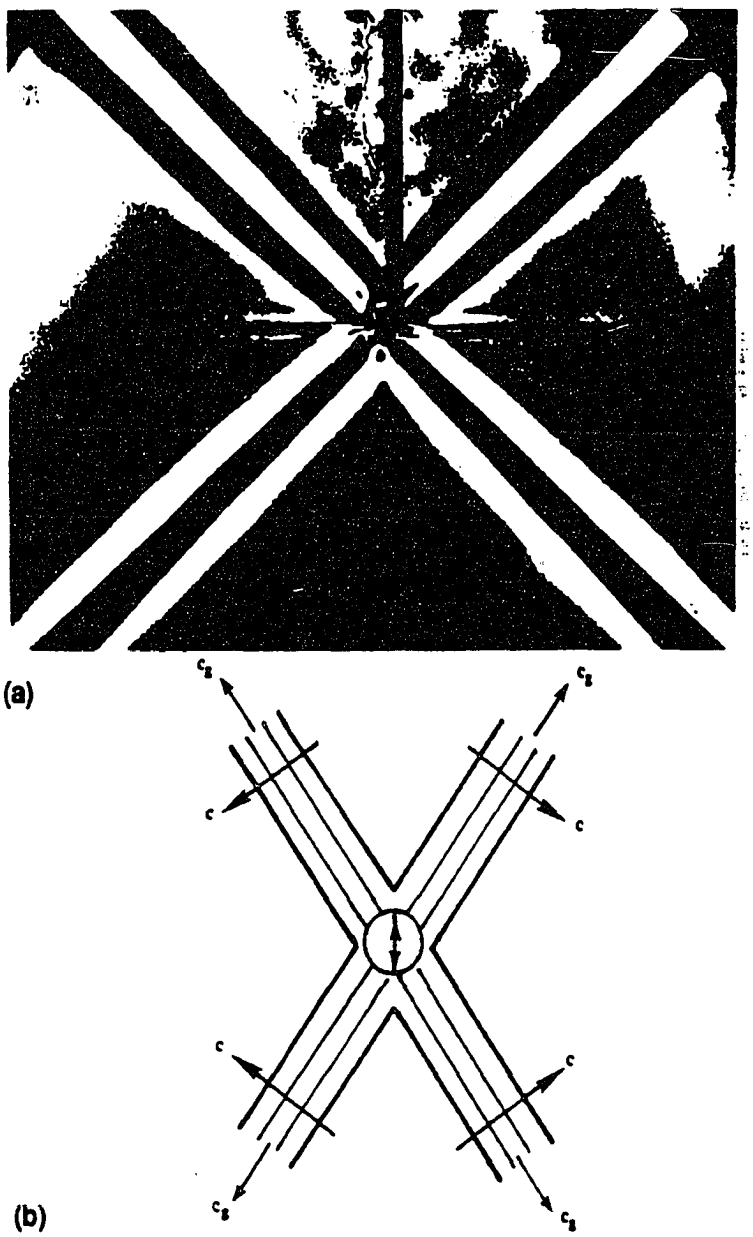

Figure 2.3 Gravity waves generated in a stratified fluid of uniform buoyancy frequency N=1 rad/s. The forcing agency is a horizontal cylinder, with its axis perpendicular to the plane of the paper, oscillating vertically at frequency ω=0.71 rad/s. The vertical dark line in the upper half of the photograph (a) is the cylinder support and should be ignored. The light and dark radial lines represent contours of constant perturbation density and are therefore constant phase lines. The schematic diagram (b) below the photograph shows the directions of phase and group velocities for the four beams (*after Kundu, 1990*).

Reproduced with permission of the copyright owner. Further reproduction prohibited without permission.

instability, energy of the shear flow is converted into wave energy contained in initially small fluctuations in the wave field. To address these physical processes, linear and nonlinear theories have been developed mathematically with the treatments of initial–value, boundary–value and nonhomogeneous terms depending on different physical considerations (for example, Lee and Beardsley, 1974; Chimonas and Grant, 1984).

2.3 Dispersion Relation of Internal Gravity Waves

It is the intent here to review the internal gravity wave character and some frequently used dynamical approximations through examining the gravity wave dispersion relation. A gravity wave is a hydrodynamic motion and thus is governed by the fluid dynamic equations which describe the conservation of momentum, mass and energy. These equations are completed here by using the ideal gas law. With the adiabatic assumption, the full set of equations is presented by eqs. (A.1)–(A.6) in Appendix A by letting $\eta = 0$ and $\varepsilon_h = \varepsilon_c = 1$. Linearizing the equations, neglecting the small terms, and writing the variables in terms of the decreasing density in the atmosphere yield

$$\tilde{u} = (\frac{\bar{\rho}}{\rho_0})^{1/2} u'; \qquad \tilde{v} = (\frac{\bar{\rho}}{\rho_0})^{1/2} v'; \qquad \tilde{w} = (\frac{\bar{\rho}}{\rho_0})^{1/2} w';$$

$$\tilde{\pi} = (\frac{\bar{\rho}}{\rho_0})^{1/2} c_p \bar{\theta} \pi'; \qquad \tilde{\theta} = (\frac{\bar{\rho}}{\rho_0})^{1/2} \frac{g}{\bar{\theta}} \theta', \tag{2.3}$$

where $\pi = (p/p_0)^{R/c_p}$, and c_p is the specific heat at constant pressure. Introducing the Galilean transformation (Yeh and Liu, 1972)

$$\vec{r}^* = \vec{r} - \vec{V} t; \qquad t^* = t \tag{2.4}$$

Reproduced with permission of the copyright owner. Further reproduction prohibited without permission.

where $\vec{\bar{V}} = \{\bar{u}, \bar{v}, 0\}$, the equations become

$$\frac{\partial \tilde{u}}{\partial t} + \frac{\partial \tilde{\pi}}{\partial x} - f\tilde{v} = 0, \tag{2.5}$$

$$\frac{\partial \tilde{v}}{\partial t} + \frac{\partial \tilde{\pi}}{\partial y} + f\tilde{u} = 0, \tag{2.6}$$

$$\frac{\partial \tilde{w}}{\partial t} + \frac{\partial \tilde{\pi}}{\partial z} + \Gamma\tilde{\pi} - \tilde{\theta} = 0, \tag{2.7}$$

$$\frac{\partial \tilde{\theta}}{\partial t} + N^2\tilde{w} = 0, \tag{2.8}$$

$$\frac{1}{C_s^2}\frac{\partial \tilde{\pi}}{\partial t} + \frac{\partial \tilde{u}}{\partial x} + \frac{\partial \tilde{v}}{\partial y} + \frac{\partial \tilde{w}}{\partial z} - \Gamma\tilde{w} = 0, \tag{2.9}$$

where $C_s = (c_p\bar{T}/c_v)^{1/2}$ is the speed of sound, c_v is the specific heat at constant volume, and $\Gamma = (1/2\bar{\rho})(d\bar{\rho}/dz) + g/C_s^2 = -(1/2\bar{\rho})(d\bar{\rho}/dz) - (1/\bar{\theta})(d\bar{\theta}/dz)$. Eqs. (2.5)–(2.9) appear to represent waves in a motionless atmosphere, but are transformed to remove the dependence on a mean wind. Assuming all perturbations can be composed of monochromic waves with

$$\psi = \psi_0 e^{i(kx+ly+mz-\omega t)}, \tag{2.10}$$

and substituting into eqs. (2.5)–(2.9), the only possibility for a non–trivial solution is that

$$\begin{aligned} &C_s^{-2}\omega^4 - \omega^2[k^2 + l^2 + m^2 + \Gamma^2 + (\frac{N}{C_s})^2 + (\frac{f}{C_s})^2] \\ &+N^2(k^2 + l^2) + f^2[m^2 + \Gamma^2 + (\frac{N}{C_s})^2] = 0, \end{aligned} \tag{2.11}$$

where $\{k, l, m\}$ (denotes as $\vec{\kappa}$ below) is the wave vector in the x, y and z coordinate system.

Eq. (2.11) is the dispersion relation of internal gravity waves. Note here that frequency ω is in new coordinates (moving with the current) and is called the intrinsic frequency. It has the relationship with the frequency ω_o given by

$$\omega = \omega_o - \vec{\kappa} \cdot \vec{\bar{V}}, \tag{2.12}$$

Reproduced with permission of the copyright owner. Further reproduction prohibited without permission.

where ω_o is called the observed frequency.

2.3.1 Rotation and Compressibility Effects

Some of the most commonly applied approximations for gravity wave dynamics in the atmosphere are irrotational, incompressibility and hydrostatic approximations. The first two will be discussed here by analyzing the dispersion relation while the last will be considered in section 3.5.

The internal gravity wave dispersion relation under the non-rotating and incompressible approximations can be achieved by setting $f = 0$ and $C_s \to \infty$ ($\delta\rho \to 0$ in the incompressible fluid) in eq. (2.11), which results in

$$C_s^{-2}\omega^4 - \omega^2[k^2 + l^2 + m^2 + \Gamma^2 + (\frac{N}{C_s})^2] + N^2(k^2 + l^2) = 0, \qquad (2.13)$$

and

$$\omega^2[k^2 + l^2 + m^2 + \Gamma_i^2] - N^2(k^2 + l^2) - f^2[m^2 + \Gamma_i^2] = 0, \qquad (2.14)$$

where $\Gamma_i = (1/2\bar{\rho})(d\bar{\rho}/dz)$.

Eqs. (2.11), (2.13) and (2.14) have been plotted in the wavenumber domain in Fig. 2.4. Since waves are symmetric horizontally, only the (k, m) plane is presented, choosing $l = 0$. It can be seen from Fig. 2.4 (a) that rotational effects on gravity wave structure can be quite large when the wave frequencies approach f. As ω increases to $10f$ or larger, the earth's rotational influence will be negligible. When the frequency is low, the effect of rotation is to steepen the wave phase slopes. As a result, for the same frequency wave, wave energy is propagated more horizontally in the presence of rotation. The influence of compressibility of the atmosphere is indistinguishable over all gravity wave scales when the wave frequency is low (the very large vertical wavelength case is discussed below). A

Reproduced with permission of the copyright owner. Further reproduction prohibited without permission.

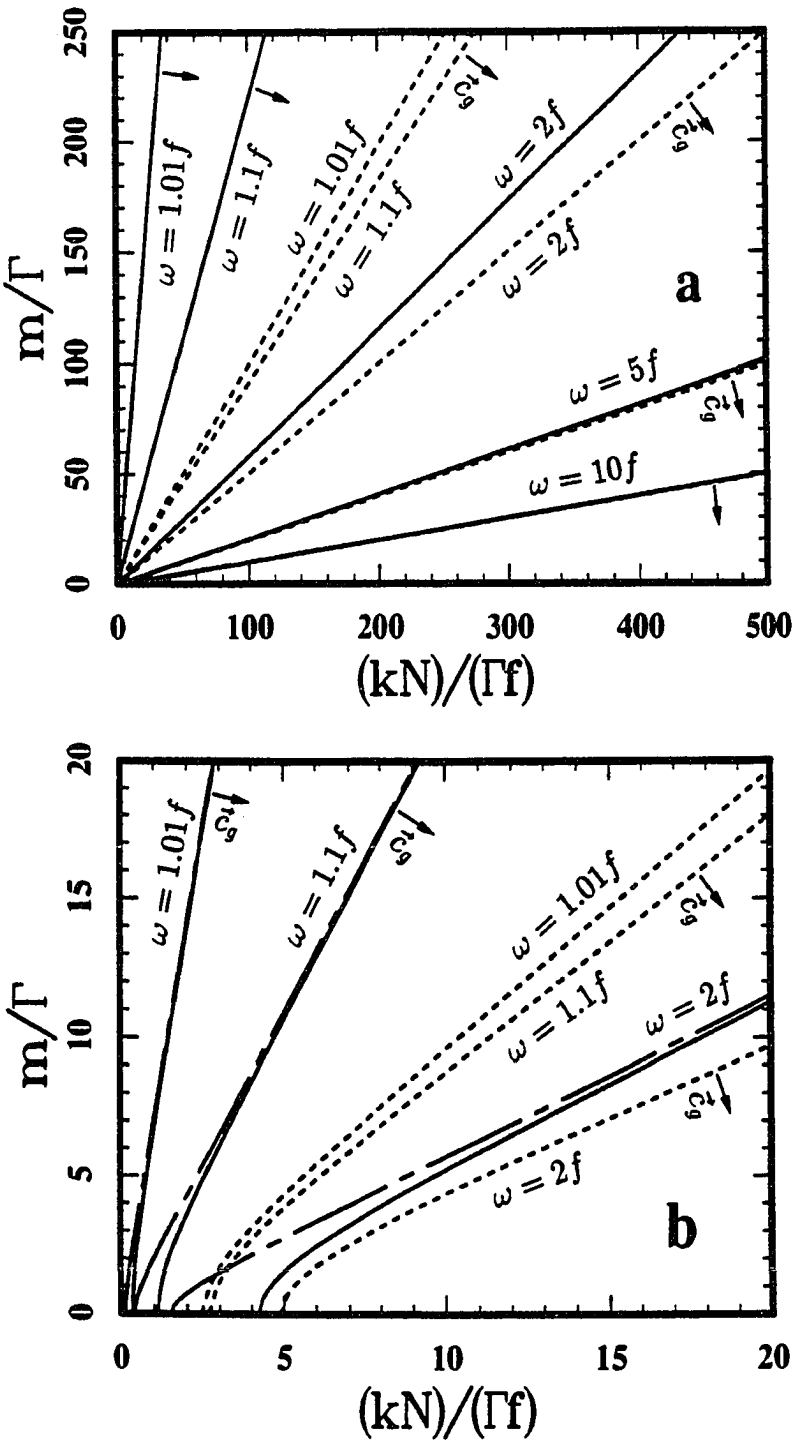

Figure 2.4 Internal gravity wave dispersion relation on (k,m) plane with l=0, Γ=0.027/km, N=0.02 rad/s and f=10^{-4}rad/s. Arrows indicate directions of the group velocities. Solid lines represent the compressible, rotating case; dashed lines are for compressible but non–rotating motions; chain dashed lines are for incompressible but rotating. Chain dashed lines are merged in solid lines in (a). (b) is same as (a) but with more detail for small wave numbers.

Reproduced with permission of the copyright owner. Further reproduction prohibited without permission.

comparison of eqs. (2.11) and (2.14) indicates that even as ω increases to $\sim 30f$, the completely incompressible approximation remains $\sim$ 99% accurate over all wave scales. Fig. 2.4(b) is the same as Fig. 2.4(a) but shows more detail at small wavenumbers. As we can see, the incompressible assumption has large departures from the compressible case as frequency and vertical wavelength increase. When the vertical wavelength is much larger than the scale height (taking $H \sim 8km$ here), the wave structure will be distorted by assuming incompressibility. This implies that compressible effects must be included to properly describe such large vertical scale motions. However, gravity wave having very large vertical wavelength (for instance, $m/\Gamma = 10$ in Fig 2.4(b), is equivalent to 23 km) is very difficult to survive in the atmosphere (see Lindzen, 1981).

2.3.2 Low Frequency Motions

Let us turn now to the low–frequency gravity waves since it is the goal of this research to provide a theoretical explanation of the low–frequency gravity waves observed in association with atmospheric jet streams. For this purpose, the incompressible assumption is assumed while keeping the rotational terms. The further assumption is that the background density is constant, except in the buoyancy term. Eq. (2.11) reduces as

$$\begin{aligned} \omega^2 &= \frac{f^2m^2 + N^2(k^2+l^2)}{k^2+l^2+m^2} \\ &= f^2 + \frac{(N^2-f^2)(k^2+l^2)}{k^2+l^2+m^2} \\ &= N^2 - \frac{(N^2-f^2)m^2}{k^2+l^2+m^2}. \end{aligned} \tag{2.15}$$

Reproduced with permission of the copyright owner. Further reproduction prohibited without permission.

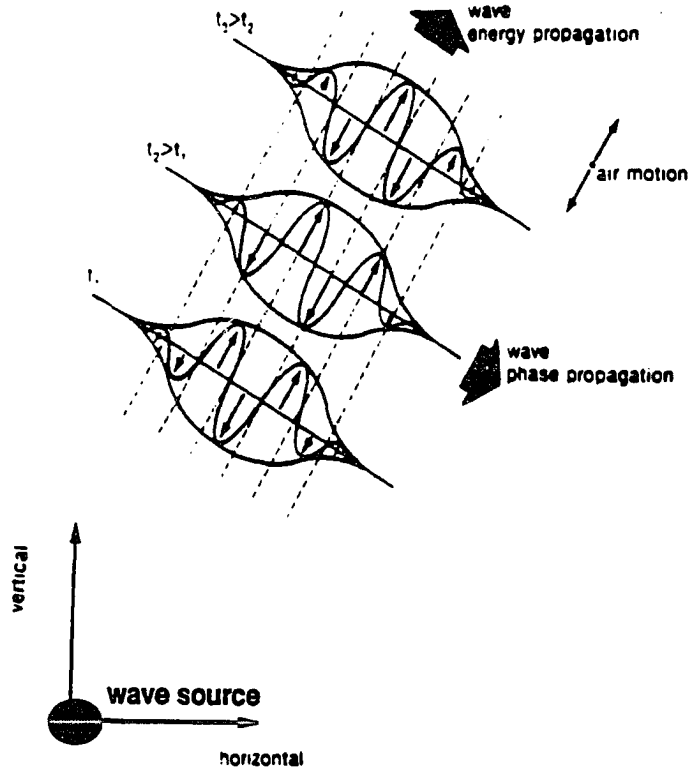

Figure 2.5 Phase and energy propagation of an internal gravity wave from a source in the atmosphere (*after Hooke*, 1986).

It is obvious that gravity wave frequencies are bounded by f and N as

$$| f | < | \omega | < N. \tag{2.16}$$

Phase and group velocities are derived immediately from eq. (2.15) (Lighthill, 1964)

$$\vec{c}_p = \{\frac{\omega k}{k^2+l^2+m^2}, \frac{\omega l}{k^2+l^2+m^2}, \frac{\omega m}{k^2+l^2+m^2}\}, \tag{2.17}$$

and

$$\vec{c}_g = \{\frac{km^2(N^2-f^2)}{\omega(k^2+l^2+m^2)^2}, \frac{lm^2(N^2-f^2)}{\omega(k^2+l^2+m^2)^2}, -\frac{m(N^2-f^2)(k^2+l^2)}{\omega(k^2+l^2+m^2)^2}\}, \tag{2.18}$$

Reproduced with permission of the copyright owner. Further reproduction prohibited without permission.

such that

$$\vec{c}_p \cdot \vec{c}_g = 0. \tag{2.19}$$

Eq. (2.19) indicates that the propagation direction for wave energy is parallel to the wave phase front as shown in Fig. 2.3(b). This result applies for hydrostatic gravity waves as well. A two–dimensional schematic representation is given by Fig. 2.5 relating the wave source and wave phase and energy propagation in the atmosphere.

Reproduced with permission of the copyright owner. Further reproduction prohibited without permission.

Chapter 3

Inertio–Gravity Wave (IGW) Radiation from an Infinite Unbalanced Gaussian Jet

3.1 Introduction

Gravity waves with frequencies near f in the vicinity of the tropospheric jet stream have been revealed by various observations (Hirota and Niki, 1986). Gravity waves with frequencies between 1–4 h associated with a low–level jet corresponding with a squall line also have been documented by some authors (see Eom, 1975; and Uccellini and Koch, 1987).

Theoretical investigations on jet–stream excitation previously focused on wave–wave interaction and shear generation of gravity waves. Van Tuyl and Young (1982) employed a two–layer nonlinear primitive equation model assuming motion to be frictionless, adiabatic, hydrostatic and with constant f to examine the forced adjustment process of the a propagating jet streak. In their control run, a completely balanced system was given initially. With the resulting unbalanced vertical motions, they found that in the high Rossby number areas near the jet core, the secondary circulations predicted by quasi–geostrophic or balanced theories were

Reproduced with permission of the copyright owner. Further reproduction prohibited without permission.

unable to maintain the initial balance. Therefore, they argued that unbalanced motions should result in these areas. Further quantitative investigations of the arising ageostrophic modes should be pursued as they suggested. Shear instability as a gravity wave excitation mechanism by the jet stream has also been examined by some authors (see Mastrantonio *et al.*, 1976). By researching such wave characteristics as growth rate through analyzing the linear stability of a low level jet stream, they found gravity waves propagating vertically but apparently with higher frequencies. Actually, most results of models taking shear instability as a gravity wave generation mechanism showed much smaller wavelengths than found in observations (Lalas and Einaudi, 1976). Although a typical large vertical wavelength (a few times as large as the shear layer) can be achieved theoretically (Lalas and Einaudi, 1976), those small-scale motions predicted by shear instability theory associated with the jet are still not simple to explain (see Uccellini, 1975; Eom, 1975; and Uccellini and Koch, 1987). Also Einaudi *et al.* (1987) were able to show the gravity wave activities without the presence of a critical level by analyzing the MST radar data. With these understandings, it might be believable that some other wave excitation mechanism such as geostrophic adjustment is an important factor in the situations associated with jet streams.

To examine geostrophic adjustment as a wave source process, unbalanced energy or momentum has to be provided. The atmospheric jet stream is one of those locations believed to be important for the residence of an ageostrophic component. The atmospheric jet streams are characterized by having a length of thousands of kilometers, a width of hundreds to thousands and a depth of a few to tens of kilometers, with a vertical shear of $\sim$ 5–10 $ms^{-1}(km)^{-1}$, a lateral shear

Reproduced with permission of the copyright owner. Further reproduction prohibited without permission.

$\sim 5\ cms^{-1}(km)^{-1}$, and a core wind speed of $\sim 60\ ms^{-1}$ in the mesosphere and $\sim 30ms^{-1}$ in the troposphere. In the averaged circulation pattern, both zonal mean and temporally averaged flows display a low latitude westerly (eastward) jet stream and a polar front jet stream. However, on individual days there is considerable latitudinal variability of the jet streams, particularly in the western North American and western European sectors (Parker, 1987). Thus, the time–averaged jet stream is not well defined in these regions. Also the instantaneous view reveals that the maximum speed of the jet stream can be as large as double that of the averaged circulation pattern.

Because it is departures from balanced flow that we believe to be an important source of IGWs, the instantaneous structure of the jet stream is used in this research to specify the ageostrophic motions. The atmospheric jet stream is a site of considerable departure from geostrophically balanced flow (Kung and Tanaka, 1983). The ageostrophic component contains $\sim 10\%$ of the motion field in the jet stream, with much larger contributions at specific sites and times (Uccellini *et al.*, 1984; Uccellini and Kocin, 1987; and Cammas and Raymond, 1989). In this chapter, geostrophic adjustment and the radiation of IGWs by a two–dimensional (2–D) ageostrophic Gaussian jet (equivalent to saying that the ageostrophic Gaussian jet is infinitely long) is addressed. An extension of this study to a localized three–dimensional jet is presented in chapter 4.

3.2 Theory

Linearized theory is used to examined the geostrophic adjustment of an infinite 2–D unbalanced Gaussian jet stream in an unbounded atmosphere. It has been

Reproduced with permission of the copyright owner. Further reproduction prohibited without permission.

assumed here that motions are incompressible, adiabatic and Boussinesq. Also the ageostrophic jet has been treated as an imposed momentum source. Under these conditions, and neglecting quadratic terms in perturbation quantities, the adjustment process can be described in Cartesian coordinates, with the jet core along the x axis directed east, y to the north and z upward by the equations (see Appendix A)

$$\frac{\partial u}{\partial t} - fv = \eta F_x \delta(t), \tag{3.1}$$

$$\frac{\partial v}{\partial t} + \frac{1}{\rho_0}\frac{\partial p}{\partial y} + fu = 0, \tag{3.2}$$

$$\frac{\partial w}{\partial t} + \frac{1}{\rho_0}\frac{\partial p}{\partial z} - \frac{g}{\bar{\theta}}\theta = 0, \tag{3.3}$$

$$\frac{\partial v}{\partial y} + \frac{\partial w}{\partial z} = 0, \tag{3.4}$$

$$\frac{\partial \theta}{\partial t} + \frac{\bar{\theta}}{g}N^2 w = 0. \tag{3.5}$$

with the notation defined in Appendix A. Here $\eta F_x \delta(t)$ symbolizes a momentum source term and F_x is defined as

$$F_x = u_* exp[-(\frac{y^2}{2\sigma_y^2} + \frac{z^2}{2\sigma_z^2})], \tag{3.6}$$

where u_* is the maximum velocity of the momentum source having a dimension of speed, $\delta(t)$ has dimension of reverse of time, and σ_y and σ_z are prescribed constants.

Eqs. (3.1)-(3.5) describe a two-dimensional baroclinic geostrophic adjustment process. In this research, u_* =$10m/s$, $\sigma_y = 100km$, and $\sigma_z = 1km$ are imposed to represent a shallow ageostrophic departure from a balanced mean state (see Cammas and Raymond, 1989). Also, f and N are assumed to be constants with values of $10^{-4}rad/s$ representing the midlatitude areas and $10^{-2}rad/s$ approximating an averaged case for the stable atmosphere.

Reproduced with permission of the copyright owner. Further reproduction prohibited without permission.

3.3 Method of Numerical Approach

Analytic solutions for all field variables u, v, w and θ obtained in this and the next chapter (*i.e.* eqs. 3.15–18, 3.27–33 and 4.16–25) are expressed in terms of multiple infinite integrals over the wavenumber domain. These integrals have singularities at $(k, l, m) \rightarrow 0$. Also, the upper integration limits are infinite and cannot be computed numerically. To remove the irregular points, several means are possible. Mathematically, complex analysis permits us to construct contours and to integrate along these contours in cases where analytic solutions are possible. Alternatively, physics allows us to assess the wave scales which contribute, thus bounding the range of numerical integration. From eqs. (3.6) and (4.6), it can be suspected that no energy is contained at $k = l = m = 0$. With the aid of the integration scheme in the new IMSL computational packet subroutine named QAND, it is found that $(k, l, m) \in (0, +\infty)$ may be replaced by $(k, l) \in [2\pi \times 10^{-6}, 2\pi \times 0.1](km)^{-1}$ and $m \in [2\pi \times 10^{-4}, 2\pi \times 10](km)^{-1}$ resulting in almost identical solutions. Here, k, l, m are wavenumbers in the x, y, z directions as prescribed. This is consistent with our expectation that the radiating waves will have horizontal and vertical scales comparable to the initial disturbance.

3.4 Adjustment of Initial Unbalance I: Approximate Fourier Integral Solutions

One classical method to deal with geostrophic adjustment processes is to assume all the added energy appears at $t = 0$. To approximate this process, as a first step, the adjustment process and response to the initially unbalanced momentum of the infinite Gaussian jet stream might be restated mathematically by

Reproduced with permission of the copyright owner. Further reproduction prohibited without permission.

eqs. (3.1)–(3.5) with $\eta = 0$ and conditions $u(y, z, 0) = F_x$, and all other variables are zero initially. This is an initial–value problem mathematically. Initially, it is assumed that all the ageostrophic energy is associated with a spectrum of IGWs only. By doing this, the mathematical complexity is reduced to some degree while we still are able to see the wave field in detail subject to the above assumption.

After some algebra, eqs. (3.1)–(3.5) can be written for all field variables as (see eq. A.20 in appendix A, letting $\eta = 0, \partial/\partial x = 0$ and $\varepsilon_h = 1$)

$$L(u, v, w, \theta) = 0, \tag{3.7}$$

with an operator given by

$$L = \frac{\partial^2}{\partial t^2}\left(\frac{\partial^2}{\partial y^2} + \frac{\partial^2}{\partial z^2}\right) + N^2\frac{\partial^2}{\partial y^2} + f^2\frac{\partial^2}{\partial z^2}. \tag{3.8}$$

3.4.1 Mathematical Expressions of the Results

The procedure here is to use a Fourier transformation to express the problem in wavenumber space, apply the desired initial conditions there, then transform back to physical domain to achieve the final results. The Fourier transform pairs used in this analysis are defined as

$$\tilde{\psi}(\vec{\kappa}, t) = \frac{1}{(2\pi)^2}\int_{-\infty}^{+\infty}\int_{-\infty}^{+\infty}\psi(\vec{r}, t)e^{-i\vec{\kappa}\cdot\vec{r}}dydz, \tag{3.9}$$

and

$$\psi(\vec{r}, t) = \int_{-\infty}^{+\infty}\int_{-\infty}^{+\infty}\tilde{\psi}(\vec{\kappa}, t)e^{i\vec{\kappa}\cdot\vec{r}}dldm, \tag{3.10}$$

where ψ represents all field variables, $i = \sqrt{-1}$, $\vec{\kappa} = l\vec{i_2} + m\vec{i_3}$, $\vec{r} = y\vec{i_2} + z\vec{i_3}$, (i_2, i_3) are unit vectors in the meridional and vertical directions, and (l, m) are the meridional and vertical wavenumbers as defined previously.

Reproduced with permission of the copyright owner. Further reproduction prohibited without permission.

Substituting eq. (3.9) into eq. (3.7) yields

$$\tilde{\psi}'' + \frac{l^2N^2 + m^2f^2}{l^2 + m^2}\tilde{\psi} = 0. \tag{3.11}$$

The general solution to eq. (3.11) is

$$\tilde{\psi}(t, \vec{\kappa}) = A(\vec{\kappa})e^{i\omega t} + B(\vec{\kappa})e^{-i\omega t}, \tag{3.12}$$

where

$$\omega^2 = \frac{l^2N^2 + m^2f^2}{l^2 + m^2}, \tag{3.13}$$

is the dispersion relation for non-hydrostatic IGWs appropriate to this problem.

The initially unbalanced momentum occurs only in the zonal direction, which is $u(y, z, t = 0) = F_x$ with a meaning of momentum per unit mass. But as time evolves, the meridional component will be excited through the Coriolis effect and all fields will then exhibit IGW motions. Thus, specifying the zonal motion determines all other field variables through eqs. (3.1)–(3.5). Letting $\tilde{\psi}$ in eq. (3.11) be $\tilde{u}$ and solving eq. (3.9) with conditions $u(y, z, t = 0) = F_x$ and $u_t(y, z, t = 0) = 0$, we obtain

$$\tilde{u}(t, \vec{\kappa}) = \frac{u_*\sigma_y\sigma_z}{2\pi} exp[-(\frac{\sigma_y^2l^2}{2} + \frac{\sigma_z^2m^2}{2})]cos(\omega t). \tag{3.14}$$

Transforming back to the physical domain by using eq. (3.10) yields

$$\begin{aligned} u(y, z, t) &= \frac{2u_*\sigma_y\sigma_z}{\pi}\int_{0+}^{+\infty}\int_{0+}^{+\infty} exp[-(\frac{\sigma_y^2l^2}{2} + \frac{\sigma_z^2m^2}{2})] \\ &\quad \cdot cos(ly)cos(mz)cos(\sqrt{\frac{N^2l^2 + f^2m^2}{l^2 + m^2}}t)dldm. \end{aligned} \tag{3.15}$$

Reproduced with permission of the copyright owner. Further reproduction prohibited without permission.

The expressions for v, w, and θ may then be obtained from eqs. (3.1), (3.4), and (3.5) using eq. (3.15), with the results

$$v(y,z,t) = -\frac{2u_*\sigma_y\sigma_z}{\pi f}\int_{0+}^{+\infty}\int_{0+}^{+\infty}\sqrt{\frac{N^2l^2+f^2m^2}{l^2+m^2}}exp[-(\frac{\sigma_y^2l^2}{2}+\frac{\sigma_z^2m^2}{2})] \cdot cos(ly)cos(mz)sin(\sqrt{\frac{N^2l^2+f^2m^2}{l^2+m^2}}t)dldm, \quad (3.16)$$

$$w(y,z,t) = -\frac{2u_*\sigma_y\sigma_z}{\pi f}\int_{0+}^{+\infty}\int_{0+}^{+\infty}\sqrt{\frac{N^2l^2+f^2m^2}{l^2+m^2}}\frac{l}{m}exp[-(\frac{\sigma_y^2l^2}{2}+\frac{\sigma_z^2m^2}{2})] \cdot sin(ly)sin(mz)sin(\sqrt{\frac{N^2l^2+f^2m^2}{l^2+m^2}}t)dldm, \quad (3.17)$$

and

$$\theta(y,z,t) = -\frac{2u_*\sigma_y\sigma_zN^2\bar{\theta}}{\pi fg}\int_{0+}^{+\infty}\int_{0+}^{+\infty}\frac{l}{m}exp[-(\frac{\sigma_y^2l^2}{2}+\frac{\sigma_z^2m^2}{2})] \cdot sin(ly)sin(mz)[cos(\sqrt{\frac{N^2l^2+f^2m^2}{l^2+m^2}}t)-1]dldm. \quad (3.18)$$

3.4.2 Transient States

Unlike barotropic geostrophic adjustment processes which exclude internal gravity waves *a priori* and are less realistic in an unbounded atmosphere, the baroclinic geostrophic adjustment process allows for both external and internal modes. From the dispersion relation, eq. (3.13), the evolution of these motions with frequencies near the inertial, f, suggests that we refer to them as IGWs. The presence of such motions leads to substantial differences from the classical barotropic geostrophic adjustment problem.

From the solution expressions, eqs. (3.15–3.18), it can be seen that u and v are symmetric about the y and z axes, while w and θ are antisymmetric. Thus

Reproduced with permission of the copyright owner. Further reproduction prohibited without permission.

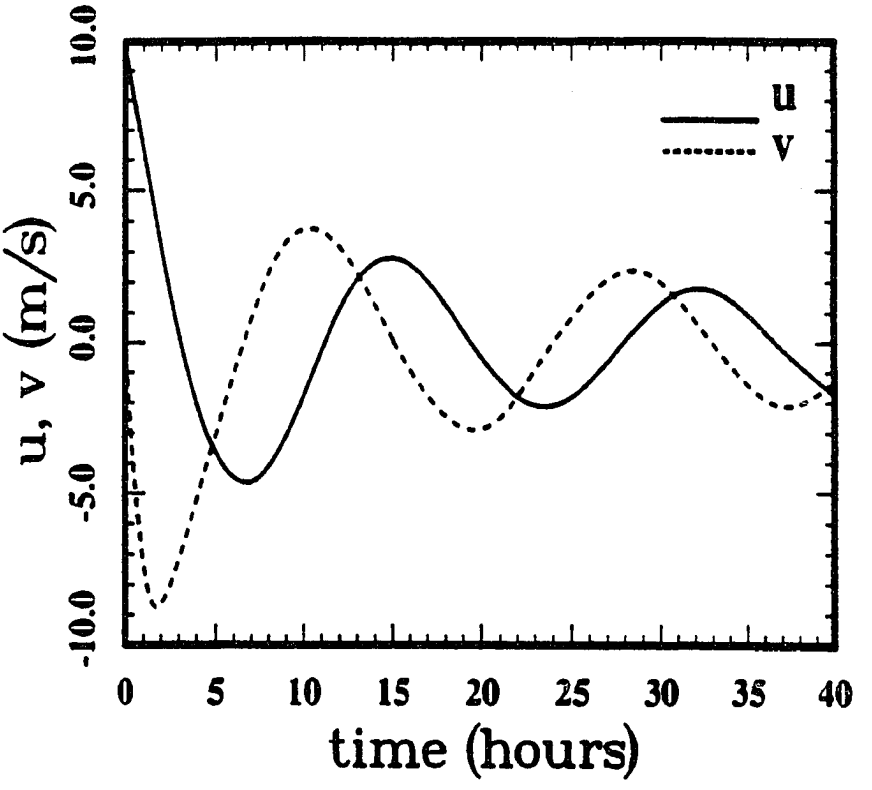

Figure 3.1 Perturbations of horizontal velocities at (y,z)=(0,0) km for the approximate Fourier integral solution. No mean state is excited.

it is necessary to compute the motion field in only one quadrant as a result and the rest of the fields can be derived. At the jet axis, $(y, z) = (0, 0)km$ in Fig. 3.1, we see only an inertial motion with a period given by $T_i = 2\pi/f$ (about 17 hours) exhibited by the horizontal motion field because of the symmetric initial disturbance resulting in the superposition of upward and downward propagating IGWs. This can also be seen from eqs. (3.17) and (3.18) mathematically from the antisymmetric character of w and θ about $y = z = 0$. The clockwise rotating maxima of horizonal velocities with time shows the influences of the Coriolis effect. This character will also be seen elsewhere in the wave field. The wave amplitudes

Reproduced with permission of the copyright owner. Further reproduction prohibited without permission.

decay after $\sim 2 - 3T_i$, indicating that much more time is needed for a baroclinic geostrophic adjustment process than for a barotropic case.

Away from the jet core, we begin to observe IGW character. At $(y, z) = (100, 1)km$, as shown in Fig. 3.2, the disturbances in w and θ clearly reveal IGW propagation through their variations. Fluctuations of w and v are positively correlated while downward motion ($w < 0$) causes adiabatic warming ($\theta > 0$) and *vice versa*. The amplitudes of u and v are comparable near the jet core due to the inertial character of the motion field. Following the same propagation angle from $(y, z) = (100, 1)km$, we obtain the motion fields at $(y, z) = (300, 3)$ and $(1000, 10)km$ shown in Figs. 3.3 and 3.4. The maximum responses at $(300,3)km$ occur from $\sim 4-13$ hours after the initial disturbance, suggesting a group velocity magnitude c_g from $\sim 6m/s$ to $\sim 20m/s$. At $(y, z) = (1000, 10)km$, a group velocity magnitude c_g from $\sim 6m/s$ to $13m/s$ can be observed. At $(300, 3)km$, wave periods begin near 10 hours and expand to near T_i after $\sim 1 - 2T_i$. This is also seen in the ratio of v and u, with larger meridional motions for $T < T_i$. A similar response is seen at $(1000, 10)km$ with an apparent decay observed $\sim 2-3T_i$ after the maximum response. And as Rossby (1938) said when he first introduced the geostrophic adjustment concept, the inertial oscillation implied the occurrence of the geostrophic adjustment.

A look at positions closer to the vertical and horizontal axes will help us to understand the behaviour of motions at higher and lower frequencies. Fig. 3.5, which shows the wave field at $(y, z) = (300, 10)km$, shows that higher frequency IGWs follow steeper propagation angles from the jet core. From an initial period of about 5 hours, the period increases and the amplitude decays, with the minimum

Reproduced with permission of the copyright owner. Further reproduction prohibited without permission.

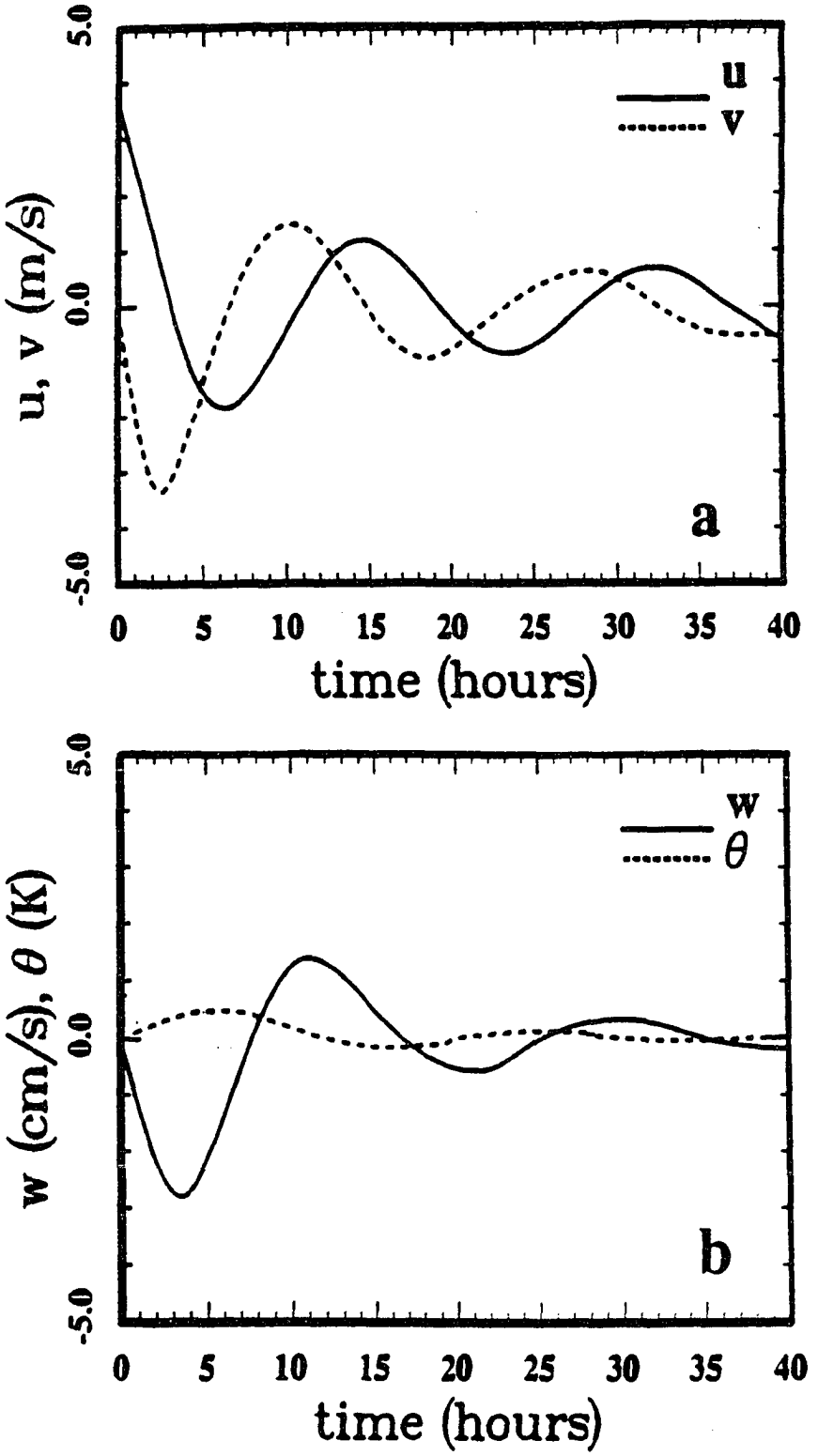

Figure 3.2 Perturbations of horizontal velocities (a), vertical velocity and temperature (b) at (y,z)=(100,1) km for the approximate Fourier integral solutions.

Reproduced with permission of the copyright owner. Further reproduction prohibited without permission.

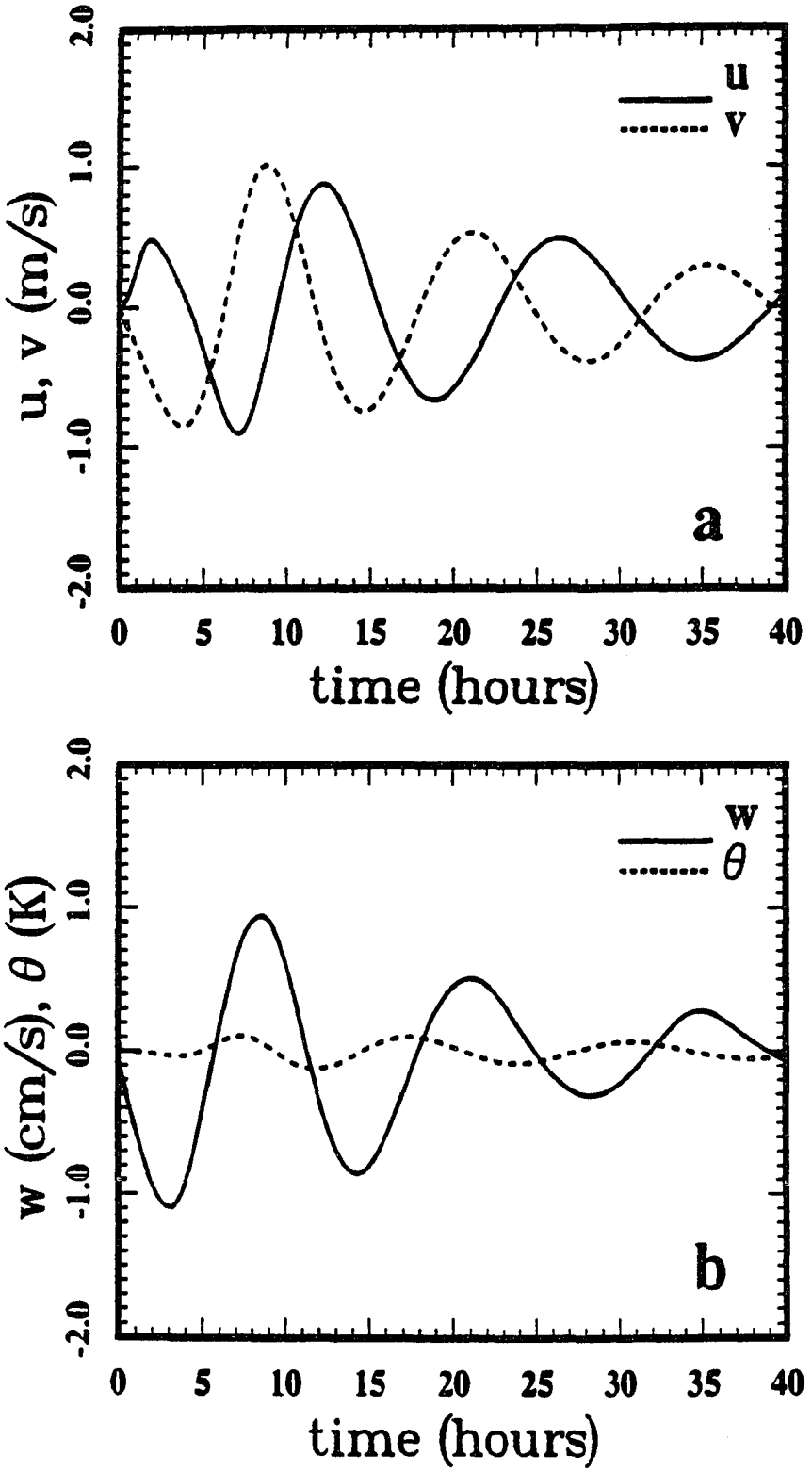

Figure 3.3 As in figure 3.2 but for (y,z)=(300,3) km.

Reproduced with permission of the copyright owner. Further reproduction prohibited without permission.

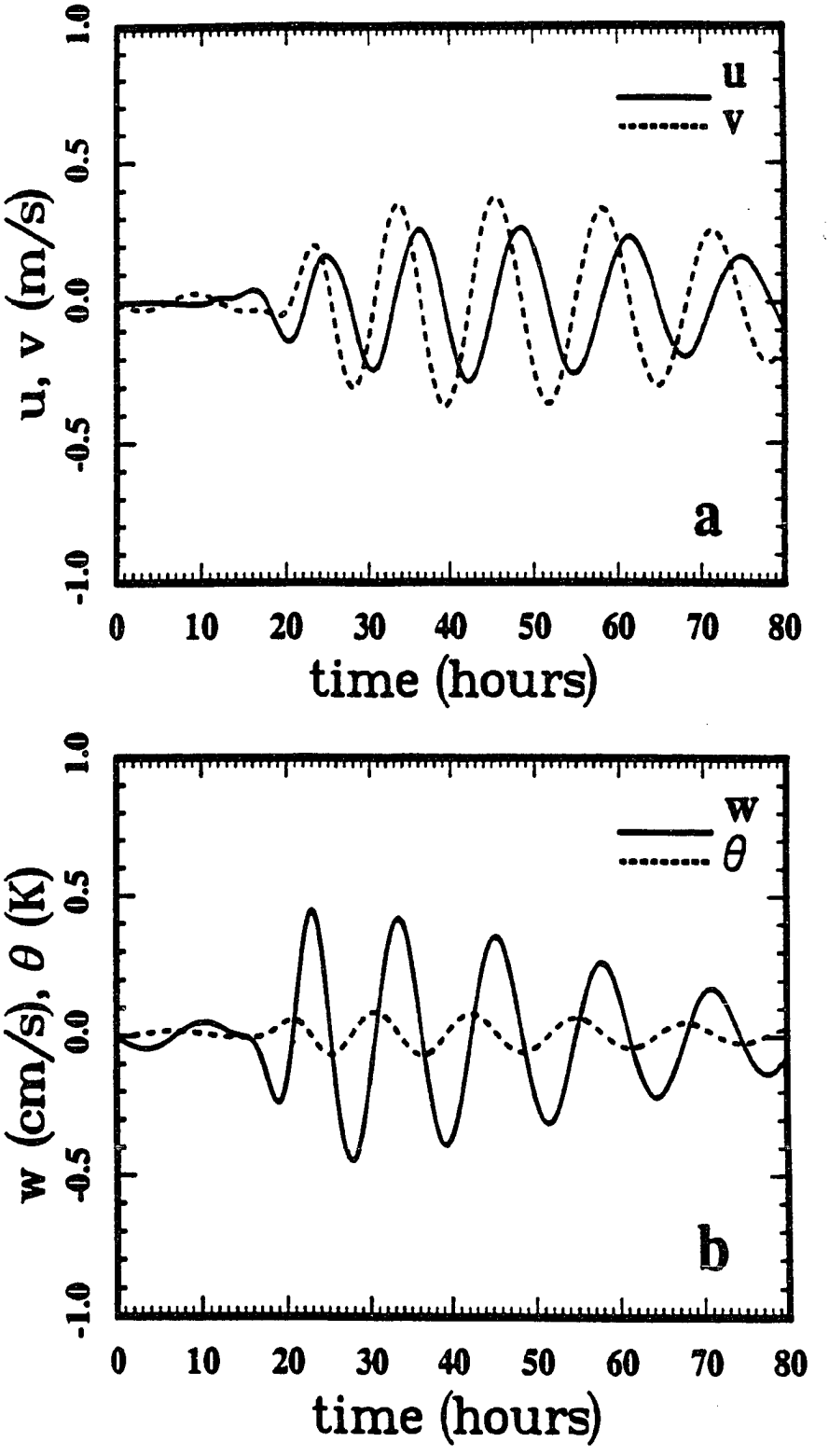

Figure 3.4 As in figure 3.2 but for (y,z)=(1000,10) km.

Reproduced with permission of the copyright owner. Further reproduction prohibited without permission.

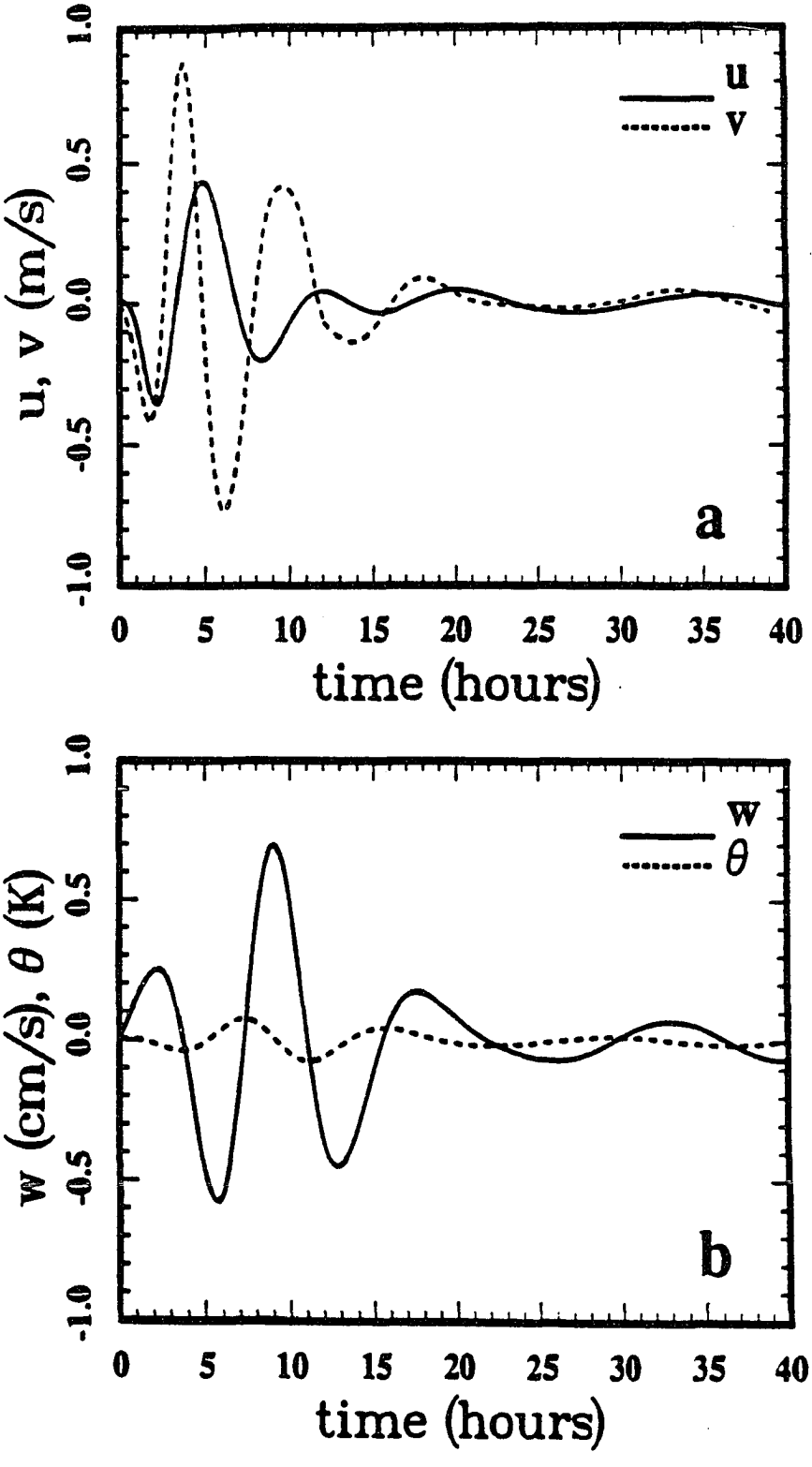

Figure 3.5 As in figure 3.2 but for (y,z)=(300,10) km.

Reproduced with permission of the copyright owner. Further reproduction prohibited without permission.

response occurring in the vertical and meridional motion fields. A positive correlation of v and w also implies outward and upward propagation of wave energy at this location. A comparison of $(y, z) = (300, 3)km$ (Fig. 3.3) and $(300, 10)km$, at the same horizontal distance from the jet core, suggests that IGW energy radiates away from the jet at a very shallow angle because of the larger amplitudes at $(300, 3)km$. A comparison of the wave fields at $(y, z) = (1000, 3)km$ (Fig. 3.6) and $(1000, 10)km$ (Fig. 3.4) likewise shows that the angle of maximum wave radiation is dictated by the initial disturbance structure, with a dominant angle $\sim tan^{-1}(1/100)$ and dominant wave periods $\sim T_i/2$ or longer. It is also noted that the lower frequency IGWs seen in Fig. 3.6 have near inertial character. Finally, we note that in this approximate solution to the initially unbalanced geostrophic adjustment problem, there is an absence of motion after the IGWs have propagated away due to the association of all initial energy with IGW motions. The more general solution is presented in section 3.6.

Time–height cross sections of the motion and thermal fields exhibit the wave structure from another point of view. Figs. 3.7 and 3.8 are for $y = 100km$ with the jet centered at $(y, z) = (0, 0)km$ as before. Larger–scale vertical motions appear at early times after the initial excitation of the horizontal motion field. A clear picture illustrated in the cross section is the progression of phase towards $z = 0$ with time increasing, consistent with the propagation of energy outward away from the unbalanced jet and the orthogonality of the group and phase velocities noted in chapter 2. The increasing wave period with time causes the vertical motion field and its companion temperature field to decay more rapidly than the horizontal motion fields (see Figs. 3.7 and 3.8). The higher altitude responses in

Reproduced with permission of the copyright owner. Further reproduction prohibited without permission.

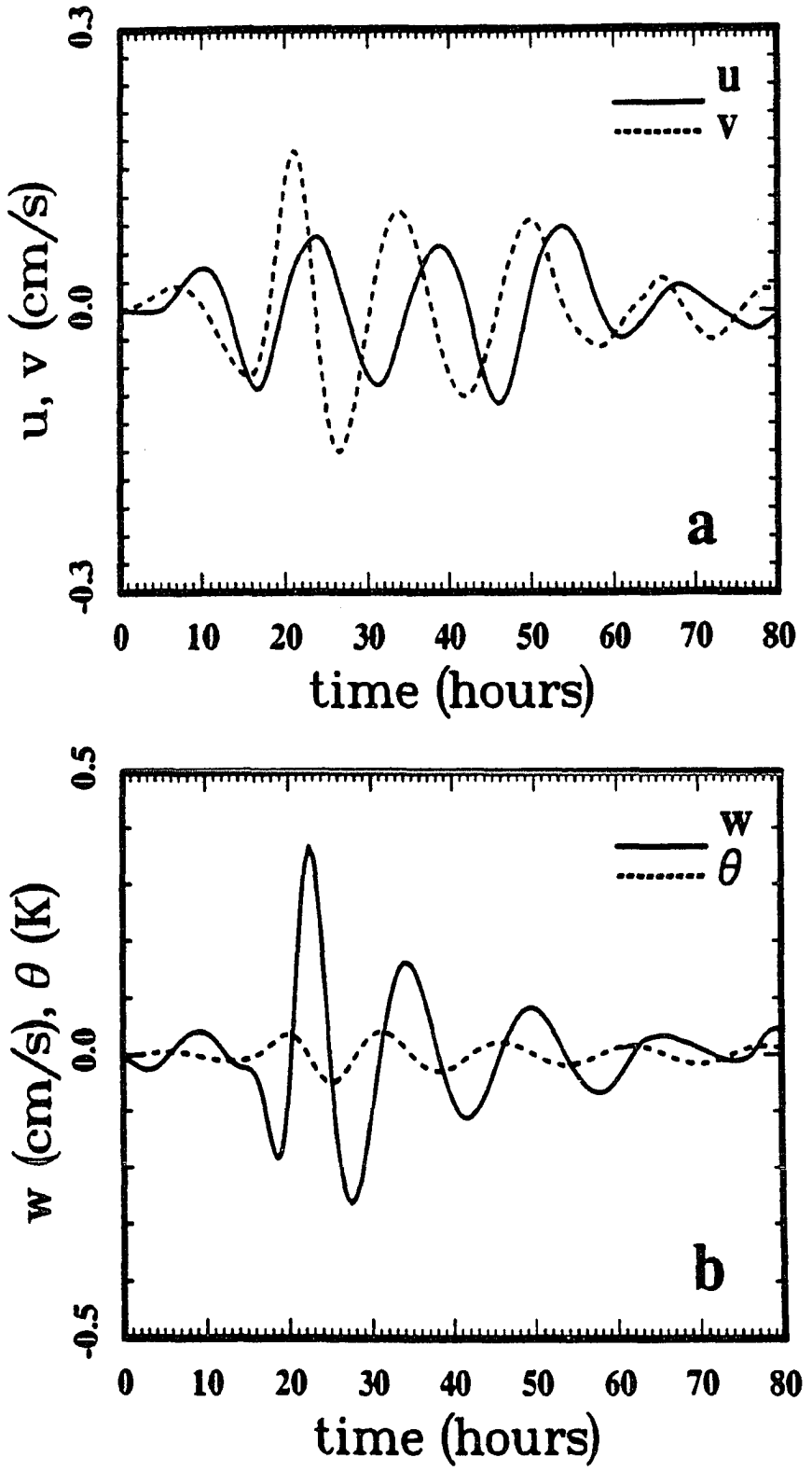

Figure 3.6 As in figure 3.2 but for (y,z)=(1000,3) km.

Reproduced with permission of the copyright owner. Further reproduction prohibited without permission.

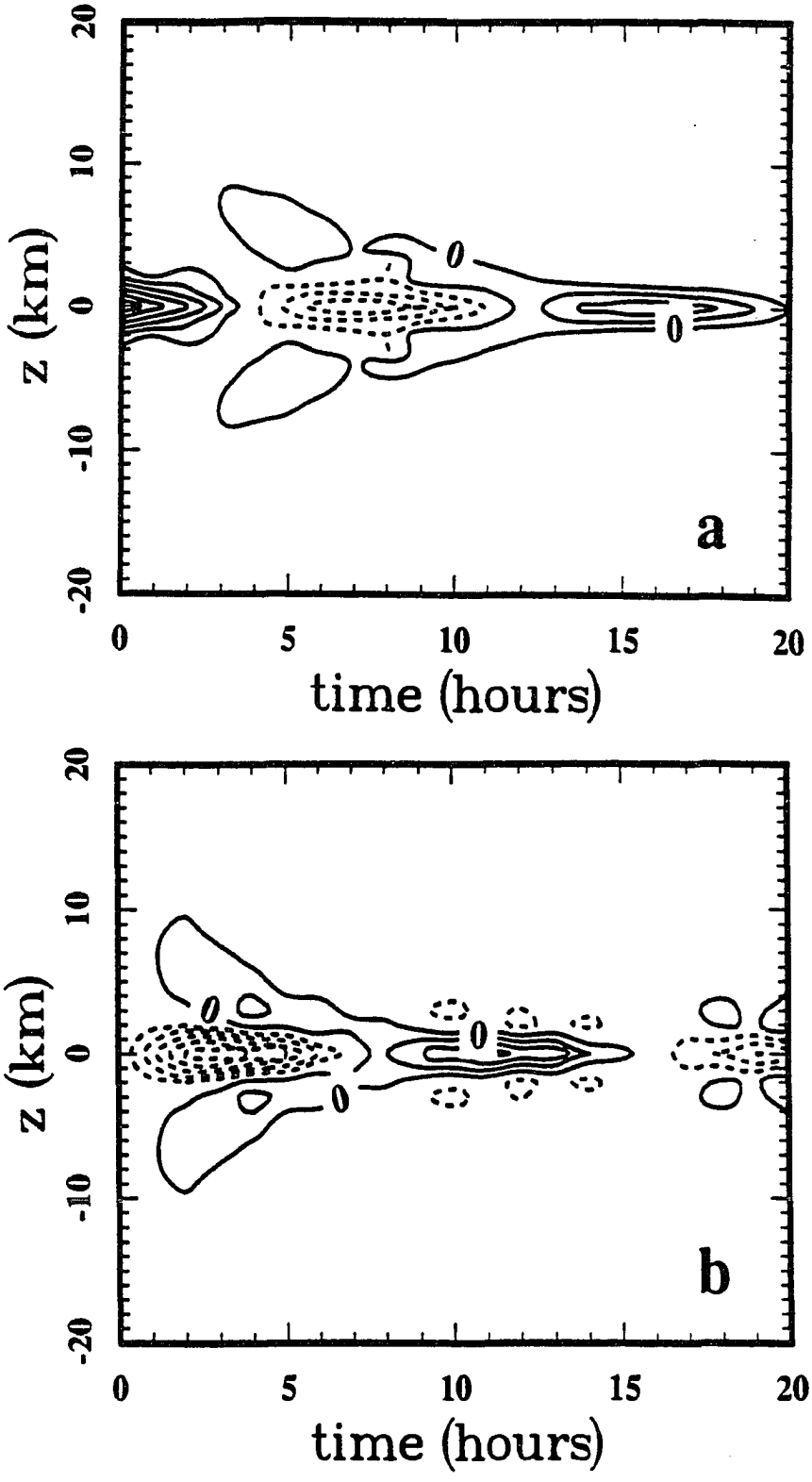

Figure 3.7 Time–height cross section of zonal (a, Δu=1.0m/s) and meridional (b, Δv=1.0m/s) velocity fluctuations at y=100 km for approximate Fourier integral solutions. Solid (dashed) contours indicate positive (negative) values.

Reproduced with permission of the copyright owner. Further reproduction prohibited without permission.

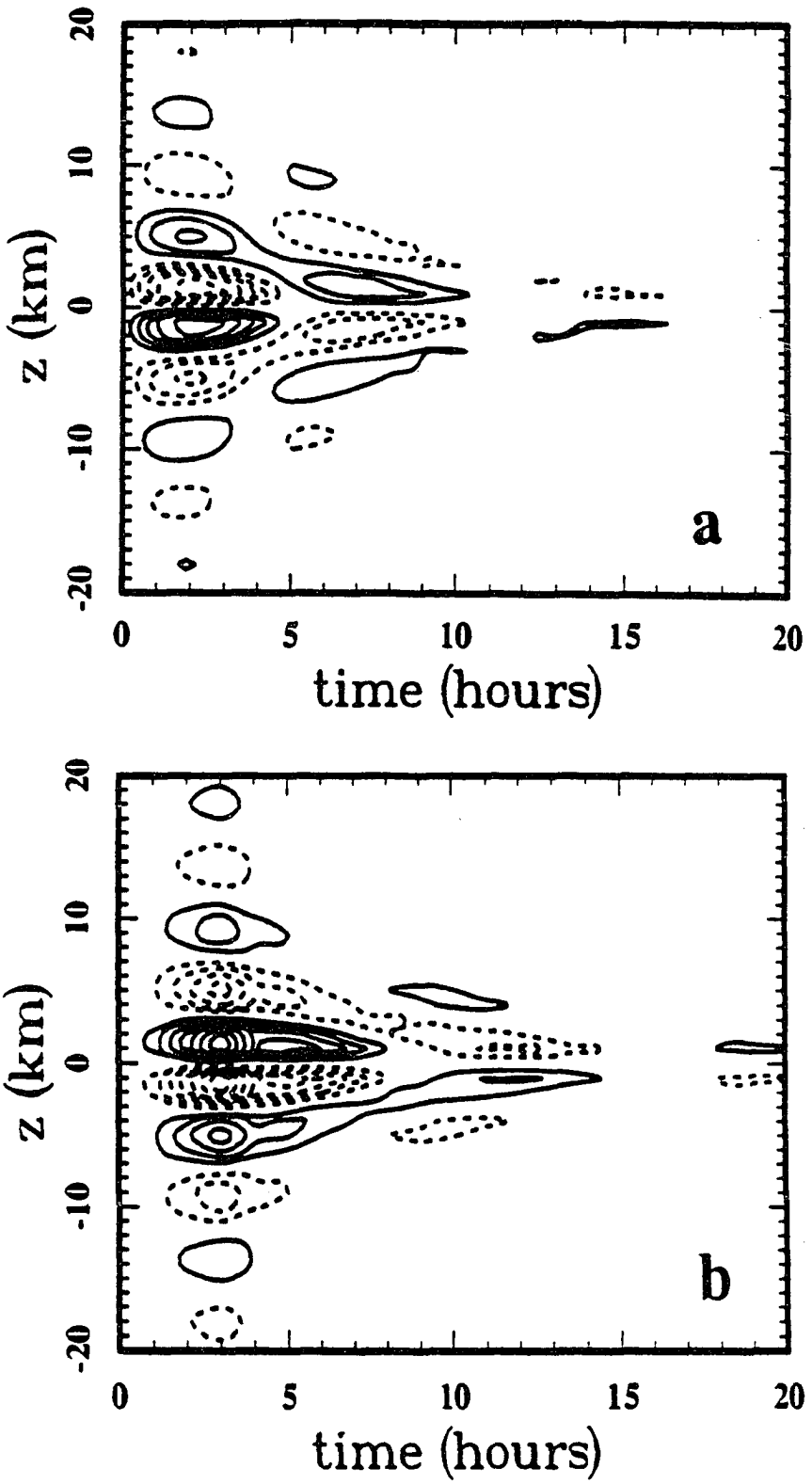

Figure 3.8 As in figure 3.7 but for vertical velocity (a, Δw=0.5cm/s) and temperature fluctuations (b, $\Delta\theta$=0.08K).

Reproduced with permission of the copyright owner. Further reproduction prohibited without permission.

the w and θ fields at early times also shows the rapid propagation ability of the higher–frequency waves implied by the dispersion relation. The dominant vertical wavelengths range from $\sim 6 - 8km$ and are seen clearly at this position and at greater distances throughout the evolution.

Figs. 3.9 and 3.10 show the cross sections at $y = 300km$. The vertical distribution of wave energy is now larger because of IGW radiation at preferred angles as noted in the time series discussed above. Larger–scale vertical motions again are seen at early times.

Greater distances exhibit the wave behavior even more clearly. At $y = 1000km$ (Figs. 3.11 and 3.12), the fastest IGW motions appear after ~ 20 hours, with the maximum response occurring somewhat later far above and below the jet axis. Since the IGWs propagate away from the jet, energy has been transported upward and downward as indicated in the figures. No energy has been transported by the motion field in the horizontal direction, emphasizing the special role of internal gravity waves in the baroclinic geostrophic adjustment process. Note that energy that appear in the horizontal motions at $z = 0$ at early times in Fig. 3.11 is not due to horizontal energy transport but due instead to the initial unbalanced structure above and below $z = 0$. Likewise, w in Fig. 3.12 results from the v field through the continuity equation, while w leads θ (Fig. 3.12) because motions are assumed to be adiabatic.

Reproduced with permission of the copyright owner. Further reproduction prohibited without permission.

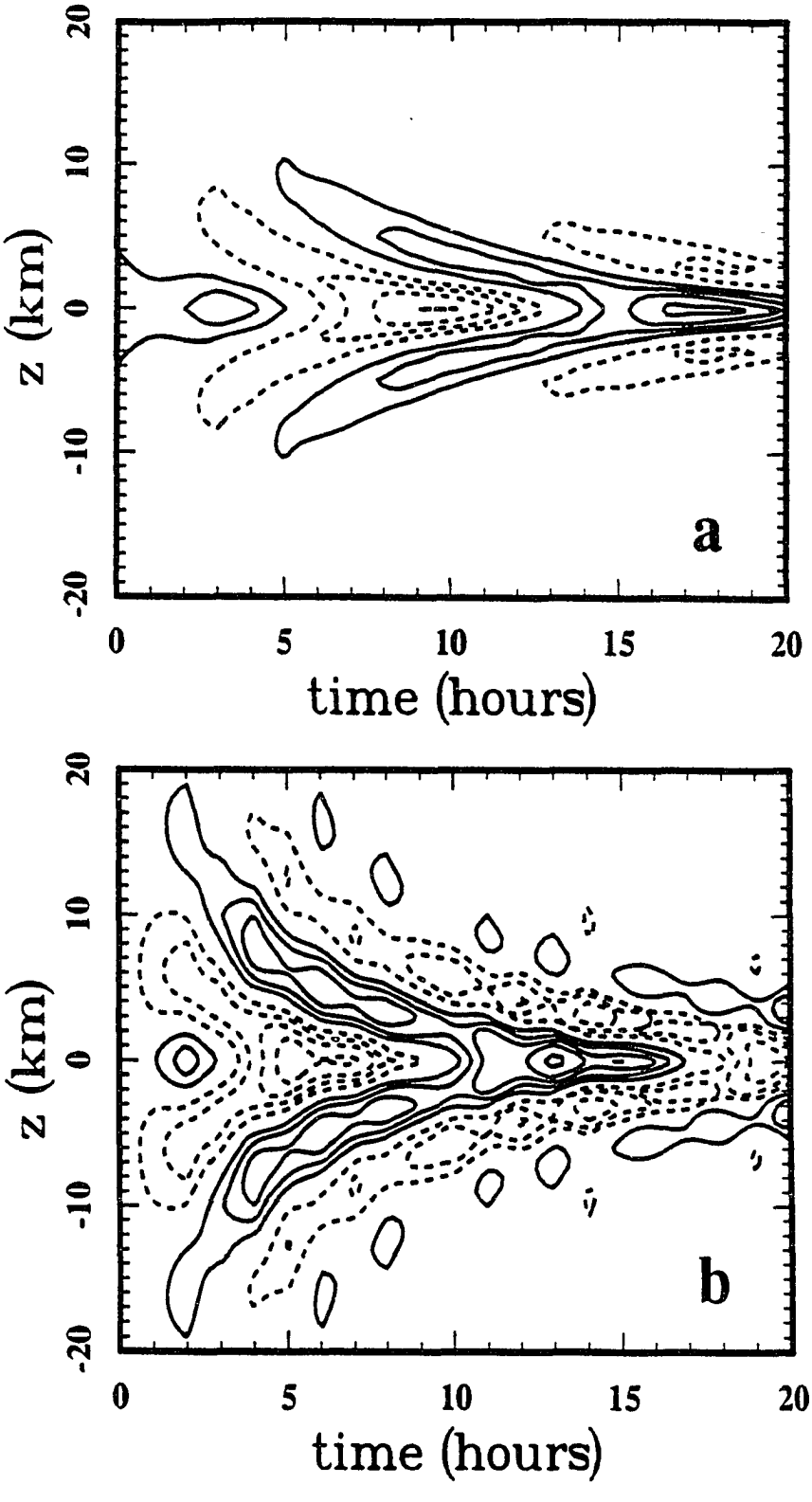

Figure 3.9 As in figure 3.7 but for y=300 km. (a), Δu=0.4m/s; (b), Δv=0.4m/s.

Reproduced with permission of the copyright owner. Further reproduction prohibited without permission.

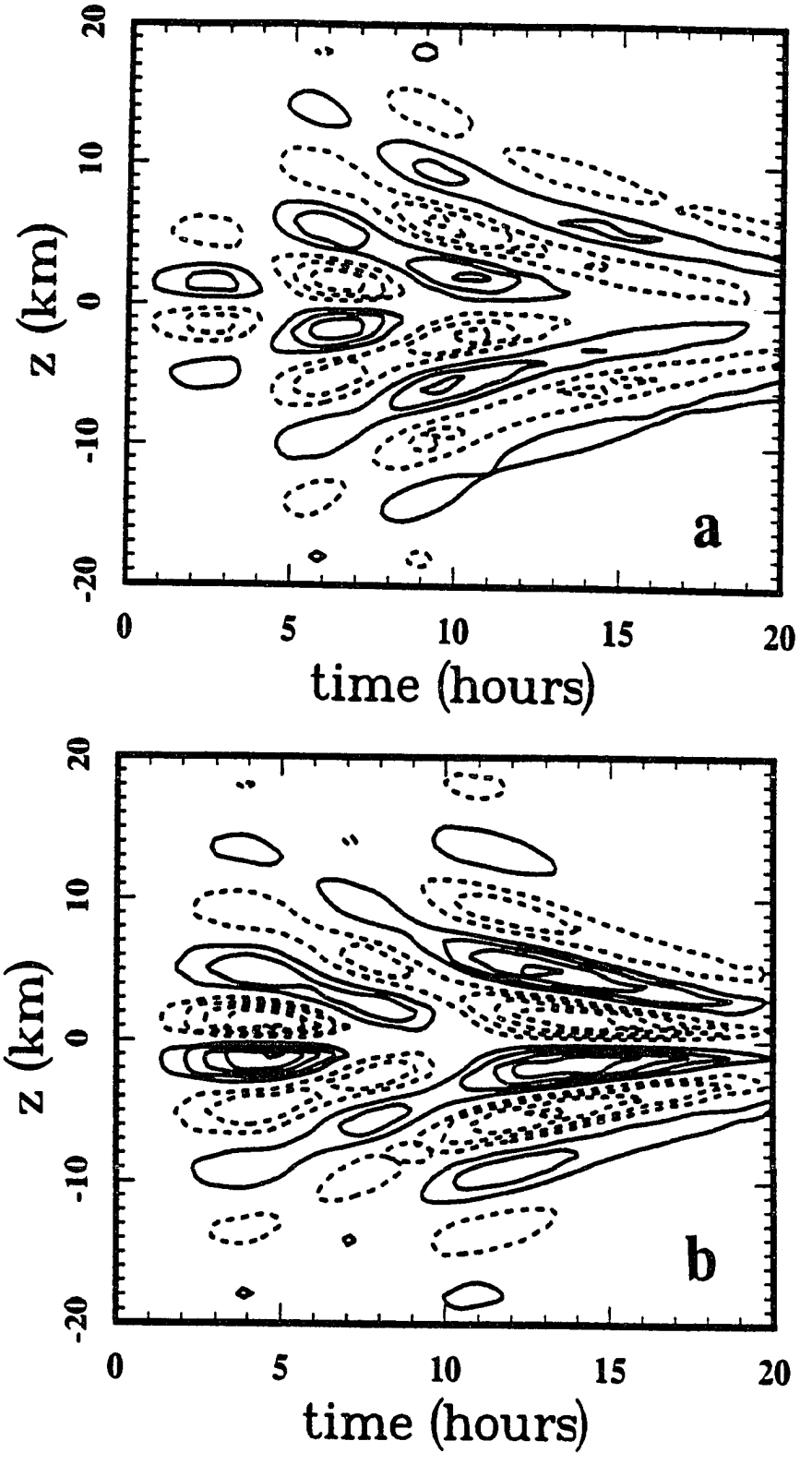

Figure 3.10 As in figure 3.8 but for y=300 km. (a), Δw=0.3cm/s; (b), $\Delta\theta$=0.04K.

Reproduced with permission of the copyright owner. Further reproduction prohibited without permission.

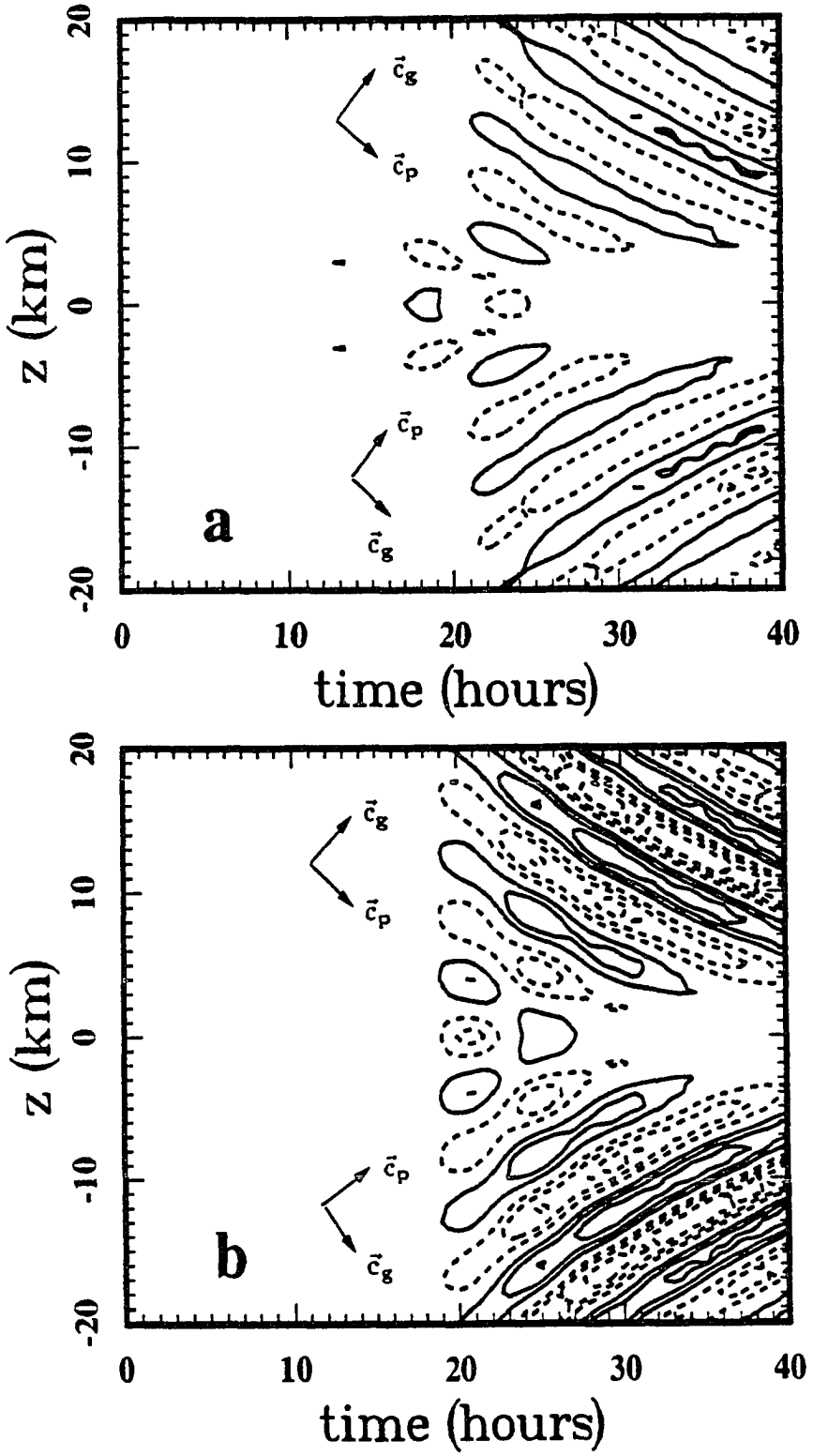

Figure 3.11 As in figure 3.7 but for y=1000 km. $\vec{c}_p$ and $\vec{c}_g$ are phase and group velocities. (a), Δu=0.1m/s; (b), Δv=0.1m/s.

Reproduced with permission of the copyright owner. Further reproduction prohibited without permission.

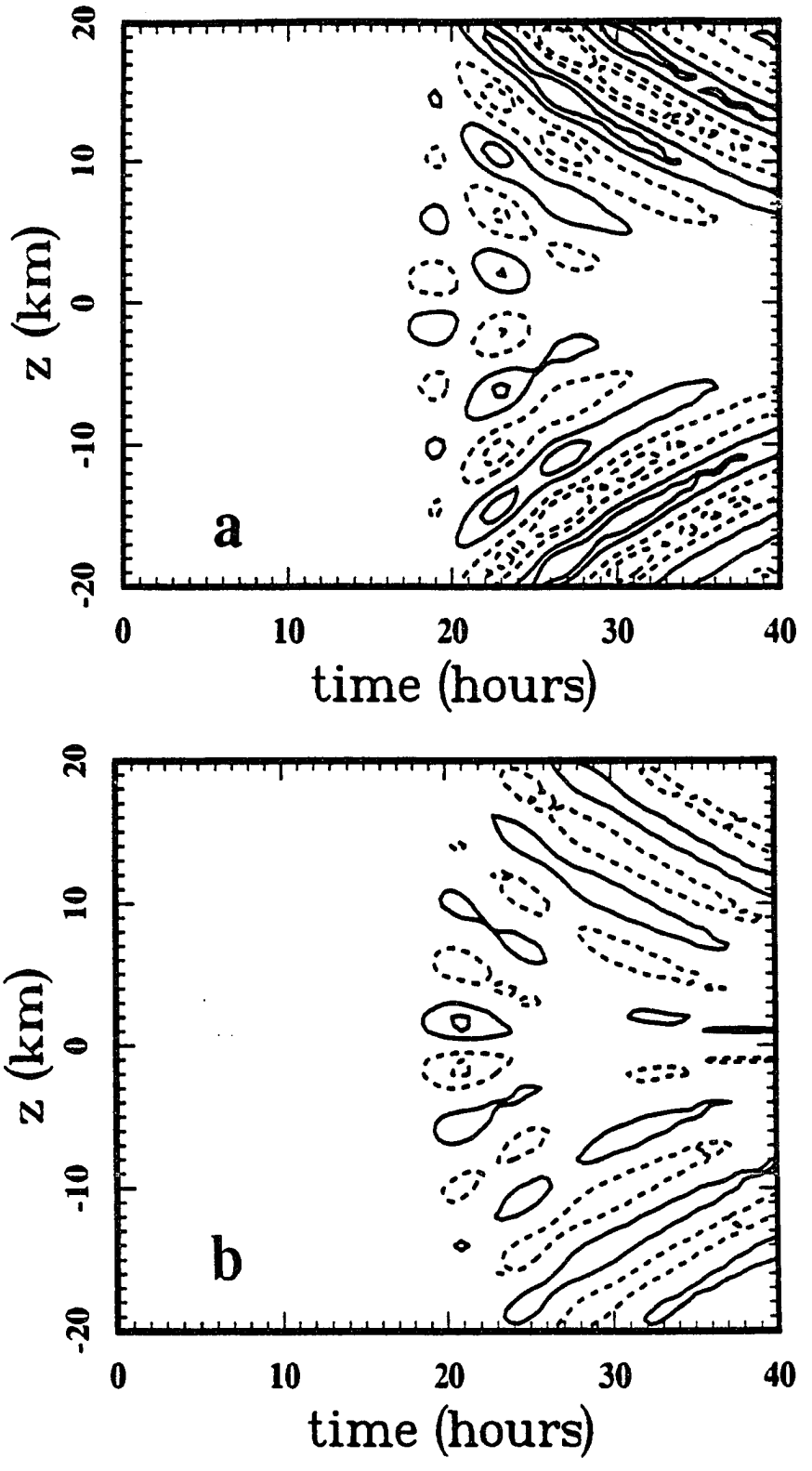

Figure 3.12 As in figure 3.8 but for y=1000 km. (a), Δw=0.2m/s; (b), $\Delta\theta$=0.05K.

Reproduced with permission of the copyright owner. Further reproduction prohibited without permission.

3.5 The Hydrostatic Approximation

An approximation generally valid at large horizontal scales in the atmosphere is that the vertical distribution of pressure is due only to the weight of the fluid column above. This implies, from the vertical momentum equation, eq. (A.3), a vertical fluid acceleration much less than that due to gravity, $dw/dt \ll g$ or , in terms of the vertical stratification, $\omega^2 \ll N^2$. This implies as well approximately horizontal motions ($w^2 \ll u^2$), nearly horizontal phase slopes ($k^2 \ll m^2$), and a

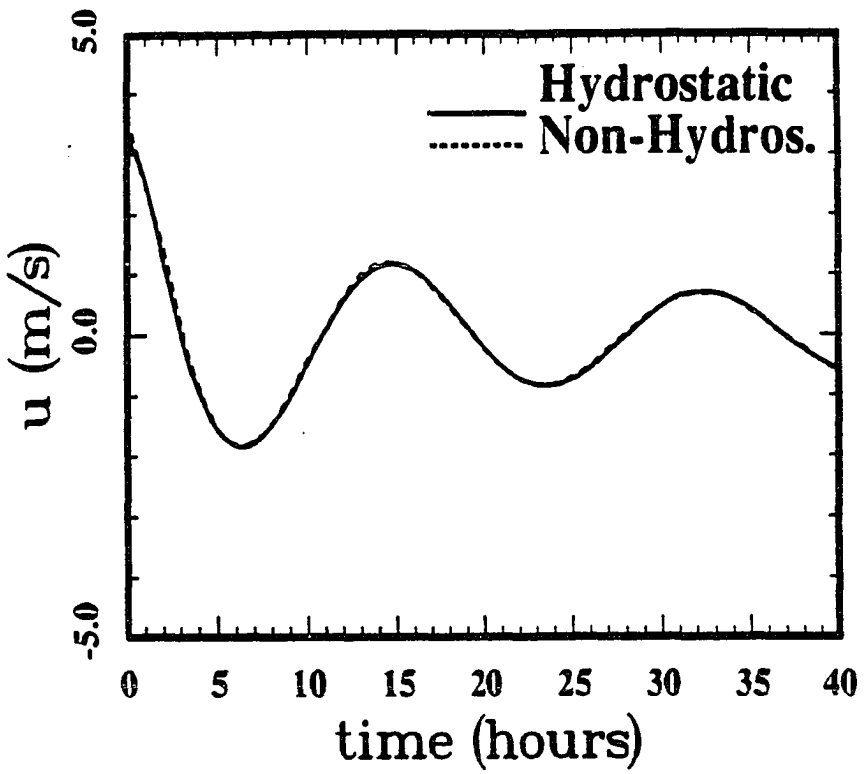

Figure 3.13 A comparison between hydrostatic and nonhydrostatic approximations in zonal velocity fluctuations at (y,z)=(100,1) km. This is the approximate Fourier integral solutions.

dispersion relation given by

$$\omega_h^2 = f^2 + \frac{k^2 + l^2}{m^2} N^2 \tag{3.19}$$

Reproduced with permission of the copyright owner. Further reproduction prohibited without permission.

where ω_h denotes gravity wave frequency under the hydrostatic approximation.

Numerical simulations including the hydrostatic approximations were conducted to compare with the nonhydrostatic results. In this case, almost identical results are achieved and Fig. 3.13 exhibits one of them. The hydrostatic result is consistent with our expectations because of the structure of the initial disturbance, causing the induced waves to have much larger horizonal wavelengths than in the vertical. The accuracy of the hydrostatic approximation allowed us to apply it when the 3–D jet adjustment process is investigated.

3.6 Adjustment of Initial Unbalance II: Full Fourier Integral Solutions

One further step in understanding the geostrophic adjustment of an infinite unbalanced Gaussian jet stream is to include not only the radiation of unbalanced momentum away as IGWs but also the resulting adjustments of the mean state needed to conserve potential vorticity. The interpretation of this physical meaning moves us from a homogeneous initial–value problem (denoted as approximate solution in section 3.4) to a nonhomogeneous treatment (denoted as the full solution) mathematically. In this way, energy partition between the IGWs and the mean state can be examined. In this 2–D investigation, since it is less computationally tedious to maintain the nonhydrostatic term and provides the same dynamic approximations as the initial–value treatment discussed above, $\varepsilon_h = 1$ has been taken.

Reproduced with permission of the copyright owner. Further reproduction prohibited without permission.

3.6.1 Theoretical Solutions

Mathematical description of the nonhomogeneous problem can be quoted from eqs. (3.1)–(3.5) with $\eta = 1$ and u, v, w, θ, p, u_t, v_t, w_t, θ_t and p_t all zero initially. The Dirac delta function in time means the balanced field has only been forced impulsively. It is possible, though, to construct another function in the time domain depending on the physical problem, a possibility yielding one more integral level in the final expressions. To generate the operators for each field variable, we take the divergence and curl of the horizontal momentum equations and do some algebra as described in appendix A. This gives (A.20 with $\partial/\partial x = \varepsilon_c = 0, \eta = \varepsilon_h = 1$)

$$\begin{pmatrix} L_1 u \\ L_2 v \\ L_2 w \\ L_1 \theta \end{pmatrix} = \begin{pmatrix} \overbrace{(M_{yy} + M_{zz})\delta''(t)}^{Part\ 1} & \overbrace{+N^2 M_{yy}\delta(t)}^{Part\ 2} \\ -fM_{zz}\delta(t) & \\ fM_{yz}\delta(t) & \\ -\frac{f\bar{\theta}N^2}{g} M_{yz}\delta(t) & \end{pmatrix}, \tag{3.20}$$

where

$$L_1 = \frac{\partial}{\partial t}\left(\frac{\partial^2}{\partial t^2}\Delta_2^* + N^2\frac{\partial^2}{\partial y^2} + f^2\frac{\partial^2}{\partial z^2}\right), \tag{3.21}$$

and

$$L_2 = \frac{\partial^2}{\partial t^2}\Delta_2^* + N^2\frac{\partial^2}{\partial y^2} + f^2\frac{\partial^2}{\partial z^2}. \tag{3.22}$$

Here $\Delta_2^* = \partial^2/\partial y^2 + \partial^2/\partial z^2$. The rest of the notation is defined in Appendix A.

We use the Fourier transform pairs given by eqs. (3.9) and (3.10) and adopt the notation from previous sections. Applying eq. (3.9) to eq. (3.20) yields

Reproduced with permission of the copyright owner. Further reproduction prohibited without permission.

$$L\begin{pmatrix}\tilde{u}\\ \tilde{v}\\ \tilde{w}\\ \tilde{\theta}\end{pmatrix}=\frac{1}{\kappa^2}\begin{pmatrix}-(\tilde{M}_{yy}+\tilde{M}_{zz})\delta'(t) & -N^2\tilde{M}_{yy}\\ f\tilde{M}_{zz}\delta(t) & \\ -f\tilde{M}_{yz}\delta(t) & \\ \frac{f\bar{\theta}N^2}{g}\tilde{M}_{yz} & \end{pmatrix}, \tag{3.23}$$

where

$$L=\frac{d^2}{dt^2}+\omega^2. \tag{3.24}$$

Eq. (3.23) contains four linear ordinary differential equations and can be solved straightforwardly. The solutions are

$$\begin{pmatrix}\tilde{u}\\ \tilde{v}\\ \tilde{w}\\ \tilde{\theta}\end{pmatrix}=\frac{1}{\kappa^2}\begin{pmatrix}-(\tilde{M}_{yy}+\tilde{M}_{zz})cos(\omega t) & -\frac{N^2}{\omega^2}\tilde{M}_{yy}[1-cos(\omega t)]\\ \frac{f}{\omega}\tilde{M}_{zz}sin(\omega t) & \\ -\frac{f}{\omega}\tilde{M}_{yz}sin(\omega t) & \\ \frac{f\bar{\theta}N^2}{g\omega^2}\tilde{M}_{yz}[1-cos(\omega t)] & \end{pmatrix}, \tag{3.25}$$

where

$$\begin{pmatrix}\tilde{M}_{yy}\\ \tilde{M}_{zz}\\ \tilde{M}_{yz}\end{pmatrix}=-\frac{u_*\sigma_y\sigma_z}{2\pi}exp[-(\frac{\sigma_y^2}{2}l^2+\frac{\sigma_z^2}{2}m^2)]\begin{pmatrix}l^2\\ m^2\\ lm\end{pmatrix}. \tag{3.26}$$

Transforming back to the physical domain results in explicit expressions for all field variables. For the convenience of discussion, all solutions have been displayed in two parts using superscripts (1) and (2) which correspond to the two nonhomogeneous terms given in eq. (3.20). Since v, w and θ have only one part, their upper indexes have been eliminated. The final mathematical solutions for u can be written as

$$\begin{aligned}u^{(1)}(y,z,t) &= \frac{2u_*\sigma_y\sigma_z}{\pi}\int_{0+}^{+\infty}\int_{0+}^{+\infty}exp[-(\frac{\sigma_y^2l^2}{2}+\frac{\sigma_z^2m^2}{2})]\\ &\quad\cdot cos(ly)cos(mz)cos(\sqrt{\frac{N^2l^2+f^2m^2}{l^2+m^2}}t)dldm,\end{aligned} \tag{3.27}$$

and

$$u^{(2)}(y,z,t) = \frac{2N^2u_*\sigma_y\sigma_z}{\pi}\int_{0+}^{+\infty}\int_{0+}^{+\infty}\frac{l^2}{N^2l^2+f^2m^2}exp[-(\frac{\sigma_y^2l^2}{2}+\frac{\sigma_z^2m^2}{2})]$$

Reproduced with permission of the copyright owner. Further reproduction prohibited without permission.

$$\cdot cos(ly)cos(mz)[1-cos(\sqrt{\frac{N^2l^2+f^2m^2}{l^2+m^2}}t)]dldm. \tag{3.28}$$

The complete solution for u is then

$$u = u^{(1)} + u^{(2)}, \tag{3.29}$$

with the mean state given from $u^{(2)}$ by

$$\begin{aligned}\bar{u}(y,z) &= \frac{2N^2u_*\sigma_y\sigma_z}{\pi}\int_{0+}^{+\infty}\int_{0+}^{+\infty}\frac{l^2}{N^2l^2+f^2m^2} \\ &\cdot exp[-(\frac{\sigma_y^2l^2}{2}+\frac{\sigma_z^2m^2}{2})]cos(ly)cos(mz)dldm.\end{aligned} \tag{3.30}$$

Similarly, v, w and θ are

$$\begin{aligned}v(y,z,t) &= -\frac{2fu_*\sigma_y\sigma_z}{\pi}\int_{0+}^{+\infty}\int_{0+}^{+\infty}\frac{m^2}{l^2+m^2}\sqrt{\frac{l^2+m^2}{N^2l^2+f^2m^2}}exp[-(\frac{\sigma_y^2l^2}{2}+\frac{\sigma_z^2m^2}{2})] \\ &\cdot cos(ly)cos(mz)sin(\sqrt{\frac{N^2l^2+f^2m^2}{l^2+m^2}}t)dldm,\end{aligned} \tag{3.31}$$

$$\begin{aligned}w(y,z,t) &= -\frac{2fu_*\sigma_y\sigma_z}{\pi}\int_{0+}^{+\infty}\int_{0+}^{+\infty}\frac{lm}{l^2+m^2}\sqrt{\frac{l^2+m^2}{N^2l^2+f^2m^2}}exp[-(\frac{\sigma_y^2l^2}{2}+\frac{\sigma_z^2m^2}{2})] \\ &\cdot sin(ly)sin(mz)sin(\sqrt{\frac{N^2l^2+f^2m^2}{l^2+m^2}}t)dldm,\end{aligned} \tag{3.32}$$

and

$$\begin{aligned}\theta(y,z,t) &= \frac{2\bar{\theta}N^2fu_*\sigma_y\sigma_z}{\pi g}\int_{0+}^{+\infty}\int_{0+}^{+\infty}\frac{lm}{N^2l^2+f^2m^2}exp[-(\frac{\sigma_y^2l^2}{2}+\frac{\sigma_z^2m^2}{2})] \\ &\cdot sin(ly)sin(mz)[1-cos(\sqrt{\frac{N^2l^2+f^2m^2}{l^2+m^2}}t)]dldm.\end{aligned} \tag{3.33}$$

3.6.2 Wave Field and Mean State

Let us now compare the approximate results of eqs. (3.15)-(3.18) with the full solutions expressed by eqs. (3.27), (3.28) and (3.31)-(3.33). It is found that

Reproduced with permission of the copyright owner. Further reproduction prohibited without permission.

part 1 of the full solution, $u^{(1)}$, is identical to the approximate results. The extra term, $u^{(2)}$, in the nonhomogeneous treatment represents a balanced zonal state (eq. 3.30) after the adjustment and a correction term to the approximate (homogeneous) treatment of the problem. The deviations of v, w and θ between the approximate and full solutions are due to the differences in the integration of a factor $(f/\omega)(m^2/\kappa^2)$. They would be identical if this factor were unity. As showed in section 3.5 of this chapter, an almost perfect agreement of hydrostatic and non-hydrostatic approximations indicates the flat wave phase, *i.e.* $m^2/\kappa^2 \sim 1$. Also it can be seen in section 3.4 that IGW frequencies elongate to near T_i soon after the initial disturbance. Therefore, the major differences between the approximate and full solutions of the 2–D initial unbalanced geostrophic adjustment is a balanced state in the full solution. Although the wavefields have been defined well by the detailed computations in section 3.4, it is the intent here to compare the wave fields following adjustment of the mean state. Figs. 3.14 and 3.15 exhibit the full consideration results at $(y, z) = (100, 1)km$ and $(y, z) = (300, 3)km$. At the position $(100, 1)km$ which is very close to the jet core, we can see (comparing to Fig. 3.2) that the w and θ fields are almost indistinguishable. The smaller amplitudes at $(300, 3)km$ (Fig. 3.15) at early times in the full Fourier integral solutions seems to suggest that the balanced mean state is achieved fairly quickly (less than one T_i) through redistribution of the initial potential vorticity.

A comparison of the approximate and full solutions at $(y, z) = (300, 3)km$ revealing a large deviation restricted to early times is displayed in Fig. 3.16. Beyond this initial response, however, the IGW field achieves a comparable structure.

The mean fields before and after adjustment are compared in Fig. 3.17. At

Reproduced with permission of the copyright owner. Further reproduction prohibited without permission.

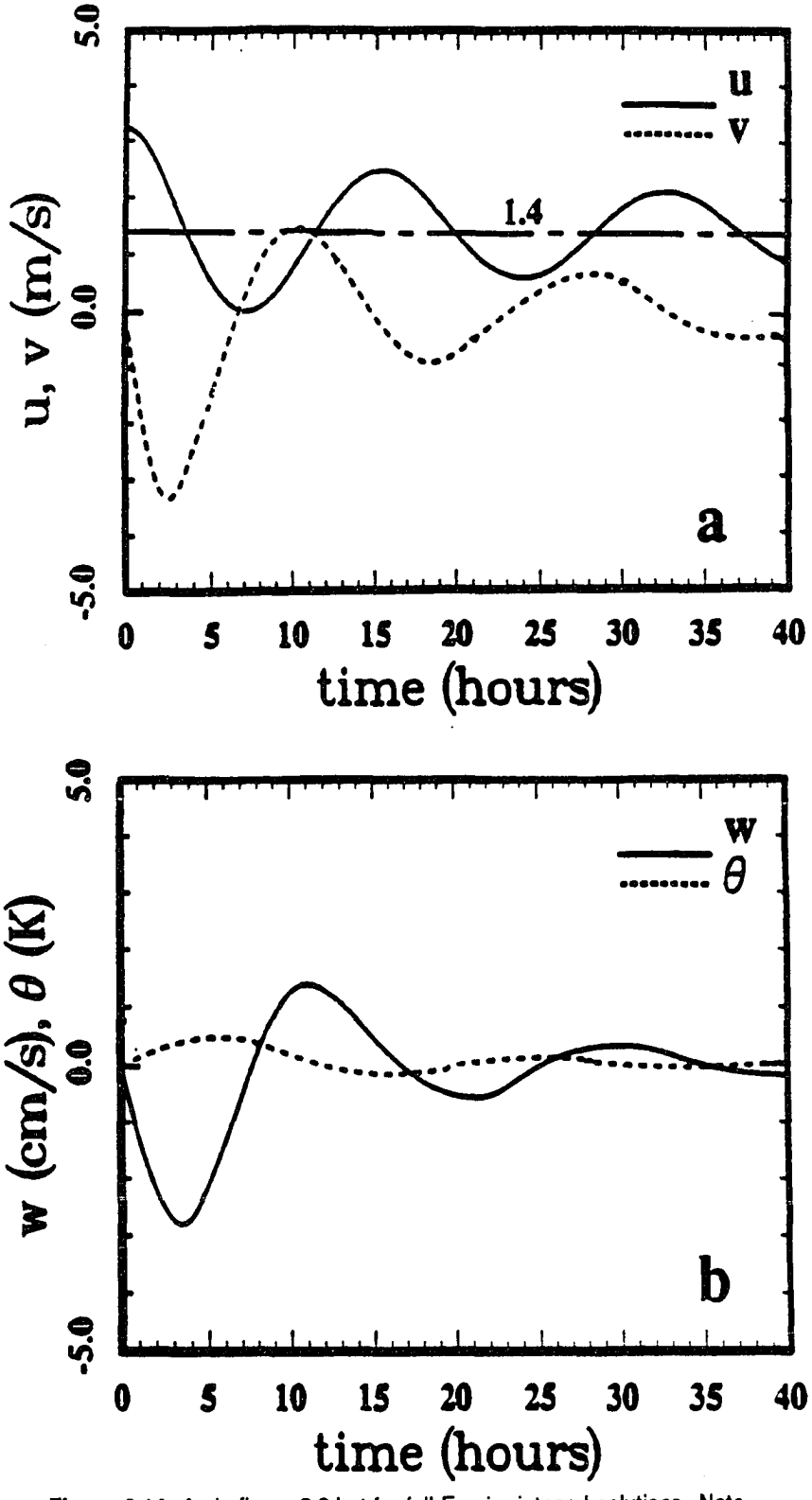

Figure 3.14 As in figure 3.2 but for full Fourier integral solutions. Note the induced mean state in (a).

Reproduced with permission of the copyright owner. Further reproduction prohibited without permission.

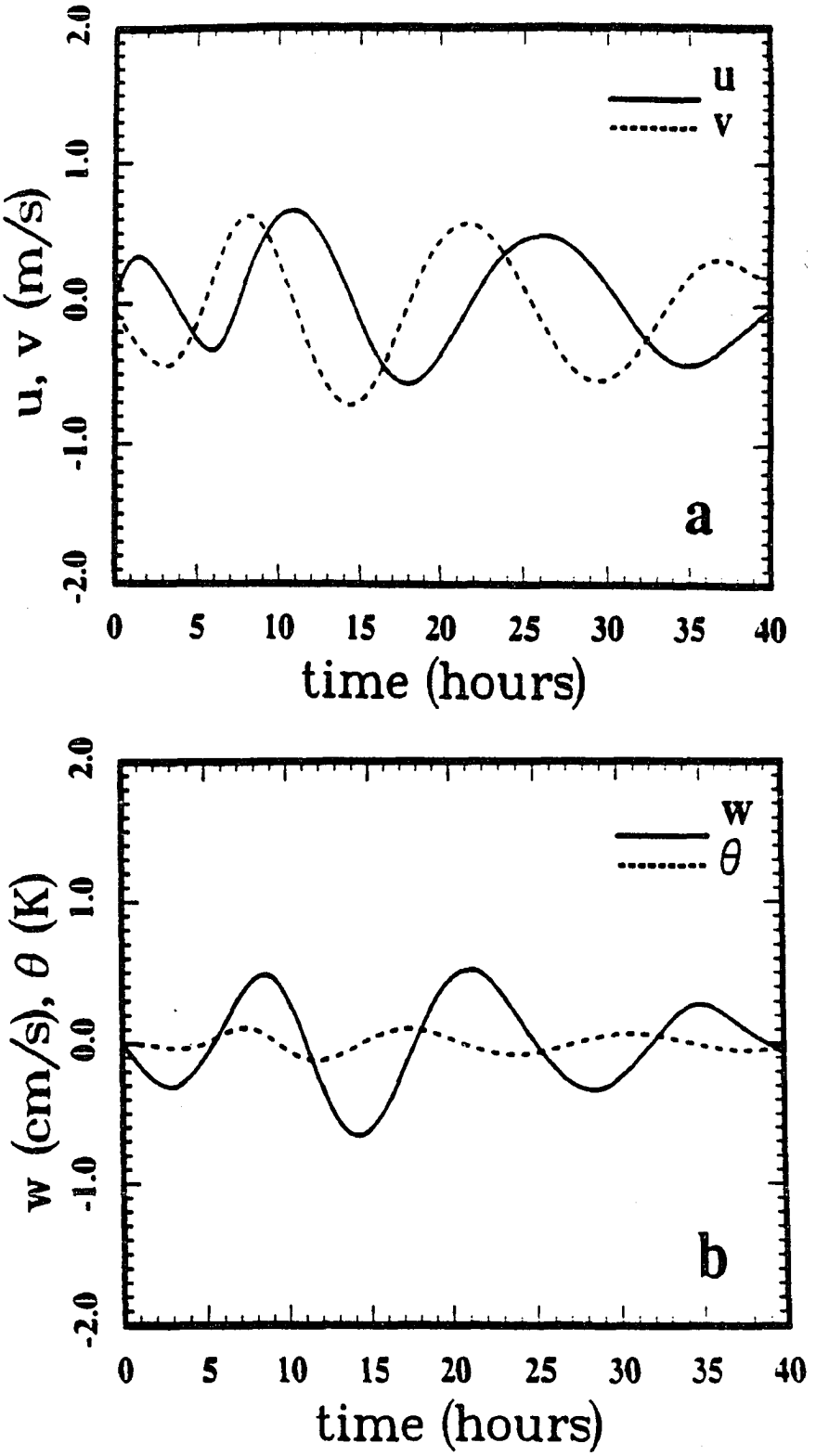

Figure 3.15 As in figure 3.14 but for (y,z)=(300,3) km. The mean in (a) is tiny (without plotting).

Reproduced with permission of the copyright owner. Further reproduction prohibited without permission.

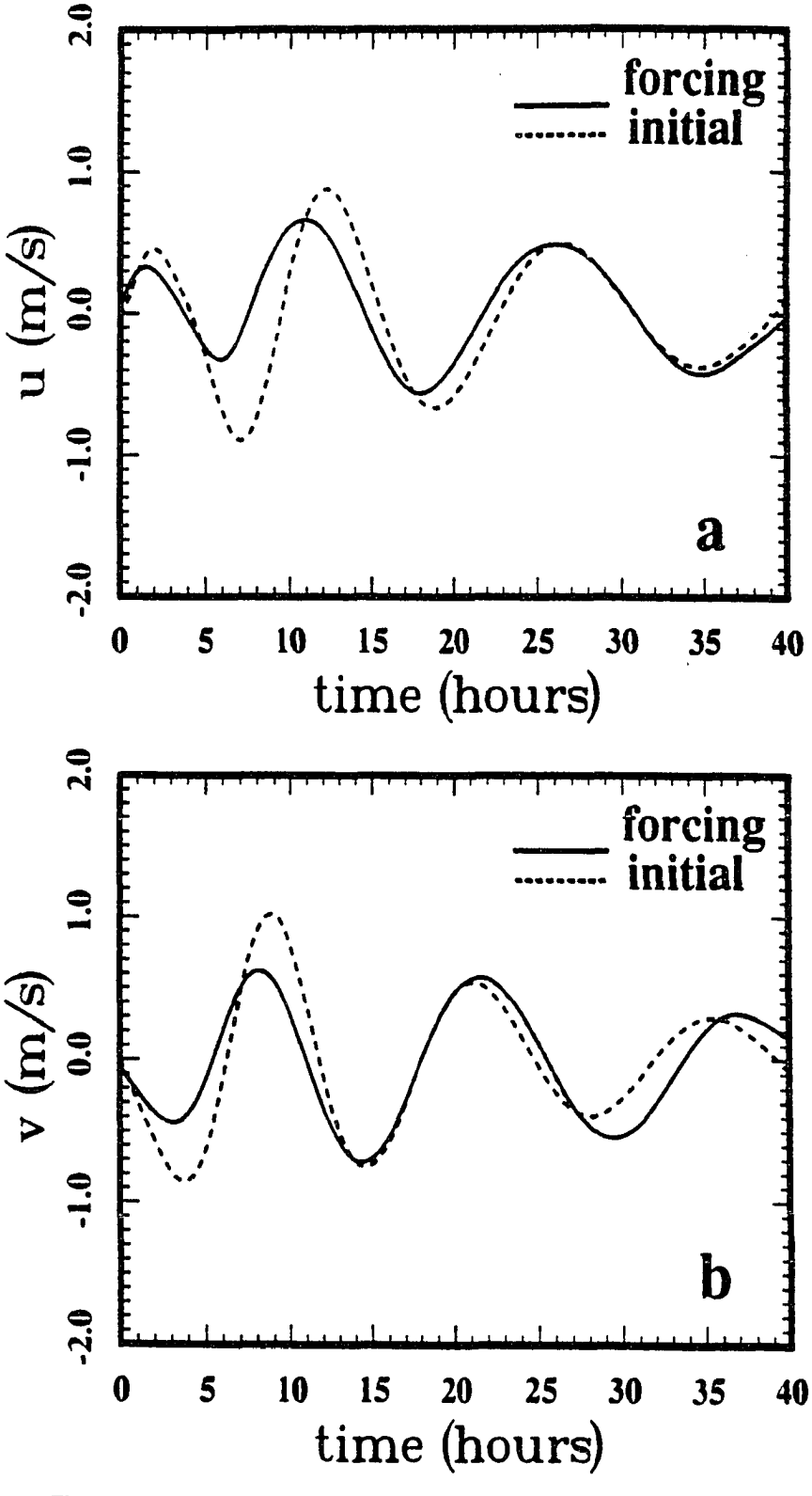

Figure 3.16 Comparisons of horizontal velocity fluctuations between approximate and full Fourier integral solutions at (y,z)=(300,3) km.

Reproduced with permission of the copyright owner. Further reproduction prohibited without permission.

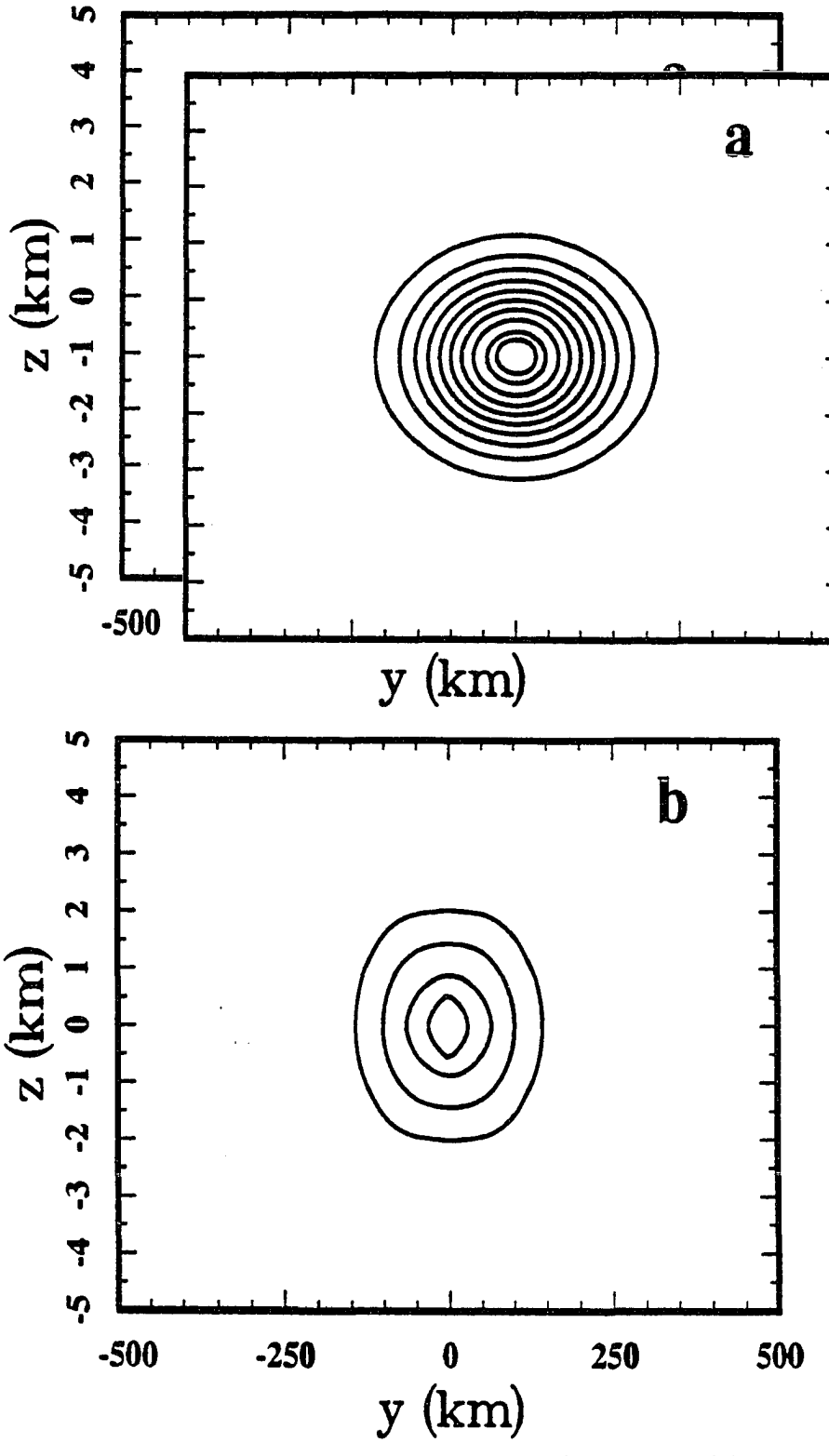

Figure 3.17 Initially unbalanced Gaussian jet (a, Δu=1.0m/s) and the induced mean state after the adjustment (b, $\Delta \bar{u}$ =1.0m/s) for the 2–D problem.

Reproduced with permission of the copyright owner. Further reproduction prohibited without permission.

the jet core there is $\sim 40\%$ of the magnitude of the initial perturbation remaining, implying about 80% of the energy has been carried away by IGWs. This has also been confirmed by the numerical summation through the entire mean field. The slimmer shape of the balanced state after the adjustment is caused by rotational influences on the transient solution.

3.7 Adjustment of Initial Unbalance III: Green's Function Solutions

Employing Green's function techniques to solve point source problems is familiar in many fields of physics. In principle, it can also be extended to deal with general sources. As an alternative tool to handle the nonhomogeneous equation, its purpose is twofold: to apply Green's functions for the linearized IGWs generators in baroclinic geostrophic adjustment processes (here for the 2–D case, the 3–D situation is presented in appendix B) and to verify the Fourier integral results developed in section 3.6.

3.7.1 Green's Functions

The Green's functions desired for eq. (3.20) may be constructed as

$$\begin{pmatrix} L_1 G_u \\ L_2 G_v \\ L_2 G_w \\ L_1 G_\theta \end{pmatrix} = -\delta(y)\delta(z) \begin{pmatrix} \delta(t)'' & +N^2\delta(t) \\ -f\delta(t) & \\ f\delta(t) & \\ -\frac{f\bar{\theta}N^2}{g}\delta(t) & \end{pmatrix}, \tag{3.34}$$

where G denotes the Green's function.

In order to reduce the problem to be only a function of space initially, a Laplace transform defined by

$$\tilde{\varphi} = \int_0^{+\infty} \varphi e^{-\sigma t}, \qquad \sigma > 0, \tag{3.35}$$

Reproduced with permission of the copyright owner. Further reproduction prohibited without permission.

is applied to eq. (3.34). Then substituting with

$$z = \sqrt{\frac{\sigma^2 + f^2}{\sigma^2 + N^2}}\mu, \tag{3.36}$$

eq. (3.34) becomes

$$L_G \begin{pmatrix} \tilde{G}_u \\ \tilde{G}_v \\ \tilde{G}_w \\ \tilde{G}_\theta \end{pmatrix} = -\frac{\delta(y)\delta(\mu)}{\sqrt{\sigma^2 + N^2}\sqrt{\sigma^2 + f^2}} \begin{pmatrix} \sigma & +\frac{(\sigma^2+N^2)}{\sigma} \\ -f & \\ f & \\ -\frac{f\bar{\theta}N^2}{g} & \end{pmatrix}, \tag{3.37}$$

where

$$L_G = \frac{\partial^2}{\partial y^2} + \frac{\partial^2}{\partial \mu^2} \tag{3.38}$$

Note that the tilde here means a Laplace transform and G_u is the Green's function for u, *etc.* In addition, σ represents the frequencies of the induced IGWs and $\sigma^2 \ll N^2$ is assumed from the analysis of the transient fields in previous sections. Applying $\sigma^2 \ll N^2$ to eq. (3.37) results in a expression identical to that obtained with the hydrostatic approximation.

Applying the hydrostatic approximation (this will be much simpler than the nonhydrostatic case in the Green's function analysis), eq. (3.37) reduces to

$$L_G \begin{pmatrix} \tilde{G}_u \\ \tilde{G}_v \\ \tilde{G}_w \\ \tilde{G}_\theta \end{pmatrix} = -\frac{\delta(y)\delta(\mu)}{N\sqrt{\sigma^2 + f^2}} \begin{pmatrix} \sigma & +\frac{N^2}{\sigma} \\ -f & \\ f & \\ -\frac{f\bar{\theta}N^2}{g\sigma} & \end{pmatrix}. \tag{3.39}$$

Eq. (3.39) is solved in free space (Butkovskiy, 1982). However, it is better to reorganize the solutions as follows so that they are convenient for the reverse Laplace transform to follow. This may be written as

$$\begin{pmatrix} \tilde{G}_u \\ \tilde{G}_v \\ \tilde{G}_w \\ \tilde{G}_\theta \end{pmatrix} = \frac{1}{2\pi N\sqrt{\sigma^2 + f^2}} ln \frac{\sqrt{\sigma^2 + a^2}}{\sqrt{\sigma^2 + a_0^2}} \begin{pmatrix} \sigma & +\frac{N^2}{\sigma} \\ -f & \\ f & \\ -\frac{f\bar{\theta}N^2}{g\sigma} & \end{pmatrix}, \tag{3.40}$$

Reproduced with permission of the copyright owner. Further reproduction prohibited without permission.

where $\hat{y} = y - \xi$; $\hat{z} = z - \zeta$; $z_0 = z + \zeta$; $a^2 = f^2 + N^2\hat{z}^2/(\hat{x}^2 + \hat{y}^2)$ and $a_0^2 = f^2 + N^2\hat{z}_0^2/(\hat{x}^2 + \hat{y}^2)$. Eq. (3.40) is transformed back to the time domain and finally yields the Green's functions for u, v, w and θ (Oberhettinger,1973; Spanier,1987)

$$\begin{aligned} G_u(y,z,t;\xi,\zeta) &\equiv G_u^{(1)} + G_u^{(2)} \\ &= \frac{1}{2\pi N}\int_0^t \frac{1}{\tau^2}[cos(a\tau) + a\tau sin(a\tau) - cos(a_0\tau) - a_0\tau sin(a_0\tau)] \\ &\cdot J_0[f(t-\tau)]d\tau \\ &+\frac{1}{4N}\int_0^t \tau \frac{cos[a_0(t-\tau)] - cos[a(t-\tau)]}{t-\tau} \\ &\cdot\{J_0(f\tau)[\frac{2}{\pi} - H_1(f\tau)] + J_1(f\tau)H_0(f\tau)\}d\tau, \end{aligned} \tag{3.41}$$

$$G_{v,w} = \frac{1}{2\pi N}\int_0^t \frac{cos(a_0\tau) - cos(a\tau)}{\tau} J_0[f(t-\tau)]d\tau, \tag{3.42}$$

and

$$G_\theta = G_u^{(2)}. \tag{3.43}$$

where J and H are Bessel and Struve's functions.

3.7.2 Numerical Results

For a point source (Dickinson, 1969a, b) located at $(\xi, \zeta) = (0, 0)$, the solutions for the field variables are

$$S^*(t) \cdot G_{u,v,w,\theta}(y, z.t; 0, 0). \tag{3.44}$$

where $S^*(t)$ denotes the given source strength. In the case of this investigation, the source is a function of space, so the solutions are

$$u = \int\int_S [G_u^{(1)} M_{zz}(\xi,\zeta) + G_u^{(2)} M_{yy}(\xi,\zeta)]d\xi d\zeta, \tag{3.45}$$

Reproduced with permission of the copyright owner. Further reproduction prohibited without permission.

$$v = \int\int_S G_v M_{zz}(\xi,\zeta)d\xi d\zeta, \tag{3.46}$$

$$w = \int\int_S G_w M_{yz}(\xi,\zeta)d\xi d\zeta, \tag{3.47}$$

and

$$\theta = \int\int_S G_\theta M_{yz}(\xi,\zeta)d\xi d\zeta. \tag{3.48}$$

where S is an unbounded 2-D space.

Owing to the tedious integral computation and the application of this technique here primarily to verify consistency with the Fourier integral technique, these comparisons have been performed only at one point. The numerical scheme is again the integral subroutine named QAND of the new IMSL package. The numerical results are sought to satisfy a designed relative error of 10^{-5} when changing the integral limits. The numerical results at $(y,z) = (100,1)km$ are exhibited in Fig. 3.18.

Comparison with the solutions at this location obtained using Fourier integral techniques (see Fig. 3.14), it can be seen that there are only small deviations of the solutions between the two techniques. Because of the uncertainties introduced by numerical evaluation of the integral expressions, however, these differences are likely due to the numerical techniques employed. Especially, the mean in the Green's function result of 1.38 m/s is only 0.02 m/s away from the Fourier integral mean solution and the wave periods are consistent to a high degree.

Reproduced with permission of the copyright owner. Further reproduction prohibited without permission.

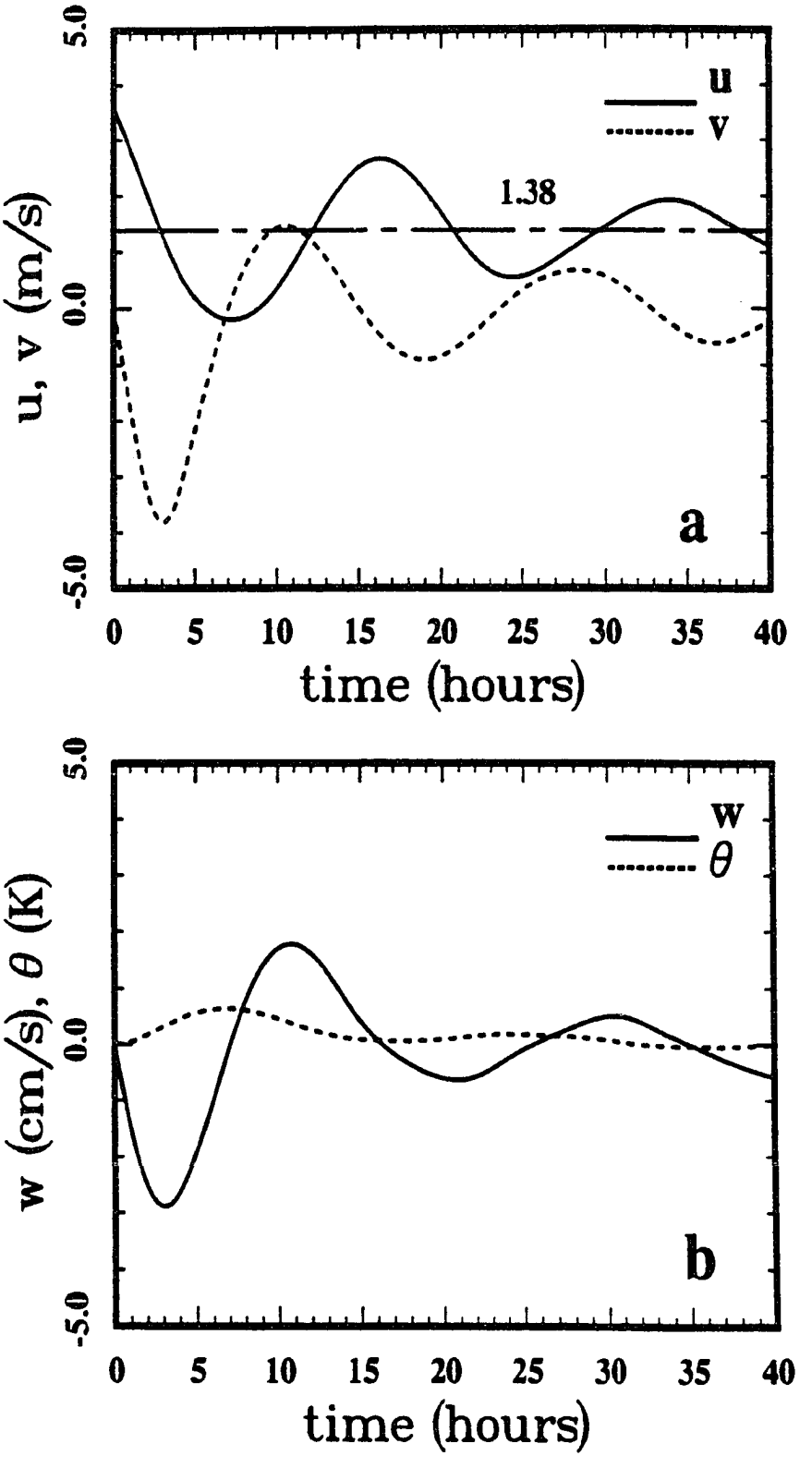

Figure 3.18 As in figure 3.14 but for the Green's function solutions.

Reproduced with permission of the copyright owner. Further reproduction prohibited without permission.

3.8 Comments on 2–D Adjustment

Geostrophic adjustment processes may be a competitive source mechanism for low–frequency internal gravity waves based on their frequent association with the jet stream. The atmospheric jet stream is one location where large departures from geostrophic flow occur. Two approximations were followed in this chapter. First, it was assumed that all the initial ageostrophic energy would be radiated as IGWs. Second, the full solution was obtained including IGWs and an altered mean state that conserved potential vorticity. Consideration of an infinite jet stream reduced the problem to a 2–D domain. The initial disturbance was assumed to be an ageostrophic Gaussian jet. A ratio of horizonal–to–vertical extent of 100:1 for the jet forcing was chosen to represent an ageostrophic component of comparable geometry, but of smaller scale, than the atmospheric jet stream (Cammas and Raymond, 1989).

The model used here can be shown to conserve potential vorticity and energy for the full solutions. In both approximate and full solutions, IGWs radiated by the infinite jet stream adjustment in this investigation had very low frequencies varying from $\sim f - 4f$, with lower–frequency waves propagating more nearly horizontally.

The bulk of unbalanced energy was radiated along shallow propagation paths from the jet core because of the shallow jet stream structure assumed. The choice of initially unbalanced momentum scale also implied a major vertical wavelength of $\sim 6 - 8km$ which must be seen easily from the time–height cross sections. The meridional wavelength is $\sim$ 100 times as large as the vertical and is imposed by the ratio of the initially jet structure. The horizonal wave fields were symmetric

Reproduced with permission of the copyright owner. Further reproduction prohibited without permission.

but the vertical motion and temperature fields were antisymmetric about the jet axes due to the symmetry of the jet and the influences of rotation.

All unbalanced energy is radiated as IGWs in the homogeneous problem because geostrophic adjustment is artificially suppressed. This is different from the barotropic geostrophic adjustment problem. The reason is not the application to shallow water or a deep atmosphere, but because of the different character of the wave modes permitting adjustment with and without stratification. Besides the wave structure, a major difference in the two solutions is also the adjustment time scale as shown in the figures.

The IGW structure induced by nonhomogeneous treatment in the full adjustment problem is essentially equivalent to that in the approximate solution. However, full solution also produces a weak balanced jet as well. This phenomenon is similar to the results by Zhu and Holton (1987) where they examined the contribution to the mean state from forcing by a gravity wave packet. Generalization of these results to a 3–D localized jet are presented in the following chapter.

Reproduced with permission of the copyright owner. Further reproduction prohibited without permission.

Chapter 4

IGW Excitation by a Localized Ageostrophic Gaussian Jet

The jet streams in the troposphere and lower stratosphere have been observed to be shallow, with a vertical scale much smaller than their horizontal extent. In addition, their east–west scale is finite, with departures from geostrophy having scales of a few thousand kilometers or less (see Cammas and Raymond, 1989; for instance). Thus, to address the geostrophic adjustment of more realistic jet streams, a three–dimensional (3–D) investigation is needed.

4.1 Governing Equations

A full response to an ageostrophic 3–D Gaussian jet assuming a nonhomogeneous term similar to that of section 3.6 is examined here. Adopting the dynamical approximations of the last chapter and applying the hydrostatic approximation for the reasons cited in section 3.5, the primitive equations for the geostrophic adjustment process of a localized atmospheric jet stream are obtained from Appendix A by letting $\eta = 1$ and $\varepsilon_h = 0$ in eqs. (A.7)–(A.11)

Reproduced with permission of the copyright owner. Further reproduction prohibited without permission.

$$\frac{\partial u}{\partial t} + \frac{1}{\rho_0}\frac{\partial p}{\partial x} - fv = F_x\delta(t), \tag{4.1}$$

$$\frac{\partial v}{\partial t} + \frac{1}{\rho_0}\frac{\partial p}{\partial y} + fu = 0, \tag{4.2}$$

$$\frac{1}{\rho_0}\frac{\partial p}{\partial z} - \frac{g}{\bar{\theta}}\theta = 0, \tag{4.3}$$

$$\frac{\partial u}{\partial x} + \frac{\partial v}{\partial y} + \frac{\partial w}{\partial z} = 0, \tag{4.4}$$

$$\frac{\partial \theta}{\partial t} + \frac{\bar{\theta}}{g}N^2 w = 0, \tag{4.5}$$

where we have assumed the same orientation of the jet stream in the Cartesian coordinates as before, with x along with the jet core to the east, y towards the north, and z upwards. All notation is as before. In this application, a momentum source is imposed by $F_x\delta(t)$ in the zonal direction with F_x having the 3–D structure

$$F_x = u_* exp[-(\frac{x^2}{2\sigma_x^2} + \frac{y^2}{2\sigma_y^2} + \frac{z^2}{2\sigma_z^2})], \tag{4.6}$$

with u, v, w, θ, u_t, v_t, w_t and θ_t all zero initially. The spatial domain is unbounded and all perturbations are assumed to vanish at infinity.

A matrix equation which has been derived in Appendix A (eq. A.20) for all field variables based on eqs. (4.1)–(4.5) is

$$\begin{pmatrix} L_1 u \\ L_1 v \\ L_2 w \\ L_1 \theta \end{pmatrix} = \begin{matrix} Part\ 1 \qquad\qquad Part\ 2 \\ \begin{pmatrix} M_{zz}\delta''(t) & +N^2 M_{yy}\delta(t) \\ -fM_{zz}\delta'(t) & -N^2 M_{xy}\delta(t) \\ fM_{yz}\delta(t) & -M_{xz}\delta'(t) \\ -\frac{f\bar{\theta}N^2}{g}M_{yz}\delta(t) & +\frac{\bar{\theta}N^2}{g}M_{xz}\delta'(t) \end{pmatrix} \end{matrix}, \tag{4.7}$$

where

$$L_1 = \frac{\partial}{\partial t}[(\frac{\partial^2}{\partial t^2} + f^2)\frac{\partial^2}{\partial z^2} + N^2\Delta_2], \tag{4.8}$$

Reproduced with permission of the copyright owner. Further reproduction prohibited without permission.

$$L_2 = (\frac{\partial^2}{\partial t^2} + f^2)\frac{\partial^2}{\partial z^2} + N^2\Delta_2, \tag{4.9}$$

and notation is as in Appendix A.

4.2 Emerging Fields Induced by Geostrophic Adjustment of an Unbalanced Localized Gaussian Jet

There are two ways in which solutions of the 3–D problem are expected to differ from the 2–D results. The 3–D wave field will contain components with some zonal propagation, and the resulting mean state in the 3–D problem must include a localized mean circulation. This 3–D baroclinic geostrophic adjustment problem will be solved using Fourier transform technique in this chapter, with the Green's function solutions presented in Appendix B.

4.2.1 Fourier Integral Expressions

First we introduce the 3–D Fourier transform pairs

$$\tilde{\psi} = \frac{1}{(2\pi)^3}\int\int_{-\infty}^{+\infty}\int \psi(\vec{r},t)e^{-i\vec{\kappa}\cdot\vec{r}}dxdydz \tag{4.10}$$

and

$$\psi = \int\int_{-\infty}^{+\infty}\int \tilde{\psi}(\vec{\kappa},t)e^{i\vec{\kappa}\cdot\vec{r}}dkdldm, \tag{4.11}$$

with all notation as before.

Employing eq. (4.11), eq. (4.8) becomes

$$L\begin{pmatrix}\tilde{u}\\ \tilde{v}\\ \tilde{w}\\ \tilde{\theta}\end{pmatrix} = \frac{1}{m^2}\begin{pmatrix}-\tilde{M}_{zz}\delta'(t) & -N^2\tilde{M}_{yy}\\ f\tilde{M}_{zz}\delta(t) & +N^2\tilde{M}_{xy}\\ -f\tilde{M}_{yz}\delta(t) & +\tilde{M}_{xz}\delta'(t)\\ \frac{f\bar{\theta}N^2}{g}\tilde{M}_{yz} & -\frac{\bar{\theta}N^2}{g}\tilde{M}_{xz}\delta(t)\end{pmatrix}, \tag{4.12}$$

Reproduced with permission of the copyright owner. Further reproduction prohibited without permission.

where

$$L = \frac{d^2}{dt^2} + \omega_h^2, \tag{4.13}$$

ω_h denotes the hydrostatic IGWs frequency defined by eq. (3.19), and

$$\begin{pmatrix} \tilde{M}_{zz} \\ \tilde{M}_{yy} \\ \tilde{M}_{xy} \\ \tilde{M}_{yz} \\ \tilde{M}_{xz} \end{pmatrix} = -\frac{u_* \sigma_x \sigma_y \sigma_z}{(2\pi)^{3/2}} exp[-(\frac{\sigma_x^2}{2}k^2 + \frac{\sigma_y^2}{2}l^2 + \frac{\sigma_z^2}{2}m^2)] \begin{pmatrix} m^2 \\ l^2 \\ kl \\ lm \\ km \end{pmatrix}. \tag{4.14}$$

Using eq. (4.7) and the Fourier transform, eq. (4.11), eq. (4.13) can be solved yielding a solution

$$\begin{pmatrix} \tilde{u} \\ \tilde{v} \\ \tilde{w} \\ \tilde{\theta} \end{pmatrix} = \frac{1}{m^2} \begin{pmatrix} -\tilde{M}_{zz} cos(\omega_h t) & -\frac{N^2}{\omega_h^2}\tilde{M}_{yy}[1 - cos(\omega_h t)] \\ \frac{f}{\omega_h}\tilde{M}_{zz} sin(\omega_h t) & +\frac{N^2}{\omega_h^2}\tilde{M}_{xy}[1 - cos(\omega_h t)] \\ -\frac{f}{\omega_h}\tilde{M}_{yz} sin(\omega_h t) & +\tilde{M}_{xz} cos(\omega_h t) \\ \frac{f\bar{\theta}N^2}{g\omega_h^2}\tilde{M}_{yz}[1 - cos(\omega_h t)] & -\frac{\bar{\theta}N^2}{g\omega_h}\tilde{M}_{xz} sin(\omega_h t) \end{pmatrix}. \tag{4.15}$$

Note the differences of $\tilde{M}_{yy}$, $\tilde{M}_{yz}$ and $\tilde{M}_{zz}$ from the 2–D results due to the different F_x between the two cases. As before, explicit expressions for all field variables can be obtained if eq. (4.16) is transformed back to the physical domain. Again, for the sake of convenience, all solutions are presented in two parts using superscripts (1) and (2) which correspond to the two nonhomogeneous terms given in eq. (4.8). The complete solutions are the combination of those two parts, with the zonal terms given by

$$\begin{aligned} u^{(1)}(x,y,z,t) &= \frac{8u_*\sigma_x\sigma_y\sigma_z}{(2\pi)^{3/2}} \int_{0+}^{+\infty}\int\int exp[-(\frac{\sigma_x^2k^2}{2} + \frac{\sigma_y^2l^2}{2} + \frac{\sigma_z^2m^2}{2})]cos(kx)cos(ly) \\ &\quad \cdot cos(mz)cos(\sqrt{f^2 + \frac{(k^2+l^2)}{m^2}N^2}t)dkdldm \end{aligned} \tag{4.16}$$

Reproduced with permission of the copyright owner. Further reproduction prohibited without permission.

and

$$u^{(2)}(x,y,z,t) = \frac{8u_*N^2\sigma_x\sigma_y\sigma_z}{(2\pi)^{3/2}}\int_{0+}^{+\infty}\int\frac{l^2}{f^2m^2+N^2(k^2+l^2)} \cdot exp[-(\frac{\sigma_x^2k^2}{2}+\frac{\sigma_y^2l^2}{2}+\frac{\sigma_z^2m^2}{2})]cos(kx)cos(ly)cos(mz) \cdot[1-cos(\sqrt{f^2+\frac{(k^2+l^2)}{m^2}N^2t})]dkdldm. \quad (4.17)$$

The mean obtained from $u^{(2)}$ has the form

$$\bar{u}(x,y,z) = \frac{8u_*N^2\sigma_x\sigma_y\sigma_z}{(2\pi)^{3/2}}\int_{0+}^{+\infty}\int\frac{l^2}{f^2m^2+N^2(k^2+l^2)}cos(kx)cos(ly)cos(mz) \cdot exp[-(\frac{\sigma_x^2k^2}{2}+\frac{\sigma_y^2l^2}{2}+\frac{\sigma_z^2m^2}{2})]dkdldm. \quad (4.18)$$

Likewise, for v we obtain

$$v^{(1)}(x,y,z,t) = -\frac{8fu_*\sigma_x\sigma_y\sigma_z}{(2\pi)^{3/2}}\int_{0+}^{+\infty}\int\frac{m}{\sqrt{f^2m^2+N^2(k^2+l^2)}} \cdot exp[-(\frac{\sigma_x^2k^2}{2}+\frac{\sigma_y^2l^2}{2}+\frac{\sigma_z^2m^2}{2})]cos(kx)cos(ly)cos(mz) \cdot sin(\sqrt{f^2+\frac{(k^2+l^2)}{m^2}N^2t})dkdldm \quad (4.19)$$

and

$$v^{(2)}(x,y,z,t) = \frac{8u_*N^2\sigma_x\sigma_y\sigma_z}{(2\pi)^{3/2}}\int_{0+}^{+\infty}\int\frac{kl}{f^2m^2+N^2(k^2+l^2)} \cdot exp[-(\frac{\sigma_x^2k^2}{2}+\frac{\sigma_y^2l^2}{2}+\frac{\sigma_z^2m^2}{2})]sin(kx)sin(ly)cos(mz) \cdot[1-cos(\sqrt{f^2+\frac{(k^2+l^2)}{m^2}N^2t})]dkdldm, \quad (4.20)$$

with a mean meridional motion from $v^{(2)}$ given by

$$\bar{v}(x,y,z) = \frac{8u_*N^2\sigma_x\sigma_y\sigma_z}{(2\pi)^{3/2}}\int_{0+}^{+\infty}\int\frac{kl}{f^2m^2+N^2(k^2+l^2)}sin(kx)sin(ly)cos(mz) \cdot exp[-(\frac{\sigma_x^2k^2}{2}+\frac{\sigma_y^2l^2}{2}+\frac{\sigma_z^2m^2}{2})]dkdldm. \quad (4.21)$$

Reproduced with permission of the copyright owner. Further reproduction prohibited without permission.

The corresponding vertical motion field is

$$w^{(1)}(x,y,z,t) = -\frac{8fu_*\sigma_x\sigma_y\sigma_z}{(2\pi)^{3/2}}\int_{0+}^{+\infty}\int\frac{l}{\sqrt{N^2(k^2+l^2)+f^2m^2}} \cdot exp[-(\frac{\sigma_x^2k^2}{2}+\frac{\sigma_y^2l^2}{2}+\frac{\sigma_z^2m^2}{2})]cos(kx)sin(ly)sin(mz) \cdot sin(\sqrt{f^2+\frac{(k^2+l^2)}{m^2}N^2}t)dkdldm \quad (4.22)$$

and

$$w^{(2)}(x,y,z,t) = \frac{8u_*\sigma_x\sigma_y\sigma_z}{(2\pi)^{3/2}}\int_{0+}^{+\infty}\int\frac{k}{m}exp[-(\frac{\sigma_x^2k^2}{2}+\frac{\sigma_y^2l^2}{2}+\frac{\sigma_z^2m^2}{2})]sin(kx) \cdot cos(ly)sin(mz)cos(\sqrt{f^2+\frac{(k^2+l^2)}{m^2}N^2}t)dkdldm. \quad (4.23)$$

It is important to note that there exists no mean state in the vertical motion field because a nonzero vertical motion would lead to a vertical divergence field and additional wave radiation. The associated θ fields are given by

$$\theta^{(1)}(x,y,z,t) = \frac{8\bar{\theta}N^2fu_*\sigma_x\sigma_y\sigma_z}{g(2\pi)^{3/2}}\int_{0+}^{+\infty}\int\frac{lm}{N^2(k^2+l^2)+f^2m^2} \cdot exp[-(\frac{\sigma_x^2k^2}{2}+\frac{\sigma_y^2l^2}{2}+\frac{\sigma_z^2m^2}{2})]cos(kx)sin(ly)sin(mz) \cdot [1-cos(\sqrt{f^2+\frac{(k^2+l^2)}{m^2}N^2}t)]dkdldm \quad (4.24)$$

and

$$\theta^{(2)}(x,y,z,t) = -\frac{8\bar{\theta}N^2u_*\sigma_x\sigma_y\sigma_z}{g(2\pi)^{3/2}}\int_{0+}^{+\infty}\int\frac{k}{\sqrt{N^2(k^2+l^2)+f^2m^2}} \cdot exp[-(\frac{\sigma_x^2k^2}{2}+\frac{\sigma_y^2l^2}{2}+\frac{\sigma_z^2m^2}{2})]sin(kx)cos(ly)sin(mz) \cdot sin(\sqrt{f^2+\frac{(k^2+l^2)}{m^2}N^2}t)dkdldm. \quad (4.25)$$

Reproduced with permission of the copyright owner. Further reproduction prohibited without permission.

4.2.2 Computational Approaches

In order to compare with the results for the infinite jet stream case developed in last chapter, a shallow jet has been chosen with $\sigma_x = 1000km$ (10 time larger than σ_y) in eq. (4.6) while keeping all other constants as before. Comparing the 3–D solutions, eqs. (4.16)–(4.25), and the 2–D expressions, eqs. (3.27)–(3.33), for the full adjustment problem, we see that all the part 1 solutions for the localized and infinite jet streams are the same except that motions follow their own dispersion relationship and there is a cosine integration factor in the 3–D case. These results indicate that the wave behaviour is similar except that waves propagate in the zonal direction to some extent in the 3–D case. The extra terms which are described in part 2 of the solutions in the 3–D case (except the zonal motion field) arise from the zonal gradient of the initial unbalanced momentum distribution and are correction terms to the 2–D simulations. The numerical method used to value eqs. (4.16)–(4.25) has been presented in section 3.3 in the last chapter.

To examine the 3–D solutions, let us first compute the wave behavior on the $x = 0$ plane. Fig. 4.1 shows part 2 of the solutions at $(x, y, z) = (0, 100, 1)km$, where $w^{(2)}$ and $\theta^{(2)}$ are identically zero from eqs. (4.23) and (4.25). This is because of the symmetric initially unbalanced momentum structure assumed and the IGWs resulting from the initial zonal divergence cancelling each other completely on $x = 0$ plane. The 3–D correction term for the meridional motion, $v^{(2)}$, is very small. A relatively larger correction for the zonal motion at early times ($< T_i$) does not simply modulate the major wave component represented by part 1 ($u^{(1)}$, see also Fig. 4.2) but also alters the phase of part 1 with its own near initial period T_i. This relatively large motion owes its existence to the repartitioning

Reproduced with permission of the copyright owner. Further reproduction prohibited without permission.

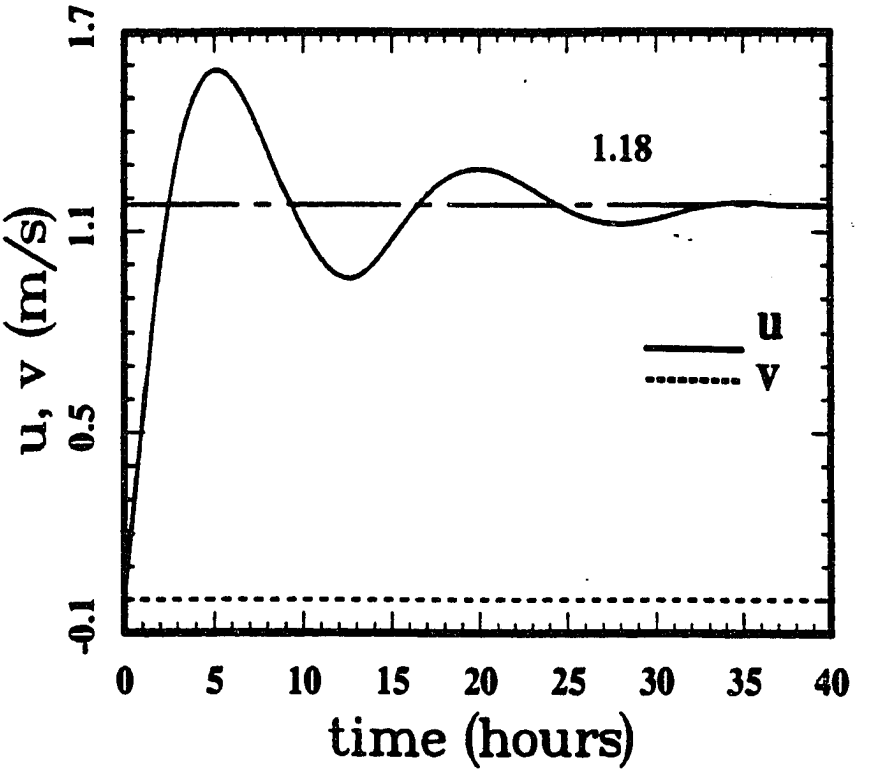

Figure 4.1 Part 2 of the horizontal velocity field at (x,y,z)=(0,100,1) km. The zonal mean (1.18m/s) is slightly smaller than the 2–D case (1.40m/s in figure 3.14).

of the energy in the initial momentum source in the 3–D problem relative to the 2–D problem (see also Fig. 3.14, $1.18m/s$ to $1.40m/s$). Close to the jet axis ($x = 0$), the major portion of the motion field is represented by part 1 ($u^{(1)}$), the correction term is dominated by $u^{(1)}$, and the complete solution (Fig. 4.2) looks very similar to the 2–D case. In the transient motion field, the fluctuations of w and θ are similar to the 2–D results. Also the small deviations of horizontal motions emphasize the similarities of the IGW behaviour between the 2–D and 3–D adjustment processes.

Away from the $x = 0$ plane, Figs. 4.3 and 4.4 show part 2 of the 3–D solution at $(x, y, z) = (300, 100, 1)km$ and $(1000, 100, 1)km$. Here again the motions on the $x = 300km$ and $1000km$ planes are considered and one point at $(y, z) =$

Reproduced with permission of the copyright owner. Further reproduction prohibited without permission.

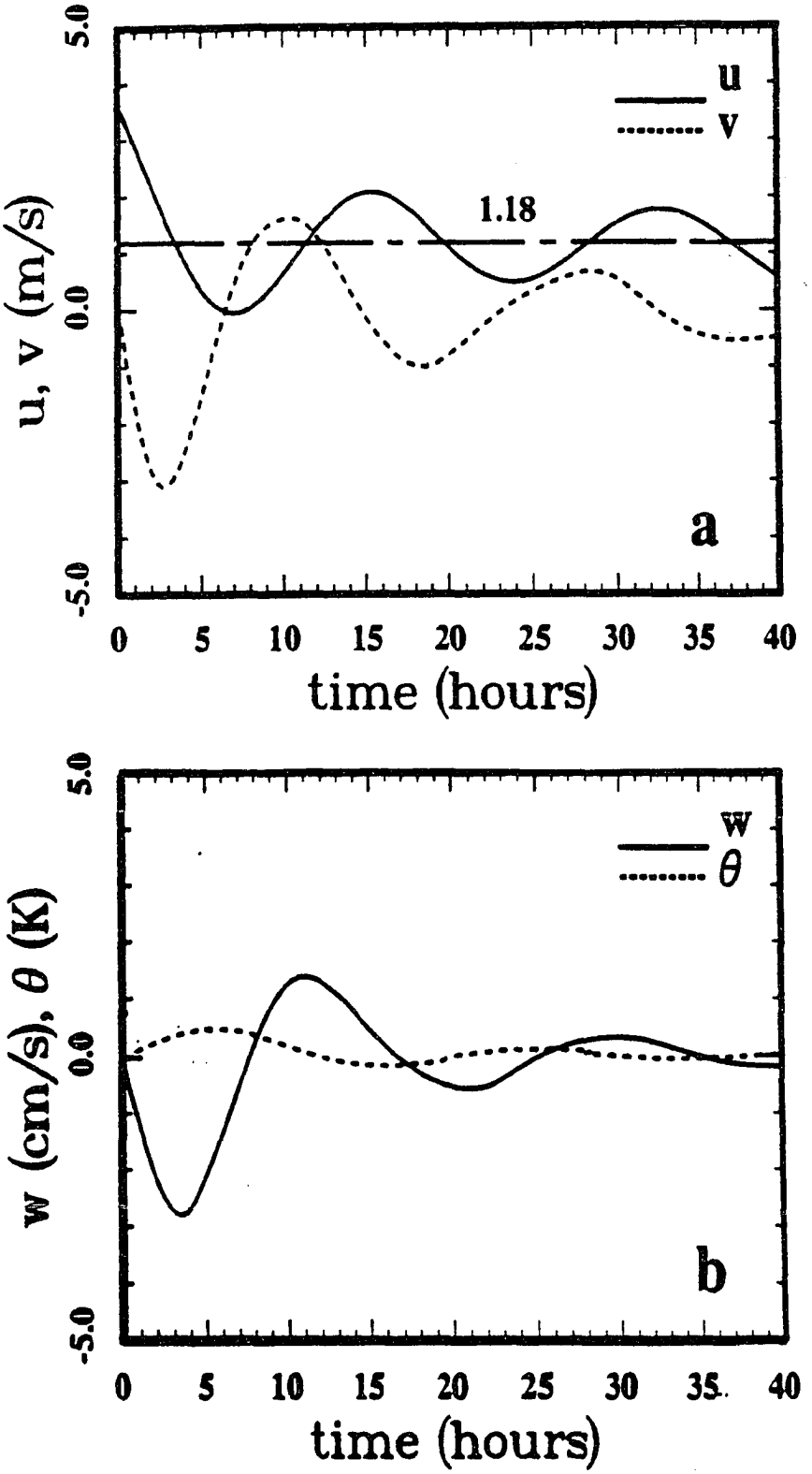

Figure 4.2 Complete solution (parts 1 and 2) for the horizontal velocity perturbations (a), vertical velocity and thermal perturbations (b) at (x,y,z)=(0,100,1) km.

Reproduced with permission of the copyright owner. Further reproduction prohibited without permission.

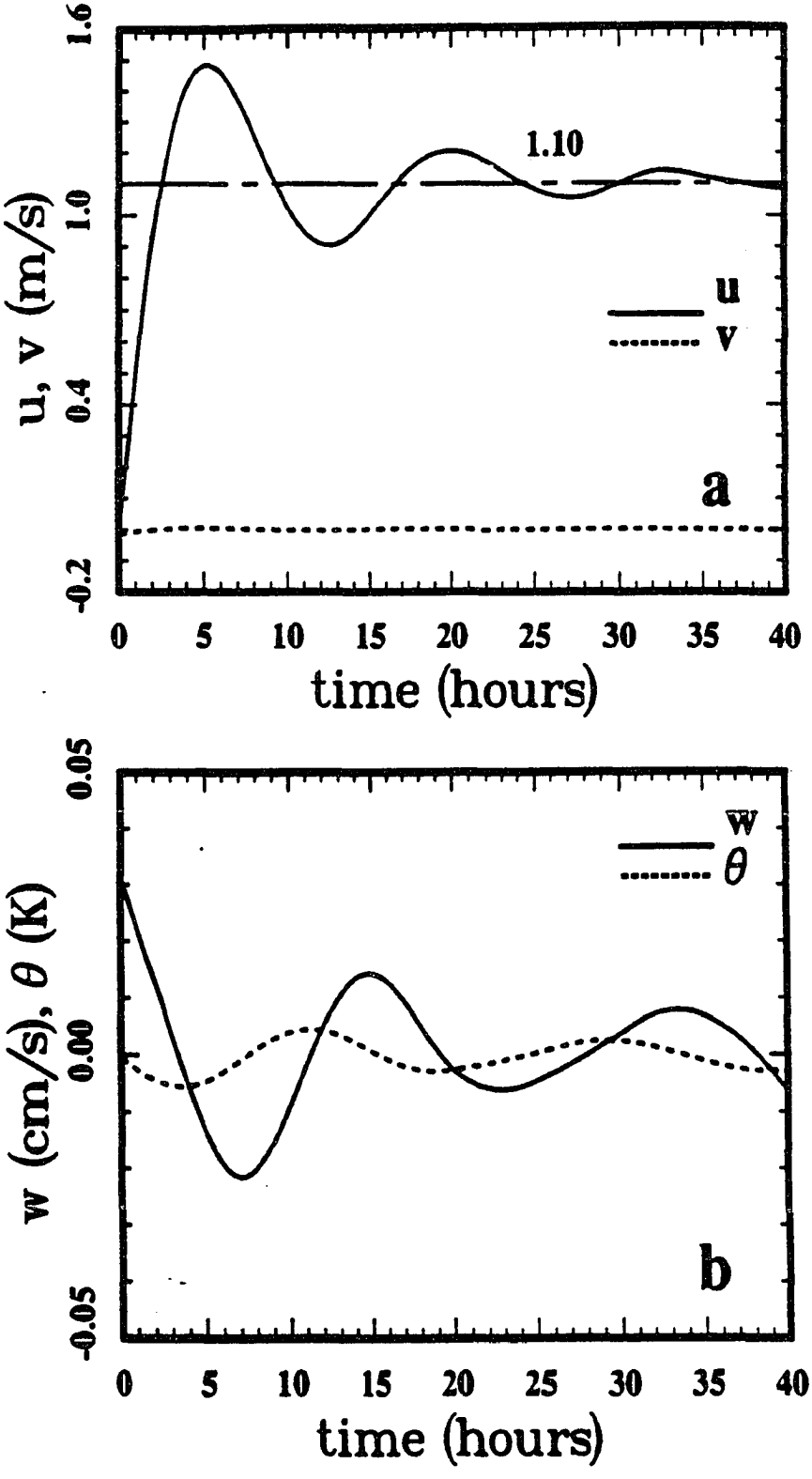

Figure 4.3 Part 2 of the horizontal velocity fluctuations (a) and vertical velocity and temperature fluctuations (b) at (x,y,z)=(300,100,1) km.

Reproduced with permission of the copyright owner. Further reproduction prohibited without permission.

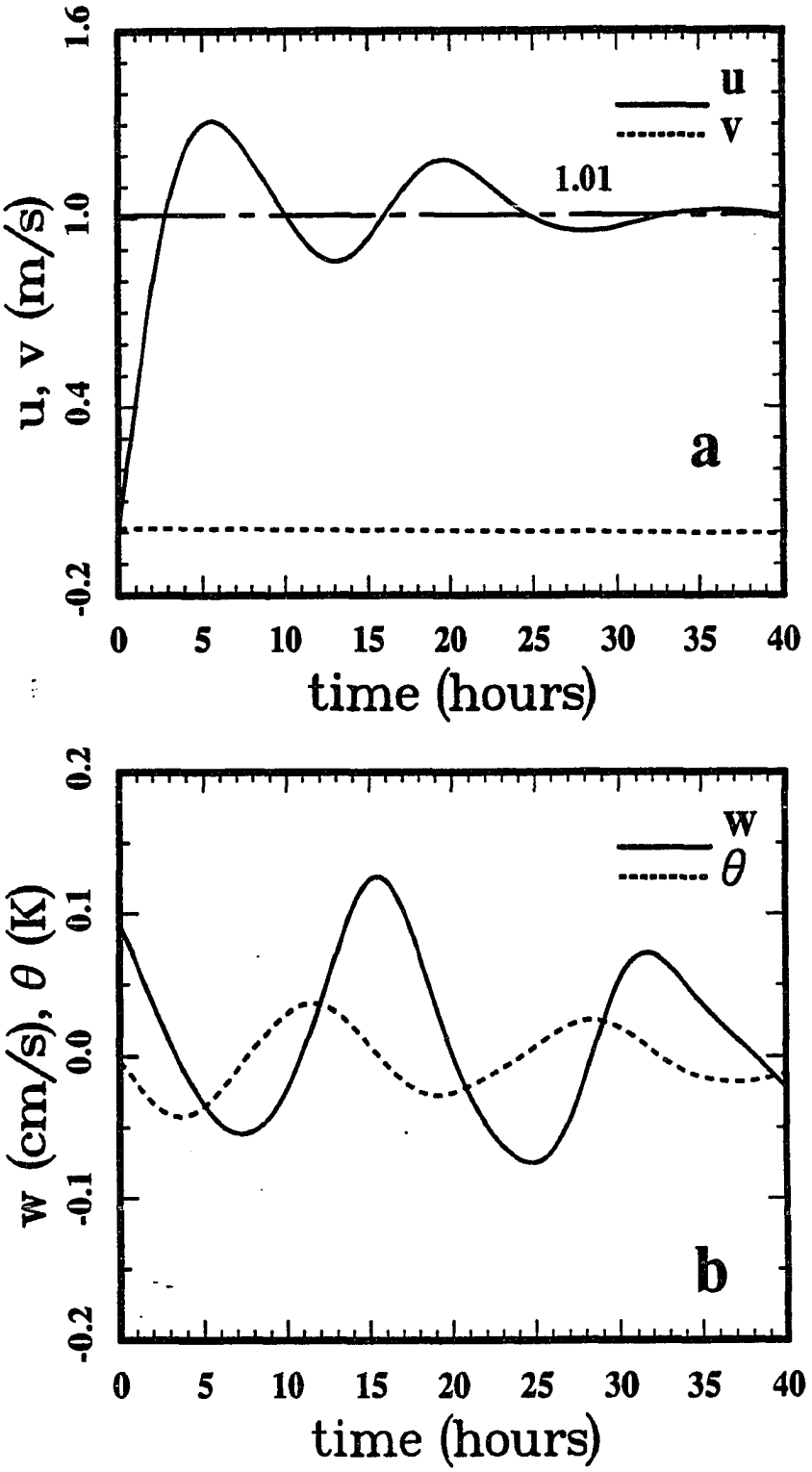

Figure 4.4 As in figure 4.3 but (x,y,z)=(1000,100,1) km.

Reproduced with permission of the copyright owner. Further reproduction prohibited without permission.

$(100, 1)km$ on each plane is chosen for comparison. The consistent phase and slightly decreased amplitudes of zonal motion from point $(0, 100, 1)$ (see Fig. 4.1) to $(300, 100, 1)$ to $(1000, 100, 1)km$ suggest that the meridional propagation of IGWs remains dominant, with zonally propagating motions playing a much smaller role. The part 2 solutions for w and θ at $(300, 100, 1)km$ (Fig. 4.3(b)) have an initial period of $\sim$ 15 hours, which elongates to a period of $\sim T_i$ after about one inertial period. This behavior is similar to the wave fields in part 1 and also to the 2–D results. However, the amplitudes of $w^{(2)}$ and $\theta^{(2)}$ are very small. In addition, $v^{(2)}$ is small at (300,100,1) and (1000,100,1)km, suggesting that the 3–D results near the jet axis are closely approximated by the 2–D results. The wave behaviour in part 2 suggests that the induced waves with some propagation in the x direction can be considered separately without distorting the part 1 wave field character. This is because the model is linear so that all waves induced by different imposed nonhomogeneous terms will follow the same dispersion relation and yield independent contributions. A comparison of the full solution between (0,100,1) km (Fig. 4.2), (300,100,1) km (Fig. 4.5) and (1000,100,1) km (Fig. 4.6) also suggests only slight propagation in the x direction because the only clear differences in the wave fields among these three points are due to the Gaussian decay factor given by the initially unbalanced jet structure. At greater distances, the correction terms coming from part 2 of the solutions begin to have observed influences on the wave fields since the part 1 solutions are smaller at greater distances than their values close to the jet core. Fig. 4.7 shows part 2 solutions at (1000,1000,10)km. $v^{(2)}$ becomes more comparable to $u^{(2)}$ than at the vicinities of the jet core (Figs. 4.1 and 4.3). It is these correction terms that cause the differences in the early responses

Reproduced with permission of the copyright owner. Further reproduction prohibited without permission.

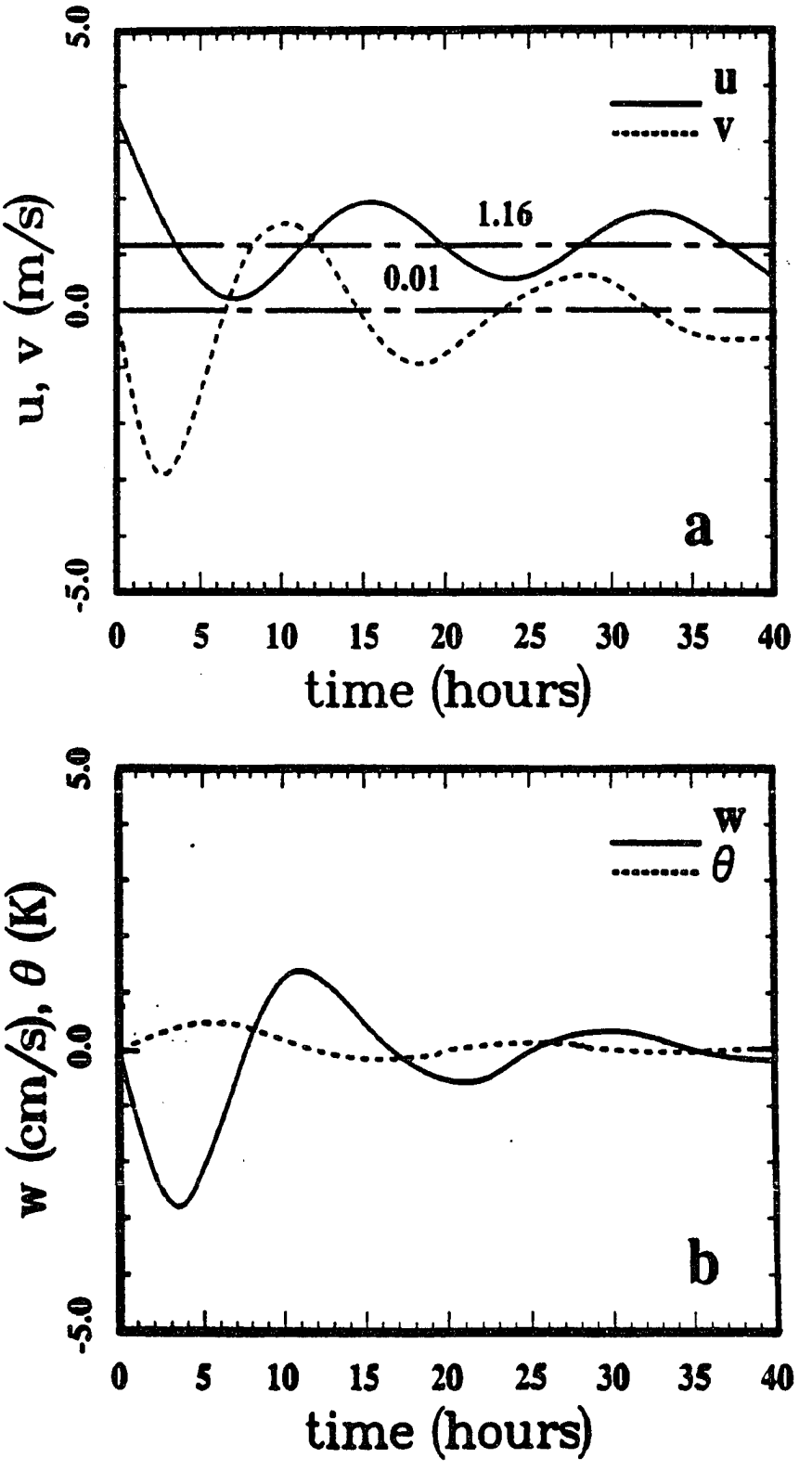

Figure 4.5 As in figure 4.2 but for (x,y,z)=(300,100,1) km.

Reproduced with permission of the copyright owner. Further reproduction prohibited without permission.

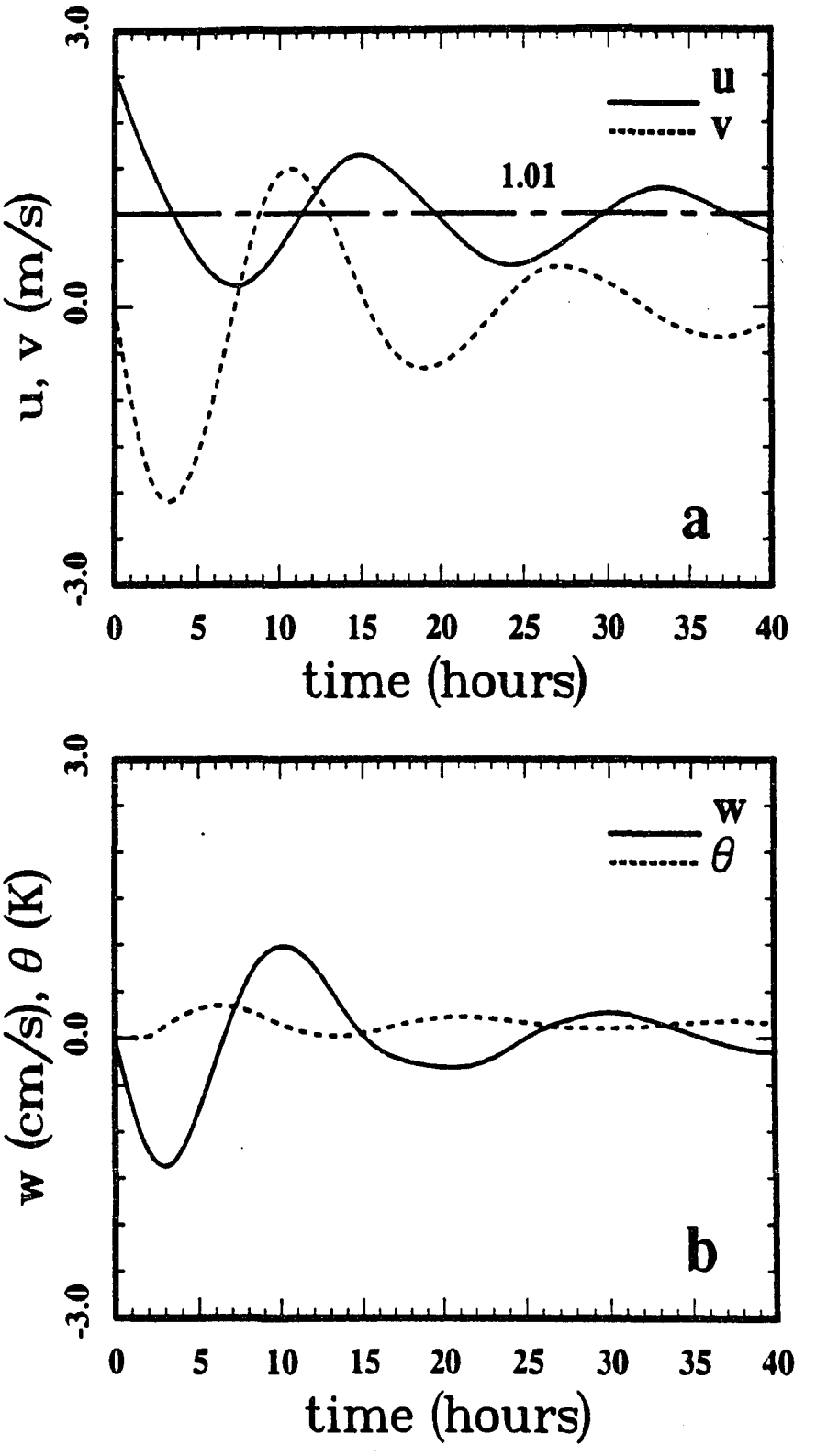

Figure 4.6 As in figure 4.2 but for (x,y,z)=(1000,100,1) km.

Reproduced with permission of the copyright owner. Further reproduction prohibited without permission.

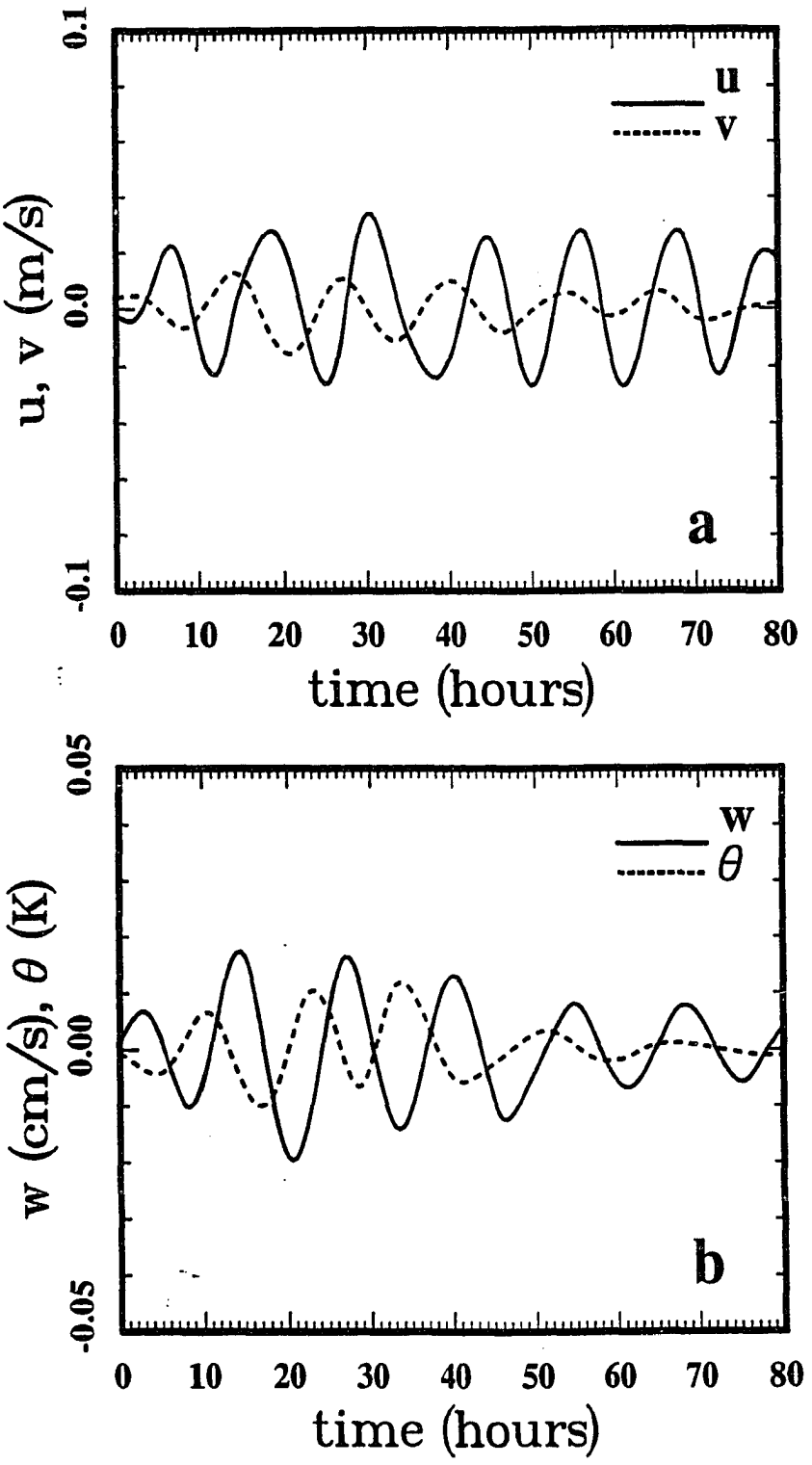

Figure 4.7 As in figure 4.3 but (x,y,z)=(1000,1000,10) km.

Reproduced with permission of the copyright owner. Further reproduction prohibited without permission.

between the 2–D and 3–D adjustments. The full solutions are presented in Figs. 4.8 and 4.9 for $(0, 1000, 10)km$ and $(1000, 1000, 10)km$. The large responses at $(x, y, z) = (0, 1000, 10)km$ occur ~20–60 hours after the excitation and implies a group velocities $\sim 5 - 15m/s$ which can also be seen from the 2–D case (see Fig. 3.4). Comparing Fig. 4.8 with Fig. 3.4, the early response in the 3–D case results from the zonally inhomogeneous distribution of the initially unbalanced momentum structure which implies the presence of zonal divergence. The observed larger v than u again implies the IGW propagation with a similar wave period and behaviour as in the 2–D case. Note here also the larger u than $v \sim 40h$ after the initial disturbance at $(1000, 1000, 10)km$ (Fig. 4.9(a)). This is because at later times, IGWs reaching that position arise from near the jet core and thus u and v have changed their relation and u now represents the primary propagation direction of those IGWs now present.

Fig. 4.10 shows the full solutions at a large zonal displacement, but closer to the horizontal jet axis, at $(x, y, z) = (1000, 1000, 3)km$. The smaller amplitudes of motions at this point compared to those at $(x, y, z) = (1000, 1000, 10)km$ (Fig. 4.9) again suggests that very few IGWs propagate along more horizontal paths. As a result, the entire field looks very similar between the 2–D and 3–D cases, with the decrease in wave amplitudes with increasing x due primarily to the Gaussian decay of the forcing in the x direction (Figs. 4.10 and 3.6).

After the IGWs propagate away from the localized initially unbalanced jet stream, the induced mean state has both zonal and meridional components. Figs. 4.11 and 4.12 exhibit the balanced zonal motions with $x - y$ and $y - z$ cross sections. A maximum $\bar{u}$ of $\sim 4m/s$ at the jet center (Fig. 4.11(a)) reveals a

Reproduced with permission of the copyright owner. Further reproduction prohibited without permission.

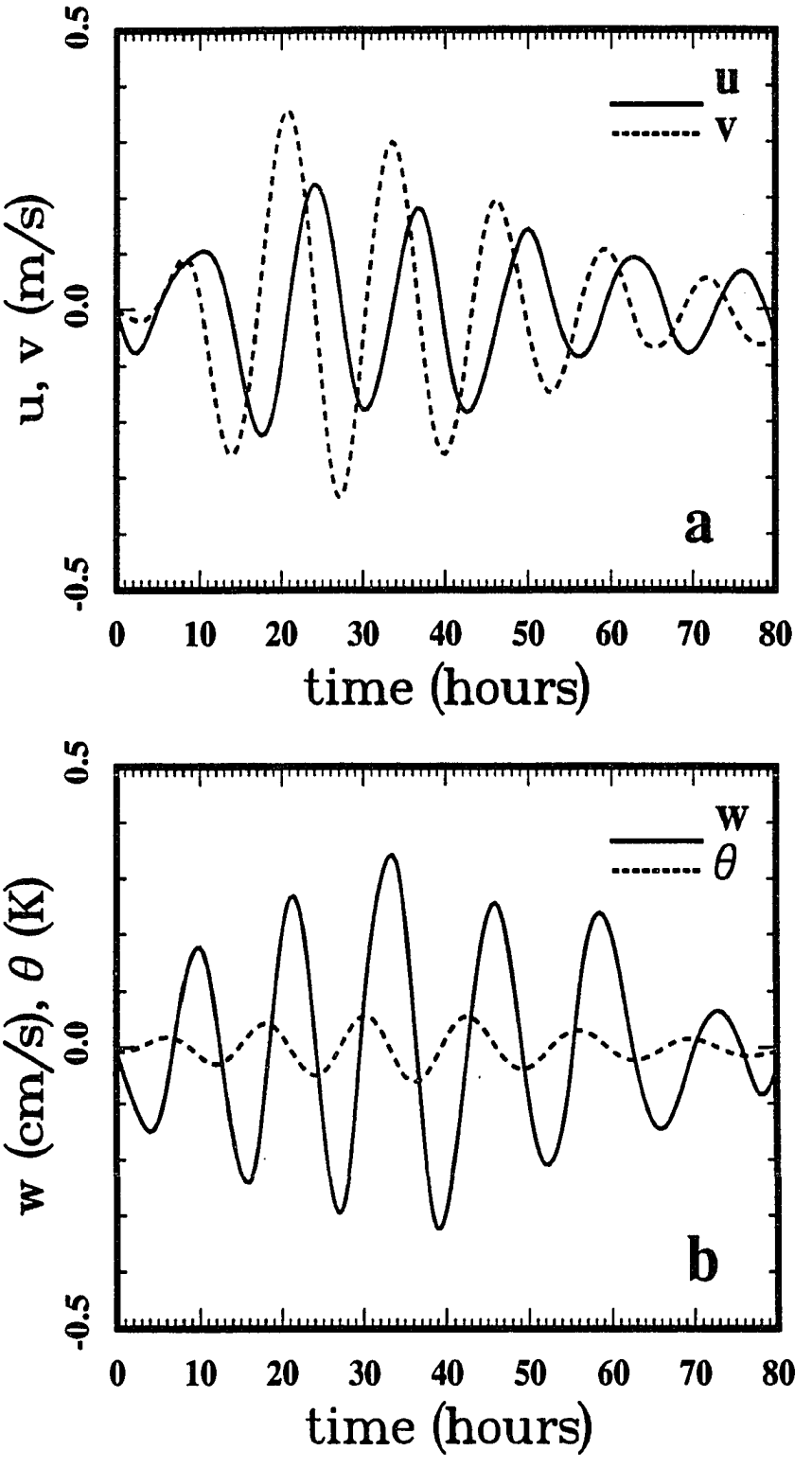

Figure 4.8 As in figure 4.2 but for (x,y,z)=(0,1000,10) km.

Reproduced with permission of the copyright owner. Further reproduction prohibited without permission.

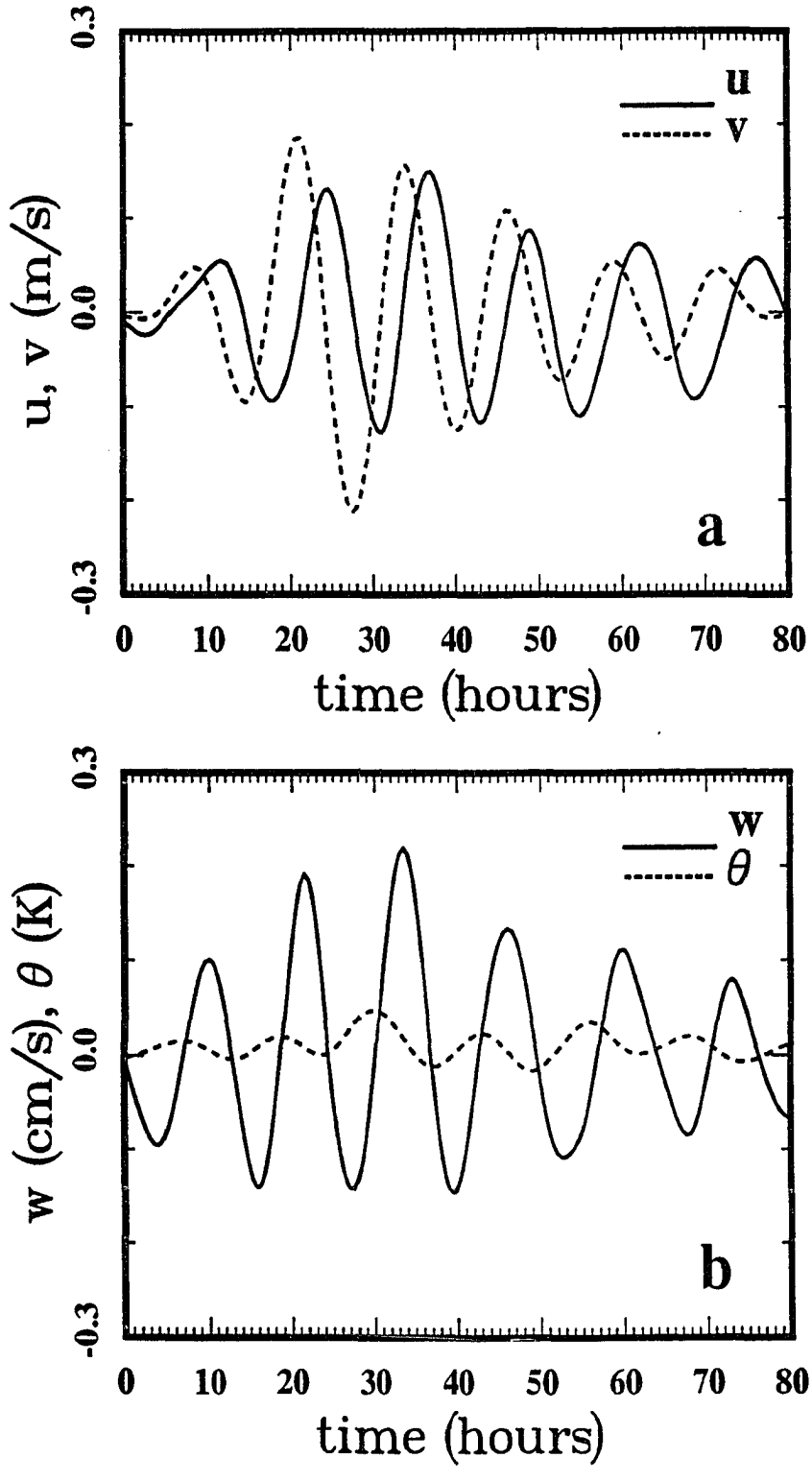

Figure 4.9 As in figure 4.2 but for (x,y,z)=(1000,1000,10) km.

Reproduced with permission of the copyright owner. Further reproduction prohibited without permission.

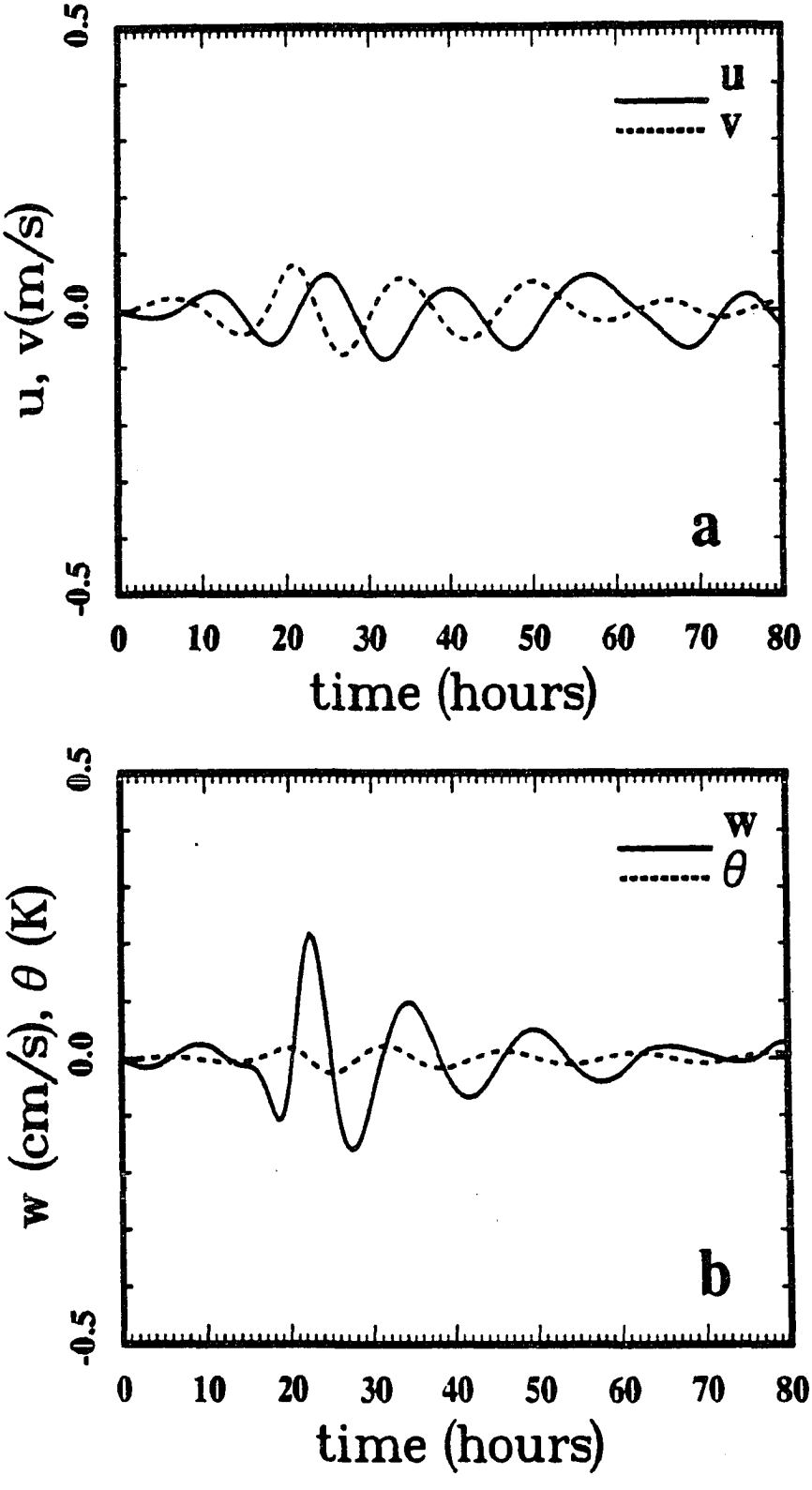

Figure 4.10 As in figure 4.2 but for (x,y,z)=(1000,1000,3) km.

Reproduced with permission of the copyright owner. Further reproduction prohibited without permission.

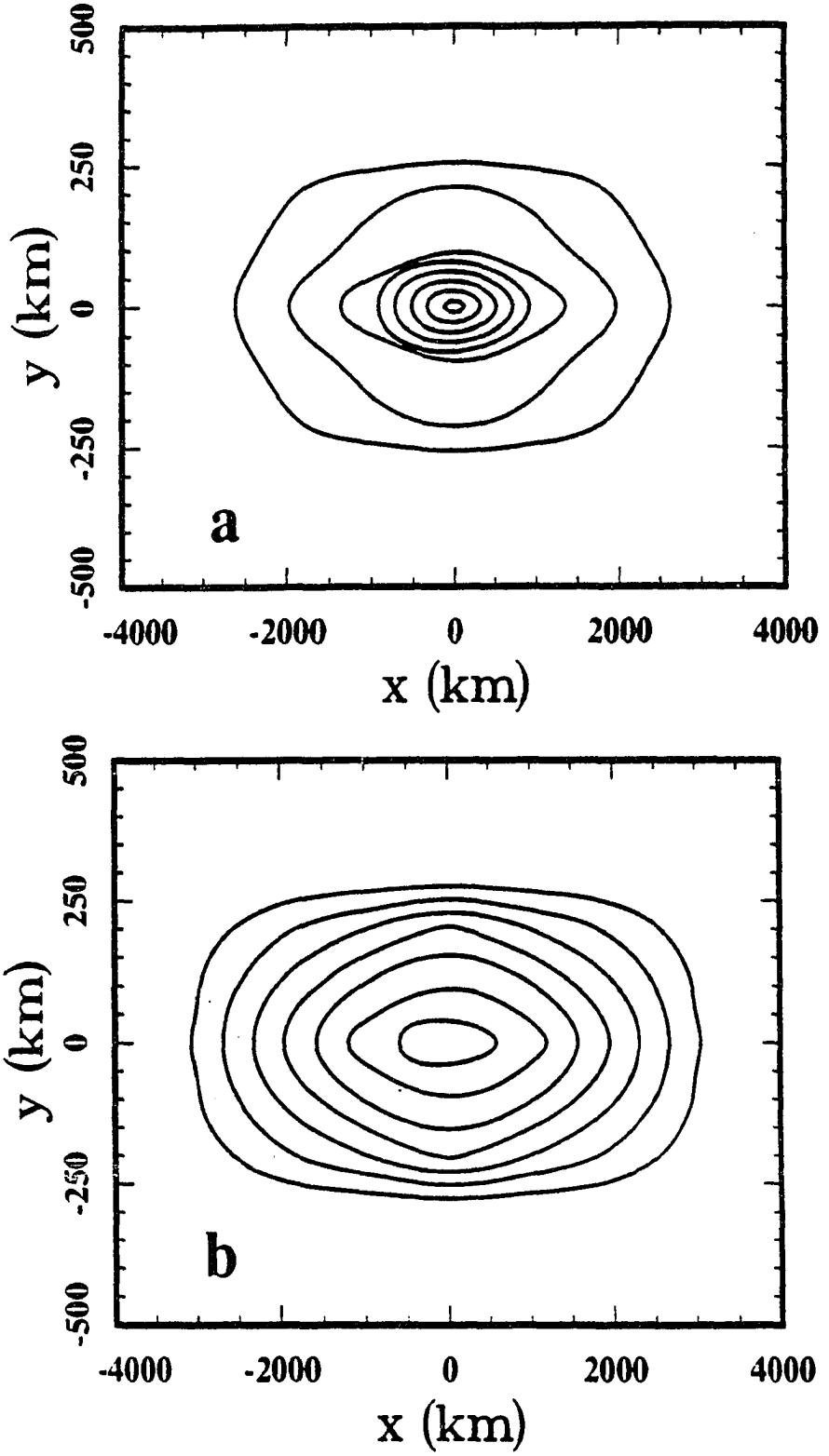

Figure 4.11 An x–y cross section of zonal mean velocity after the adjustment. (a), z=0 km, $\Delta\bar{u}$=0.5m/s; (b),z=1 km, $\Delta\bar{u}$=0.2m/s.

Reproduced with permission of the copyright owner. Further reproduction prohibited without permission.

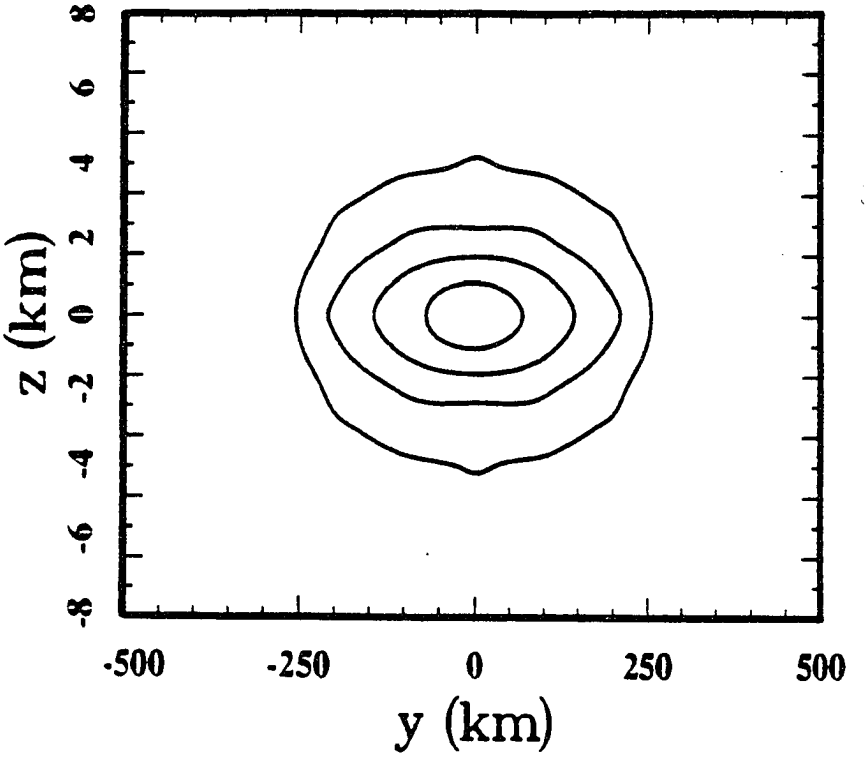

Figure 4.12 As in figure 4.11 but for a y–z cross section at x=2000 km. $\Delta\bar{u}$=0.2m/s.

similar value to the 2–D case (Fig. 3.17(b)), but the induced flow is elongated in the zonal direction. The shape of $\bar{u}$ looks similar to a Gaussian distribution. The slightly uneven contours are due to numerical errors in the velocity estimates and should be ignored. The mean state in the meridional direction (Fig. 4.13) results from the mean zonal convergence in $\bar{u}$ due to the imposed localized initial momentum source. Here $\bar{v}$ is $\sim$ 30–40 times smaller than $\bar{u}$ because of the scales of the gradients in the generated mean zonal structure and of the extent of the return flow. This suggests that a mean meridional velocity comparable to the zonal value arising from such an adjustment would require initial scales of the unbalanced momentum source to be comparable. The $x-z$ cross section (Fig. 4.14) indicates

Reproduced with permission of the copyright owner. Further reproduction prohibited without permission.

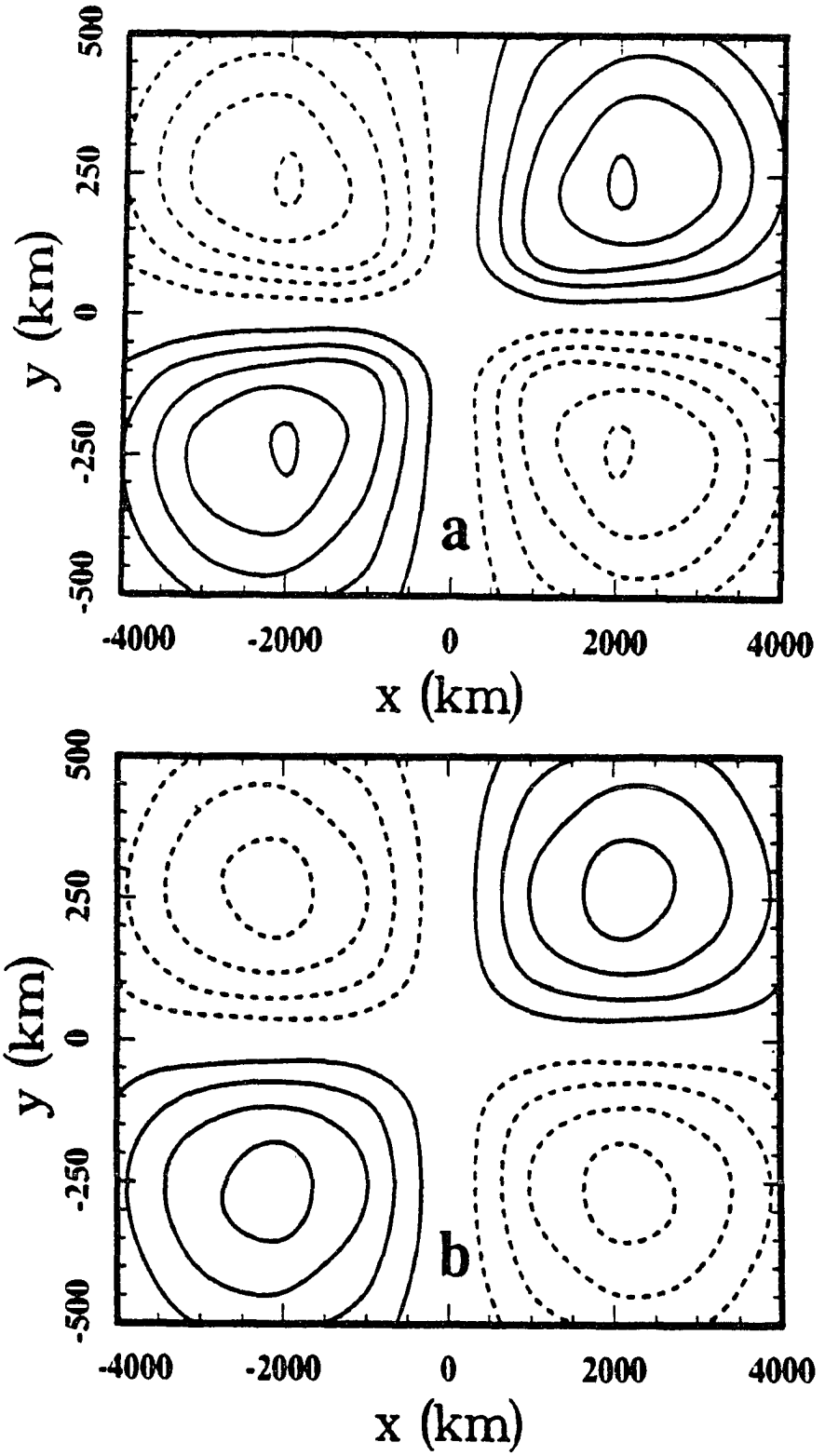

Figure 4.13 As in figure 4.11 but for the meridional component. $\Delta\bar{v}$=2.0cm/s. Note the different units for $\bar{v}$. (a), z=0 km; (b), z=1 km.

Reproduced with permission of the copyright owner. Further reproduction prohibited without permission.

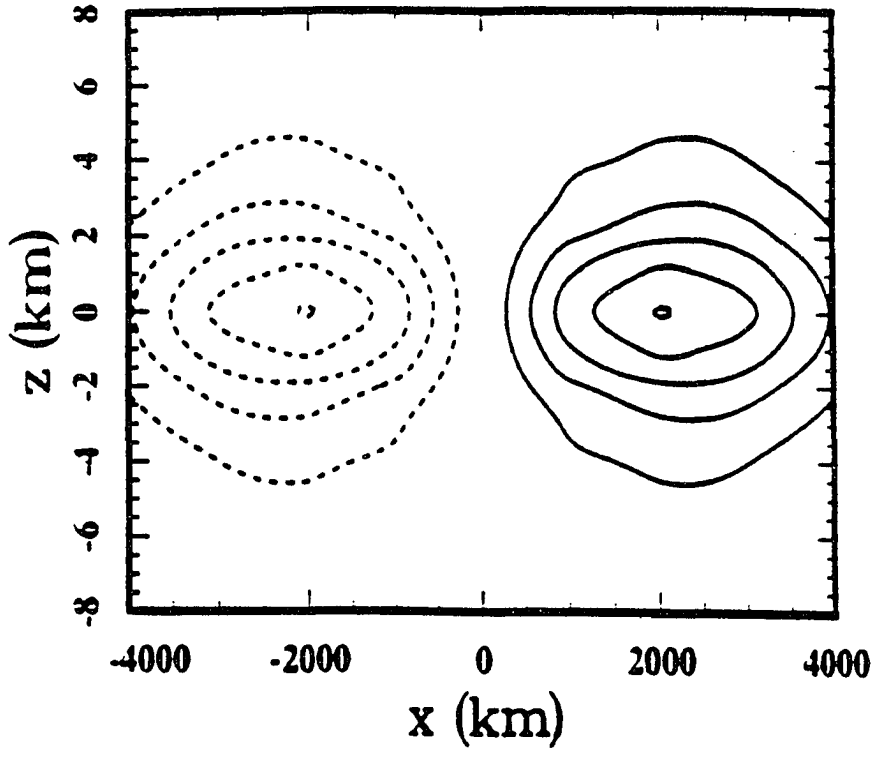

Figure 4.14 As in figure 4.13 but for the x–z cross section. y=200 km, $\Delta\bar{v}$=2.0cm/s.

that the structure of the meridional mean state is also uniform in altitude. The zonal gradients of $\bar{u}$ are observed to be balanced by the meridional gradients of $\bar{v}$, consistent with the continuity equation.

Reproduced with permission of the copyright owner. Further reproduction prohibited without permission.

4.3 Comments on 3–D Adjustment

IGWs induced by the geostrophic adjustment of the atmospheric jet stream have been investigated by specifying an unbalanced shallow Gaussian jet in two and three dimensions which represent infinite and localized jet streams respectively. The radiation of IGWs with frequencies near f and with typical $\sim 6-8$ km vertical wavelengths resulted for jets with $\sigma_z = 1km$ and $\sigma_y = 100km$, and with $\sigma_x = 1000km$ or of infinite zonal extent. The IGWs excited by the adjustment were found to propagate largely or entirely meridionally and to have frequencies and propagation characteristics consistent with the ratios of the initially unbalanced jet scales. The wave fields excited were also found to provide an possible explanation for observations of such motions in association with jet stream flows in the atmosphere.

The full 3–D adjustment results are distinguished from the 2–D results only by the differences between eqs. (3.20) and (4.7) expressing the different responses to infinite and localized momentum sources. Comparing the right hand sides of those two equations with all motions subject to the hydrostatic approximation, it is found that the absence of a zonal gradient in the initial momentum distribution will reduce the 3–D problem to the 2–D results. Thus, the only differences will be how IGWs propagate in the 2–D and 3–D cases. A much larger scale of ageostrophic zonal momentum relative to the meridional thus implies the validity of the 2–D approach and of the 2–D results in this thesis. The large scale of the horizontal ageostrophic component likewise implies the utility of the hydrostatic approximation.

The character of IGWs resulting from a localized jet stream for any particular

Reproduced with permission of the copyright owner. Further reproduction prohibited without permission.

case will depend on the jet structure and the ageostrophic component specified. But we expect the results obtained in this thesis to be widely applicable qualitatively to the interpretation of such observed motions.

Reproduced with permission of the copyright owner. Further reproduction prohibited without permission.

Chapter 5

Conclusions and Discussion

Gravity waves are usually characterized as mesoscale motions even though their horizontal wavelengths can be as large as $\sim 10^3$ kilometers at some sites in the atmosphere. Observational studies have shown that most gravity wave energy occurs at frequencies near f (Balsley and Carter, 1982; Meek *et al.*, 1985) and that these motions are often in association with the jet stream (Stobie *et al.*, 1983; Vincent and Homan, 1983; Bosart and Sanders, 1986; Hirota and Niki, 1986). Of particular relevance to the efforts of this thesis, by analyzing the MU radar data Hirota and Niki (1986) were able to identify gravity wave energy propagating upward in the stratosphere and downward in the troposphere away from an apparent jet stream source. These observations provided the major motivations for this study.

This thesis assumed geostrophic adjustment to be a source mechanism of IGWs and used Fourier integral and Green's function techniques to examine the wave fields radiated by infinite and localized ageostrophic Gaussian jets. For simplicity, motions were assumed to be linear, incompressible and Boussinesq and to occur in a mean flow initially at rest. The dimensions of ageostrophic components embedded in the jets were assumed to have a ratio of 100:1 in the infinite jet case, with an

Reproduced with permission of the copyright owner. Further reproduction prohibited without permission.

axial–to–lateral extent of 10:1 in the case of a localized jet. It is necessary to point out that it is impossible to address every individual jet case through a theoretical study. However, it can be inferred from this particular configuration (and the linear nature of our solutions) that a similar ratio of ageostrophic components initially will result a similar structure among IGWs through the dispersion relations (eqs. 3.13 and 3.19). Both approximate (homogeneous) and full initial–value solutions were obtained for the 2–D problem using Fourier integral techniques. The initial–value solutions approximated well the full wave field solutions for the shallow momentum source in the 2–D problem. IGWs having frequencies near f were found to be the primary wave components excited. Positions far from the jet axis exhibited meridional IGW propagation most clearly. Wave packets of moderate amplitude propagated upward and downward, with IGW phases moving downward and upward above and below the jet core. Energy was seen to be transported along shallow paths with angles of $\sim tan^{-1}(1/100)$ from the horizontal due to the scales present in the initially unbalanced momentum source. IGWs propagated outward from the jet source with higher frequency motions following steeper paths and propagating more rapidly than lower frequencies. Horizontal motions were symmetric and the vertical motion and temperature fields were antisymmetric about the jet axes in the wave fields for the 2–D case because of the symmetric structure of the Gaussian momentum source.

Wave field solutions of the full initial–value problem differ only slightly from the approximate solutions due to the evolution of a weak balanced mean jet structure. This surviving mean jet had an amplitude $\sim$ 40% of the initial forcing and was slightly elongated in the vertical relative to initially unbalanced jet structure. The

Reproduced with permission of the copyright owner. Further reproduction prohibited without permission.

adjustment time for this baroclinic geostrophic adjustment process was $\sim 2-3T_i$ instead of a few hours in a barotropic adjustment process owing to the group velocity differences between internal and external gravity waves. The hydrostatic approximation was found to yield accurate solutions because of the low–frequency nature of the motion field, and Fourier integral solutions were validated with those obtained using Green's function techniques.

Results obtained with a localized unbalanced Gaussian jet differed from those obtained for an infinite jet by permitting some wave propagation in the zonal direction, but with the major wave field structure qualitatively like that of the 2–D solution and reducing to the 2–D results as $\sigma_x \rightarrow \infty$. For this chosen jet structure, the correction terms defined by the part 2 solutions in chapter 4 (except the zonal motion) result in amplitude and phase changes between components in a manner that reduces meridionally propagating motions and introduces significant zonal propagation at large axial displacements from the jet core. It should also be noted that the differences between the 2–D and 3–D results are likely to be even greater if the zonal and meridional scales of the initially unbalanced source structure are more nearly comparable.

The results found in this thesis represent a first attempt to understand the wave fields excited by geostrophic adjustment associated with the atmospheric jet streams. There are many ways in which the problem could be made more realistic. First, temporal morphology of the source could include a more general departure from balanced flow conditions. A delta function in the time domain imposes the unbalanced momentum in an infinitely short time. On the other hand, solutions can be derived using Fourier transform or Green's function techniques for $f(t)$ any

Reproduced with permission of the copyright owner. Further reproduction prohibited without permission.

function of time. Second, these results would be more realistic if the background atmosphere included a mean balanced jet structure. A uniform background motion can be solved most simply by introducing Galilean transformation (eq. 2.4). But a more realistic background velocity field would lead to very much more complexity in the mathematical expression of the solution. Third, the β effect could be included. The early studies of the influence of inertial motions with $\beta \neq 0$ were performed for the oceans (Munk and Phillips, 1968). Geisler and Dickinson (1972) employed a 2–D model to examine the β effect of IGWs during the wave propagation due to a geostrophic adjustment process in the ocean by expressing f as a constant reference value plus a linear poleward gradient (a β–plane model) and noted that waves travelling to the north are reflected at the latitude where their frequency is equal to the Coriolis parameter. A final issue that may affect wave excitation by geostrophic adjustment is nonlinearity. Although many of the observed features of IGWs around a jet stream may be described well by linear theory, nonlinearity may be important in strong source regions where amplitudes may be relatively large. Also the nonlinear investigation might help us to understand the excitation process of the initial unbalance in the atmospheric jet streams.

Reproduced with permission of the copyright owner. Further reproduction prohibited without permission.

Appendix A

IGW Generators of Geostrophic Adjustment

The full set of equations describing geostrophic adjustment of the atmospheric jet stream in an incompressible, adiabatic and inviscid fluid may be written as

$$\frac{\partial u}{\partial t} + u\frac{\partial u}{\partial x} + v\frac{\partial u}{\partial y} + w\frac{\partial u}{\partial z} + \frac{1}{\rho}\frac{\partial p}{\partial x} - fv = \eta F_x \delta(t), \tag{A.1}$$

$$\frac{\partial v}{\partial t} + u\frac{\partial v}{\partial x} + v\frac{\partial v}{\partial y} + w\frac{\partial v}{\partial z} + \frac{1}{\rho}\frac{\partial p}{\partial y} + fu = 0, \tag{A.2}$$

$$\varepsilon_h\left(\frac{\partial w}{\partial t} + u\frac{\partial w}{\partial x} + v\frac{\partial w}{\partial y} + w\frac{\partial w}{\partial z}\right) + \frac{1}{\rho}\frac{\partial p}{\partial z} + g = 0, \tag{A.3}$$

$$\varepsilon_c\left(\frac{\partial \rho}{\partial t} + u\frac{\partial \rho}{\partial x} + v\frac{\partial \rho}{\partial y} + w\frac{\partial \rho}{\partial z}\right) + \rho\left(\frac{\partial u}{\partial x} + \frac{\partial v}{\partial y} + \frac{\partial w}{\partial z}\right) = 0, \tag{A.4}$$

$$\frac{\partial \theta}{\partial t} + u\frac{\partial \theta}{\partial x} + v\frac{\partial \theta}{\partial y} + w\frac{\partial \theta}{\partial z} = 0, \tag{A.5}$$

$$\rho = \frac{p}{RT}, \tag{A.6}$$

where u, v, w, ρ, p, and θ denote zonal, meridional, and vertical components of velocity, density, pressure and potential temperature, δ here is Dirac delta function. R is gas constant, and $f = 2\Omega sin(\phi)$ is the Coriolis term. Here η, ε_h and ε_c are switch constants representing a nonhomogeneous forcing (referred to as the full initial–value problem in this thesis), and nonhydrostatic and compressible effects with values of unity. With these quantities zero, the initial value (referred as the

Reproduced with permission of the copyright owner. Further reproduction prohibited without permission.

approximate solution), hydrostatic and incompressible problem is obtained. The quantity F_x denotes the spatial form of the initial momentum distribution.

Employing linearized theory and the Boussinesq approximation and omitting the primes, eqs. (A.1)–(A.6) in a motionless background become

$$\frac{\partial u}{\partial t} + \frac{1}{\rho_0}\frac{\partial p}{\partial x} - fv = \eta F_x \delta(t), \tag{A.7}$$

$$\frac{\partial v}{\partial t} + \frac{1}{\rho_0}\frac{\partial p}{\partial y} + fu = 0, \tag{A.8}$$

$$\varepsilon_h \frac{\partial w}{\partial t} + \frac{1}{\rho_0}\frac{\partial p}{\partial z} - \frac{g}{\bar{\theta}}\theta = 0, \tag{A.9}$$

$$\frac{\partial u}{\partial x} + \frac{\partial v}{\partial y} + \frac{\partial w}{\partial z} = 0, \tag{A.10}$$

$$\frac{\partial \theta}{\partial t} + \frac{\bar{\theta}}{g} N^2 w = 0, \tag{A.11}$$

where $N^2 = (g/\bar{\theta})d\bar{\theta}/dz$ is the square of the buoyancy (Brunt–Väisälä) frequency. An overbar denotes mean quantities and ρ_0 is a reference density chosen as constant.

Combining eqs. (A.9) and (A.11) to eliminate θ yields

$$[(\varepsilon_h \frac{\partial^2}{\partial t^2} + N^2)]w = -\frac{1}{\rho_0}\frac{\partial^2 p}{\partial t \partial z}, \tag{A.12}$$

Taking the curl of the horizontal momentum equations, *i.e.* $\partial(A.7)/\partial y - \partial(A.8)/\partial x$, we obtain,

$$(\frac{\partial^2}{\partial t \partial y} - f\frac{\partial}{\partial x})u - (\frac{\partial^2}{\partial t \partial x} + f\frac{\partial}{\partial y})v = \eta \frac{\partial F_x}{\partial y}\delta(t). \tag{A.13}$$

Then using $\partial(A.12)/\partial y$ and $\partial^2(A.8)/\partial t \partial z$ to eliminate p and eq. (A.10) to eliminate w yield

$$[f\frac{\partial^3}{\partial t \partial z^2} + \frac{\partial^2}{\partial x \partial y}(\varepsilon_h \frac{\partial^2}{\partial t^2} + N^2)]u + [\frac{\partial^4}{\partial t^2 \partial z^2} + \frac{\partial^2}{\partial y^2}(\varepsilon_h \frac{\partial^2}{\partial t^2} + N^2)]v = 0. \tag{A.14}$$

Reproduced with permission of the copyright owner. Further reproduction prohibited without permission.

From eqs. (A.13) and (A.14) one obtains

$$\frac{\partial}{\partial t}[(\frac{\partial^2}{\partial t^2}+f^2)\frac{\partial^2}{\partial z^2} + (\varepsilon_h\frac{\partial^2}{\partial t^2}+N^2)\Delta_2]u = [\frac{\partial^4}{\partial t^2\partial z^2}+\frac{\partial^2}{\partial y^2}(\varepsilon_h\frac{\partial^2}{\partial t^2}+N^2)]\eta F_x\delta(t), \quad \text{(A.15)}$$

and

$$\frac{\partial}{\partial t}[(\frac{\partial^2}{\partial t^2}+f^2)\frac{\partial^2}{\partial z^2} + (\varepsilon_h\frac{\partial^2}{\partial t^2}+N^2)\Delta_2]v = -[f\frac{\partial^3}{\partial t\partial z^2}+\frac{\partial^2}{\partial x\partial y}(\varepsilon_h\frac{\partial^2}{\partial t^2}+N^2)]\eta F_x\delta(t), \quad \text{(A.16)}$$

where $\Delta_2 = \partial^2/\partial x^2+\partial^2/\partial y^2$ is the horizontal 2–D Laplacian operator. Now taking the divergence of the horizontal momentum equations, *i.e.*, $\partial(A.7)/\partial x+\partial(A.8)/\partial y$, and using eq. (A.10), yields

$$-\frac{\partial^2 w}{\partial t\partial z}-f(\frac{\partial v}{\partial x}-\frac{\partial u}{\partial y})+\frac{1}{\rho_0}\Delta_2 p = \eta\frac{\partial F_x}{\partial x}\delta(t). \quad \text{(A.17)}$$

Thus taking $\partial(A.17)/\partial t$, using $\partial(A.7)/\partial y, \partial(A.8)/\partial x$ and eq. (A.10) to eliminate u and v, and applying eq. (A.12) to substitute for p, one obtains

$$(\frac{\partial^2}{\partial t^2}+f^2)\frac{\partial^2}{\partial z^2}+(\varepsilon_h\frac{\partial^2}{\partial t^2}+N^2)\Delta_2 w = (f\frac{\partial}{\partial y}-\frac{\partial^2}{\partial t\partial x})\eta\frac{\partial F_x}{\partial z}\delta(t). \quad \text{(A.18)}$$

Eq. (A.18) together with eq. (A.11) yields

$$\frac{\partial}{\partial t}[(\frac{\partial^2}{\partial t^2}+f^2)\frac{\partial^2}{\partial z^2} + (\varepsilon_h\frac{\partial^2}{\partial t^2}+N^2)\Delta_2]\theta = -\frac{\bar{\theta}N^2}{g}(f\frac{\partial}{\partial y}-\frac{\partial^2}{\partial t\partial x})\eta\frac{\partial F_x}{\partial z}\delta(t). \quad \text{(A.19)}$$

Finally, combining eqs. (A.15), (A.16), (A.18) and (A.19) gives

Reproduced with permission of the copyright owner. Further reproduction prohibited without permission.

$$\begin{pmatrix} L_1 u \\ L_1 v \\ L_2 w \\ L_1 \theta \end{pmatrix} = \eta \begin{pmatrix} (\varepsilon_h M_{yy} + M_{zz})\delta''(t) & +N^2 M_{yy}\delta(t) \\ -[\varepsilon_h M_{xy}\delta''(t) + f M_{zz}\delta'(t)] & -N^2 M_{xy}\delta(t) \\ f M_{yz}\delta(t) & -M_{xz}\delta'(t) \\ -\frac{f\bar{\theta}N^2}{g} M_{yz}\delta(t) & +\frac{\bar{\theta}N^2}{g} M_{xz}\delta'(t) \end{pmatrix}, \qquad \text{(A.20)}$$

Part 1 *Part 2*

where

$$L_1 = \frac{\partial}{\partial t}[(\frac{\partial^2}{\partial t^2} + f^2)\frac{\partial^2}{\partial z^2} + (\varepsilon_h \frac{\partial^2}{\partial t^2} + N^2)\Delta_2], \qquad \text{(A.21)}$$

and

$$L_2 = (\frac{\partial^2}{\partial t^2} + f^2)\frac{\partial^2}{\partial z^2} + (\varepsilon_h \frac{\partial^2}{\partial t^2} + N^2)\Delta_2, \qquad \text{(A.22)}$$

$M_{zz} = \partial^2 F_x/\partial z^2, M_{yy} = \partial^2 F_x/\partial y^2$, $M_{xy} = \partial^2 F_x/\partial x \partial y, M_{yz} = \partial^2 F_x/\partial y \partial z$, and $M_{xz} = \partial^2 F_x/\partial x \partial z$.

Reproduced with permission of the copyright owner. Further reproduction prohibited without permission.

Appendix B

Green's Function Solutions for 3–D IGW Generators

This derivation concerns only the hydrostatic case. First applying the Laplace transform defined by

$$\tilde{\varphi} = \int_0^{+\infty} \varphi e^{-\sigma t}, \qquad \sigma > 0, \tag{B.1}$$

in the time domain to eq. (4.7), substituting for z with

$$z = \sqrt{\frac{\sigma^2 + f^2}{N^2}}\mu, \tag{B.2}$$

using the properties of the $\delta-$function (remember our at rest initial conditions), the equation for the Green's functions is obtained

$$L_G \begin{pmatrix} \tilde{G}_u \\ \tilde{G}_v \\ \tilde{G}_w \\ \tilde{G}_\theta \end{pmatrix} = -\frac{\delta(x)\delta(y)\delta(\mu)}{N\sqrt{\sigma^2+f^2}} \begin{pmatrix} \sigma & +\frac{N^2}{\sigma} \\ -f & -\frac{N^2}{\sigma} \\ f & -\sigma \\ -\frac{f\bar{\theta}N^2}{g\sigma} & +\frac{\bar{\theta}N^2}{g} \end{pmatrix}, \tag{B.3}$$

where

$$L_G = \Delta_2 + \frac{\partial^2}{\partial \mu^2}. \tag{B.4}$$

The tilde here denotes a Laplace transform and G_u is the Green's function for u, *etc.*

Reproduced with permission of the copyright owner. Further reproduction prohibited without permission.

Eq. (B.3) is solved in free space (Butkovskiy,1982) but is rewritten as

$$\begin{pmatrix} \tilde{G}_u \\ \tilde{G}_v \\ \tilde{G}_w \\ \tilde{G}_\theta \end{pmatrix} = \frac{1}{4\pi N\sqrt{\hat{x}^2+\hat{y}^2}\sqrt{\sigma^2+a^2}} \begin{pmatrix} \sigma & +\frac{N^2}{\sigma} \\ -f & -\frac{N^2}{\sigma} \\ f & -\sigma \\ -\frac{f\bar{\theta}N^2}{g\sigma} & +\frac{\bar{\theta}N^2}{g} \end{pmatrix}, \tag{B.5}$$

where $\hat{x} = x - \lambda; \hat{y} = y - \xi; \hat{z} = z - \zeta$; and $a^2 = f^2 + N^2\hat{z}^2/(\hat{x}^2+\hat{y}^2)$ Therefore, the Green's functions in the time domain are (Oberhettinger,1973; Spanier,1987)

$$\begin{aligned} G_u(x,y,z,t;\lambda,\xi,\zeta) &\equiv G_u^{(1)} + G_u^{(2)} \\ &= -\frac{aJ_1(at)}{4\pi N\sqrt{\hat{x}^2+\hat{y}^2}} + \frac{Nt}{8\sqrt{\hat{x}^2+\hat{y}^2}} \\ &\quad \cdot\{J_0(at)[\frac{2}{\pi} - H_1(at)] + J_1(at)H_0(at)\}, \end{aligned} \tag{B.6}$$

$$\begin{aligned} G_v(x,y,z,t;\lambda,\xi,\zeta) &\equiv G_v^{(1)} + G_v^{(2)} \\ &= -\frac{fJ_0(at)}{4\pi N\sqrt{\hat{x}^2+\hat{y}^2}} - \frac{Nt}{8\sqrt{\hat{x}^2+\hat{y}^2}} \\ &\quad \cdot\{J_0(at)[\frac{2}{\pi} - H_1(at)] + J_1(at)H_0(at)\}, \end{aligned} \tag{B.7}$$

$$G_w(x,y,z,t;\lambda,\xi,\zeta) \equiv G_w^{(1)} + G_w^{(2)} = \frac{fJ_0(at)}{4\pi N\sqrt{\hat{x}^2+\hat{y}^2}} + \frac{aJ_1(at)}{4\pi N\sqrt{\hat{x}^2+\hat{y}^2}}, \tag{B.8}$$

and

$$G_\theta(x,y,z,t;\lambda,\xi,\zeta) \equiv G_\theta^{(1)} + G_\theta^{(2)} =$$

$$-\frac{f\bar{\theta}Nt}{8g\sqrt{\hat{x}^2+\hat{y}^2}}\{J_0(at)[\frac{2}{\pi} - H_1(at)] + J_1(at)H_0(at)\} + \frac{\bar{\theta}NJ_0(at)}{4\pi g\sqrt{\hat{x}^2+\hat{y}^2}}. \tag{B.9}$$

where J and H are Bessel and Struve's functions.

The final solutions are given by

$$u = \int\int_V \int [G_u^{(1)} M_{zz}(\lambda,\xi,\zeta) + G_u^{(2)} M_{yy}(\lambda,\xi,\zeta)]d\lambda d\xi d\zeta, \tag{B.10}$$

$$v = \int\int_V \int [G_v^{(1)} M_{zz}(\lambda,\xi,\zeta) + G_v^{(2)} M_{xy}(\lambda,\xi,\zeta)]d\lambda d\xi d\zeta, \tag{B.11}$$

Reproduced with permission of the copyright owner. Further reproduction prohibited without permission.

$$w = \int\int\int_V [G_w^{(1)} M_{yz}(\lambda, \xi, \zeta) + G_w^{(2)} M_{xz}(\lambda, \xi, \zeta)] d\lambda d\xi d\zeta, \tag{B.12}$$

and

$$\theta = \int\int\int_V [G_\theta^{(1)} M_{yz}(\lambda, \xi, \zeta) + G_\theta^{(2)} M_{xz}(\lambda, \xi, \zeta)] d\lambda d\xi d\zeta. \tag{B.13}$$

where V is an unbounded 3–D domain.

Reproduced with permission of the copyright owner. Further reproduction prohibited without permission.

References

Balsley, B. B., and D. A. Carter, 1982: The spectrum of atmospheric velocity fluctuations at 8 and 86 km, *Geophys. Res. Lett.*, **9**, 465–468.

Blumen, W., 1972: Geostrophic adjustment, *Rev. Geophys. Space Phys.*, **10**, 485–528.

Bosart, L. F., and F. Sanders, 1986: Mesoscale structure in the megalopolitan snowstorm of 11–12 February 1983, Part III: A large–amplitude gravity wave, *J. Atmos. Sci.*, **43**, 924–939.

Butkovskiy, A. G., 1982: Green's functions and transfer functions handbook, Ellis Horwood Ltd., 236pp.

Cahn, A., 1945: An investigation of the free oscillations of a simple current system, *J. Meteorol.*, **2**, 113–119.

Cammas, J., and D. Raymond, 1989: Analysis and diagnosis of the composition of ageostrophic circulations in jet–front system, *Mon. Wea. Rev.*, **117**, 2447–2462.

Charney, J., 1955: The use of the primitive equations of motion in numerical prediction, *Tellus*, **7**, 22–26.

Chimonas, G., 1970: Internal gravity-wave motions induced in the earth's atmosphere by a solar eclipse, *J. Geophys. Res.*, **75**, 5545-5551.

Chimonas, G., and C. O. Hines, 1970: Atmospheric gravity waves launched by auroral currents, *Planet. Space Sci.*, **18**, 565-589.

Chimonas, G., and J. R. Grant, 1984: Shear excitation of gravity waves. Part II: Upscale scatting from Kelvin–Helmholtz waves, *J. Atmos. Sci.*, **41**, 2278–2288.

Reproduced with permission of the copyright owner. Further reproduction prohibited without permission.

Clark, T. E., T. Hauf and J. P. Kuettner, 1986: Convectively forced internal gravity waves: Results from two-dimensional numerical experiments, *Quart. J. Roy. Meteorol. Soc.*, **112**, 899–925.

Danielsen, E. F., R. S. Hipskind, W. L. Starr, J. F. Vedder, S. E. Gaines, D. Kley and K. K. Kelly, 1991: Irreversible transport in the stratosphere by internal waves of short vertical wavelength, *J. Geophys. Res.*, in press.

Davis, M. J. and A. V. Da Rosa, 1970: Possible detection of atmospheric gravity waves generated by the solar eclipse, *Nature*, **226**, 1123.

Dickinson, R. E., 1969*a*: Propagations of atmospheric motions. 1. Excitation by point impulses, *Rev. Geophys.*, **7**, 483–514.

Dickinson, R. E., 1969*b*: Propagations of atmospheric motions. 2. Excitation by switch–on sources, *Rev. Geophys.*, **7**, 515–538.

Dong, B. and K. C. Yeh, 1988: Resonant and nonresonant wave-wave interactions in an isothermal atmosphere, *J. Geophys. Res.*, **93**, 3729-3744.

Duffy, D. G., 1990:Geostrophic adjustment in a baroclinic atmosphere., *J. Atmos. Sci.*, **47**, 457–473.

Dunkerton, T., 1989: Theory of internal gravity wave saturation, *Pure Appl. Geophys.*, **130**, 373–397.

Eady, E. T., 1949: Long waves and cyclone waves, *Tellus*, **1**, 33–52.

Einaudi, F., W. L. Clark, D. Fua, J. L. Green and T. E. VanZandt, 1987: Gravity waves and convection in Colorado during July 1983, *J. Atmos. Sci.*, 44, 1534–1553.

Eom, J. K., 1975: Analysis of the internal gravity wave occurrence of 19 April 1970 in the Midwest , *Mon. Wea. Rev.*, **103**, 217–226.

Fritts, D. C., 1982: Shear excitation of atmospheric gravity wave, *J. Atmos. Sci.*, **39**, 1936–1952.

Fritts, D. C., 1984*a*: Gravity wave saturation in the middle atmosphere: A review of theory

Reproduced with permission of the copyright owner. Further reproduction prohibited without permission.

and observations, *Rev. Geophys. Space Phys..*, **22**, 275–308.

Fritts, D. C., 1984*b*: Shear excitation of atmospheric gravity waves. Part II: nonlinear radiation from a free shear layer, *J. Atmos. Sci.*, **41**, 524–531.

Fritts, D. C., 1989: A review of gravity wave saturation processes, effects, and variability in the middle atmosphere , *Pure Appl. Geophys.*, **130**, 343–371.

Fritts, D. C., and G. D. Nastrom, 1991: Sources of mesoscale variability of gravity waves, II: Frontal, convective and jet stream excitation, Submitted to *J. Atmos. Sci.*.

Fritts, D. C., and T. J. Dunkerton, 1985: Fluxes of heat and constituents due to convectively unstable gravity waves , *J. Atmos. Sci.*, **42**, 549–556.

Gall R. L., R. T.Williams and T. L. Clark, 1988: Gravity waves generated during frontogenesis, *J. Atmos. Sci.*, **45**, 2204–2219.

Geisler, J. E. and R. E. Dickinson, 1972: The role of variable Coriolis parameter in the propagation of inertia–gravity waves during the process of geostrophic adjustment, *J. Phys.. Oceanogr.*, **2**, 263-272.

Gossard, E. E., 1962: Vertical flux of energy into the lower ionosphere from internal gravity waves generated in the troposphere. , *J. Geophys. Res.*, **67**, 745-757.

Gossard, E. E., and W. H. Hooke, 1975: Waves in the atmosphere, Elsevier Sci. Pub. Co., 456 pp.

Hauf, T. and T. L. Clark, 1989: Three–dimensional numerical experiment on convectively forced internal gravity waves, *Quart. J. Roy. Meteorol. Soc.*, **115**, 309–333.

Hines, C. O., 1960: Internal atmospheric gravity waves at ionospheric heights, *Can. J. Phys..*, **38**, 1441-1481.

Hines, C. O., 1988: A modeling of atmospheric gravity waves and wave generated by isotropic and anisotropic terrain, *J. Atmos. Sci.*, **45**, 309–322.

Hines, C. O., and Colleagues, 1974: The upper atmosphere in motion, Amer. Geophys. Union, 1027pp.

Reproduced with permission of the copyright owner. Further reproduction prohibited without permission.

Hirota, I. and T. Niki, 1986: Inertia–gravity waves in the troposphere and stratosphere observed by the MU radar, *J. Meteorol. Soc. Japan*, **64**, 995–999.

Holton, J. R., 1982: The role of gravity wave induced drag and diffusion in the momentum budget of the mesosphere, *J. Atmos. Sci.*, **39**, 791-799.

Holton, J. R., and X. Zhu, 1984: A further study of gravity waves induced drag and diffusion in the mesosphere, *J. Atmos. Sci.* , **41**, 2653-2662.

Hooke, W. H., 1986: Gravity waves, in Mesoscale meteorology and forecasting, P. S. Ray edited, Amer. Meteorol. Soc., 793pp.

Hoskins, B. J., 1975: The geostrophic momentum approximation and the semi–geostrophic equations, *J. Atmos. Sci.*, **32**, 233–242.

Jasperson, W. h., G. D. Nastrom, and D. C. Fritts, 1990: Further study of terrain effects on the mesoscale spectrum of atmospheric motions, *J. Atmos. Sci.*, **47**, 979–987.

Kundu, P. K., 1990: Fluid mechanics, Acad. Press, 638pp.

Kung, E. C. and H. L. Tanaka, 1983: Energetics analysis of the global circulation during the special observation period of FGGE , *J. Atmos. Sci.*, **40**, 2575–2592.

Kwon, K. H., D. C. Senft, and C. S. Gardner, 1990: Airborne sodium lidar observations of horizontal and vertical wavenumber spectra of mesopause density and wind perturbations , *J. Geophys. Res.*, **95**, 13723–13736.

Lalas, D. P. and F. Einaudi, 1976: On characteristics of gravity waves generated by atmospheric shear layers, *J. Atmos. Sci.*, **33**, 1248–1259.

Lee, C. Y. and R. C. Beardsley, 1974: The generation of long nonlinear internal waves in a weakly stratified shear flow, *J. Geophys. Res.*, **79**, 453–462.

Ley, B. E. and W. R. Peltier, 1978: Wave generation and frontal collapse, *J. Atmos. Sci.*, **35**, 3–17.

Lighthill, M. J., 1964: Group velocity, *J. Inst. math. Appl.*, **1**, 1–28.

Lilly, D. K. and P. J. Kennedy, 1973: Observations of a stationary mountain wave and its

Reproduced with permission of the copyright owner. Further reproduction prohibited without permission.

associated momentum flux and energy dissipation, *J. Atmos.Sci.*, **30**, 1135–1152.

Lindzen, R. S., 1981: Turbulence and stress due to gravity wave and tidal breakdown, *J. Geophys. Res.*, **86**, 9707-9714.

Lu, D., T.E.VanZandt and W.L.Clark, 1984: VHF Doppler radar observations of buoyancy waves included by thunderstorms, *J. Atmos. Sci.*, **41**, 272–282.

Mastrantonio, G. F., F. Einaudi, D. Fua and D. P. Lalas, 1976: Generation of gravity waves by jet streams in the atmosphere, *J. Atmos. Sci.*, **33**, 1730–1738.

McFarlane, N. A., 1987: The effect of orographically excited gravity wave drag on the general circulation of the lower stratosphere and troposphere, *J. Atmos.Sci.*, **44**, 1775–1800.

Meek, C. E., I. M. Reid and A. H. Manson, 1985: Observations of mesospheric wind velocities. II. Cross sections of power spectral density for 48–8 h, 8–1 h, 1 h–10 min over 60–110 km for 1981, *Radio Sci.*, **20**, 1383–1402.

Middleton, J. F., 1986: Energetics of linear geostrophic adjustment, *J. Phys.. Oceanogr.*, **17**, 735-740.

Munk, W. and N. Phillips, 1968: Coherence and band structure of the inertial motion in the sea, *Rev. Geophys. Space Phys..*, **6**, 447-472.

Nastrom, G. D. and D. C. Fritts, 1991: Source of mesoscale variability of gravity waves,I: Topographic excitation. Submitted to *J. Atmos. Sci.*.

Nastrom, G. D., D. C. Fritts and K. S. Gage, 1987: An investigation of terrain effects on the mesoscale spectrum of atmospheric motions, *J.Atmos.Sci.*, **44**, 3087–3096.

Oberhettinger, F., 1973: Tables of Laplace Transforms, Springer–Verlag, 428pp.

Obukhov, A. M., 1949: On the question of the geostrophic wind (in Russian), *Izv. Akad. Nauk SSSR Ser. Geograf.-Geofiz.*, **13**, 281–306.

Parker, S. P. 1987: Meteorological source book, McGraw–Hill Book Co., 304pp.

Pfister, L., W. Starr, R. Craig, M. Leowenstein and M. Legg, 1986: Small scale motions

Reproduced with permission of the copyright owner. Further reproduction prohibited without permission.

observed by aircraft in the tropical lower stratosphere: Evidence for mixing and its relationship to large scale flow, *J. Atmos. Sci.*, **43**, 3210–3225.

Phillips, N. A., 1963: Geostrophic motion, *Rev. Geophys.*, **1**, 123–176.

Phillips, N. A., W. Blumen and O. Cote, 1960: Numerical weather prediction in the Soviet Union , *Bull. Amer. Meteorol. Sco.*, 41, 599–617.

Richmond, A. D., 1978: Gravity wave generation, Propagation, and dissipation in the thermosphere, *J. Geophys. Res.*, **83**, 4131-4145.

Rind, D., R. Suozzo, N. K. Balachandran, A. Lacis and G. Russell, 1988: The GISS global climate-middle atmosphere model. Part I: Model structure and climatology, *J. Atmos. Sci.*, **45**, 329-370.

Rossby, C. G., 1938: On the mutual adjustment of pressure and velocity distributions in certain simple current systems, 2, *J. Mar. Res.*, **1**, 239–263.

Schubert, W. H., J. I. Hack, P. L. Silva Dias and S. R. Fulton, 1980: Geostrophic adjustment of an axisymmetric vortex, *J. Atmos. Sci.*, **37**, 1464–1484.

Smith, R. B., 1985: On severe downslope winds, *J. Atmos. Sci.*, **42**, 2597–2603.

Spanier, J., and K. B. Oldham, 1987: An atlas of functions, Hemisphere Pub. Co., 700pp.

Stobie, J. G., F. Einaudi and L. W. Uccellin, 1983: A case study of gravity waves–convective storms interaction: 9 May 1979, *J. Atmos. Sci.*, **40**, 2804–2830.

Stone, P. H., 1966: On non–geostrophic baroclinic instability, *J. Atmos. Sci.*, **23**, 239–400.

Stone, P. H., 1978: Baroclinic adjustment, *J. Atmos. Sci.*, **35**, 561–571.

Tanaka, H. L., and S. Sun, 1990: A study of baroclinic energy sources for large–scale atmospheric normal modes, *J. Atmos. Sci.*, **47**, 2674–2695.

Uccellini, L. W., 1975: A case study of apparent gravity wave initiation of severe convective storms, *Mon. Wea. Rev.*, **103**, 497–513.

Uccellini, L. W., and P. J. Kocin, 1987: The interaction of jet stream circulations during heavy snow events along the east coast of the United states, *Wea. Forecasting*, **2**,

Reproduced with permission of the copyright owner. Further reproduction prohibited without permission.

289–308.

Uccellini, L. W., , R. A. Petersen, C. H. Wash and K. F. Brill, 1984: The President's day cyclone of 18–19 February 1979: Synoptic overview and analysis of the subtropical jet streak influencing the precyclogenetic period, *Mon. Wea. Rev.*, **112**, 31–55.

Uccellini, L. W., and S. E. Koch, 1987: The synoptic setting and possible energy sources for mesoscale wave disturbances, *Mon. Wea. Rev.*, **115**, 721–729.

Van Tuyl, A. H. and J. A. Young, 1982: Numerical simulation of nonlinear jet streak adjustment, *Mon. Wea. Rev.*, **110**, 2038–2054.

Veronis, G., 1956: Partition of energy between geostrophic and non–geostrophic oceanic motion, *Deep Sea Res.*, **3**, 157–177.

Vincent, D. G. and J. H. Homan, 1983: Mesoscale analysis of pressure and precipitation patterns during AVE–SESAME 1979, 10–11 April, *Bull. Amer. Meteorol. Soc.*, **64**, 23–28.

Vincent, R. A. and S. D. Eckermann, 1990:VHF radar observations of mesoscale motions in the troposphere: Evidence of gravity wave Doppler shifting, *Radio Sci.*, **25**, 1019–1037.

Walterscheid, R. L. and D. J. Boucher, Jr., 1984: A simple model of the response of the thermosphere to impulsive forcing, *J. Atmos. Sci.*, **41**, 1062–1072.

Weinstock, J., 1987: The turbulence field generated by a linear gravity wave, *J. Atmos. Sci.*, **44**, 410–420.

Yeh, K. C. and C. H. Liu, 1972: Theory of ionospheric waves. Acad. Press, 464pp.

Yeh, T. C. and C. H. Liu, 1985: Evolution of atmospheric spectrum by processes of wave-wave interaction, *Radio Sci.*, **20**, 1279-1294.

Zeng, Q., 1978: Mathematical and physical principles of numerical weather prediction, Vol. 1, Acad. Press, Beijing, 543pp (in Chinese).

Zhu, X., 1987: Inertio-gravity waves in the middle atmosphere, Ph. D. thesis, Univ. of

Reproduced with permission of the copyright owner. Further reproduction prohibited without permission.

Washington, 167pp.

Zhu, X., and J. R. Holton, 1987: Mean fields induced by local gravity–wave forcing in the middle atmosphere, *J. Atmos. Sci.*, 44, 620–630.

Reproduced with permission of the copyright owner. Further reproduction prohibited without permission.